Patrick Hayes

Thesis

2007

Imperial College
London

Advances in Catalysis for Fuel Cells

A Thesis Submitted for the Degree of Doctor of Philosophy of the University of London and the Diploma of Imperial College

Dr A R Kucernak Research Group
Department of Chemistry
Imperial College
London SW7 2AZ

BIBL
LONDON
UNIV.

Advances in Catalysis for Fuel Cells. Patrick Hayes, PhD Thesis.

In order to reduce the costs of fuel cells, the amount of expensive precious metal catalyst needed must be reduced. Sputter deposition of platinum produces a thin platinum catalyst layer with a high surface area. The roughness is significantly enhanced by reactive sputter deposition of platinum. The usual inert plasma gas used for sputter deposition was replaced with oxygen, and the resulting platinum oxide layer was reduced electrochemically. Roughness factors of 138 to 154 ± 5 depending on substrate were produced by reactive sputtering, compared to 31-54 by inert sputter deposition, depending on the substrate, at a loading of 0.15 mg cm^{-2}. The catalyst layer thickness was 140 ± 40 nm. A fuel cell was constructed with reactively sputtered electrodes; on polarising the cell the currents obtained were 50-90 mA cm^{-2} at 0.5 V. A simple-pore model of the sputter deposited electrode is presented to examine the extent to which the catalysts are utilised.

The impact of sputter deposition on the proton conductivity of Nafion was investigated by AC impedance measurements. Membrane electrode assemblies which had been directly sputtered with platinum showed a conductivity up to 34% lower than that seen for the unsputtered membrane. Progress towards a transfer method that removes the need for direct sputter deposition is reported. Platinum was sputtered on a secondary substrate such as Al foil or soluble PVA films, then hot pressed to the membrane and dissolved. The extent to which the catalyst layer was transferred was found to be somewhat limited.

Another approach to reducing the costs of fuel cells is to use an alternative, non-precious metal catalyst. Tungsten carbides were produced by carburising tungsten oxide nanopowder and by carburising tungsten oxide from a Pechini-style polymer

precursor. The BET surface areas of these catalysts were 5.91 $m^2 g^{-1}$ and 2.51 $m^2 g^{-1}$ respectively; the crystallite sizes as determined by X-ray crystallography were 10.9 nm and 16.9 nm. The catalysts were found to exhibit activity towards hydrogen oxidation in an aqueous electrolyte and a half-cell. A fuel cell was constructed with a tungsten carbide anode and a conventional platinum cathode; the current at 0.5 V was found to be 10-18 mA cm^{-2}. Significantly, the performance did not deteriorate at all when the fuel stream was poisoned with 100 ppm carbon monoxide.

Acknowledgements.

Many thanks to my supervisor, Dr Anthony Kucernak, for excellent supervision, knowledge and guidance.

Thanks are also due to the current and former members of the Kucernak Group, including Junhua Jiang, Shengli Chen, Ruilin Wang, Dan Brett, Yangdong Quian (who assisted with the recording and interpretation of the XRD spectra shown in chapter 5), Greg Offer and Alice Sleightholme (who provided a small sample of high surface area Pd for use on reference electrodes, chapter 3). Technical help was provided by Steve Atkins and Simon Turner. Steve built the potentiostatic current loads used for fuel cell tests in this work and he and Simon assisted with the building of much other equipment.

Finally, many thanks to my family for their help and support, and most of all, to Nella.

Contents.

Chapter 1: Introduction. 15

1.1 Fuel Cells. 15

1.2 Polymer Electrolyte Fuel Cells. 20

1.3 Sputter Deposition. 27

1.4 Non-Noble Metal Fuel Cell Catalysts. 30

1.5 Scope of the Thesis. 34

Chapter 2: Sputter Deposition of Catalysts. 35

2.1 Introduction. 35

2.2 Experimental. 37

2.3 Results and Discussions. 40

2.4 Conclusions. 52

Chapter 3: Conductivity of Nafion Membranes. 54

3.1 Introduction. 54

3.2 Experimental. 59

3.4 Results and Discussions. 61

3.3 Conclusions. 66

Chapter 4: Indirect Deposition of Sputtered Platinum Catalysts. 67

4.1 Introduction. 67

4.2 Experimental. 69

4.3 Results and Discussions. 70

4.3.1 Assessment of Roughness Factors of Films. 70

4.3.2 Cracking of Catalyst and Loss of Catalyst from Nafion Films. 71

4.4 Conclusions. 74

Chapter 5: Investigations into Tungsten Carbide As a Possible Non-Noble Metal Fuel Cell Catalyst. 76

5.1 Introduction. 76

5.2 Experimental. 81

5.2.1 Production of Tungsten Carbide. 81

5.2.2 Rotating Disk Experiments. 82

5.2.3 Manufacture of Electrodes. 82

5.2.4 Testing of Electrodes. 83

5.3 Results and Discussions. 84

5.4 Conclusions. 97

Chapter 6: Fuel Cells With Tungsten Carbide Catalysed Anodes. 99

6.1 Introduction. 99

6.2 Experimental. 100

6.3 Results and Discussions. 101

6.3.1 Polarisation of a WC Fuel Cell Anode in the Absence of Hydrogen. 101

6.3.2 Operation of WC Fuel Cell Anodes on Pure Hydrogen. 103

6.3.3: Operation of WC Anodes in the Presence of CO. 107

6.4 Conclusions. 108

Chapter 7: Fuel Cell Testing of Sputter Deposited Catalysts. 109

7.1 Introduction. 111

7.2 Experimental. 111

7.3 Modelling of Catalyst Utilisation 115

7.4 Conclusions 119

Chapter 8: Conclusions. 120

8.1 Conclusions. 120

8.2 Further Work. 123

8.3 Dissemination. 123

Appendix A: Analytical Techniques. 124

A.1 BET surface area analysis. 124

A.2 Platinum Loading by ICP-AES. 124

A.3 X-Ray Powder diffraction. 125

Chapter 9: References. 127

List of Figures and Tables.

Chapter 1.

Figure 1.1: 'Volcano' plot of exchange current density, j_0/mAcm^{-2}, vs enthalpy of adsorption of hydrogen (Metal-hydrogen bond enthalpy/kJ mol^{-1}) on various metals. Taken from *Electrochemistry* by Rieger [2], data from Trasatti [3]. 18

Figure 1.2: The structure of Nafion, as originally reported by Grot [6]. 20

Figure 1.3: Channel structure of Nafion. Taken from Hammann, Hamnett and Vielstich [8]. 21

Figure 1.4: Schematic view of a hydrogen-fuelled PEM fuel cell, in cross-section. 23

Figure 1.5: Typical fuel cell polarisation and power curve for a hydrogen-fuelled PEM fuel cell. 24

Chapter 2.

Figure 2.1: Schematic of the electrochemical cell used for reduction of catalysts and surface area determination in this chapter, showing the working electrode arrangement. The reference electrode is a mercury/mercurous sulfate electrode. The electrolyte was 0.5 mol dm^{-3} H_2SO_4. Not shown are the connections to the potentiostat. 38

Figure 2.2: Cyclic voltammogram of a typical polycrystalline platinum electrode in 0.5M H_2SO_4, N_2 bubbled, 5 mV s^{-1}, room temperature, measured vs MMSE corrected to the RHE scale. 40

Figure 2.3: CO stripping voltammetry of Pt-catalysed GDE in 0.5M H_2SO_4, degassed with N_2, scan rate 15mVs^{-1}, where the electrode was held at 0.3V for 20 mins whilst the electrolyte was saturated with carbon monoxide gas. The electrolyte was then thoroughly degassed with nitrogen for 40 mins before scanning the potential to anodic potentials. 42

Figure 2.4: Schematic of Pt sputtered onto a carbon gas diffusion electrode composed of graphitic carbon paper and a layer of Vulcan XC72R. 44

Table 2.1: Typical roughness factors for the range of electrodes employed in this work by sputter deposition method and coated substrate. 45

Table 2.2: Comparing CO stripping and hydrogen adsorption measures of Electrochemically Active Surface Area of a reactively sputtered Pt on carbon gas diffusion electrode. Geometric electrode area: 1.12 cm^{-2}. 45

Figure 2.5: SEM image of Pt sputtered onto carbon gas diffusion electrode, showing the catalyst, high surface area carbon layer and the carbon fibres of the carbon paper substrate. The GDE was cleaved by a scalpel blade. Magnification ×540. 46

Figure 2.6: SEM image of Pt sputtered onto Nafion membrane, cleaved by a scalpel blade, showing the Nafion membrane and catalyst layer. Image recorded at 70° from normal to the catalyst surface. Magnification ×420. 47

Figure 2.7: SEM of Pt sputtered on Nafion at higher magnifications, cleaved by a scalpel blade, showing the Nafion membrane and catalyst layer. Image recorded at 70° from normal to the catalyst surface. Magnification ×17500. 48

Figure 2.8: Cross-section TEM of platinum catalysed membrane embedded in epoxy resin. Sections of the resin 90 nm thick were cleaved with a diamond knife. The Nafion membrane and resin support are highlighted. Magnification ×12000. 49

Figure 2.9: Cross-section TEM of platinum catalysed membrane embedded in epoxy resin, section 90 nm thick. The Nafion membrane and resin support are indicated. Magnification ×80000. 49

Figure 2.10: Cross-section TEM of platinum catalysed membrane embedded in epoxy resin. Sections of the resin 90 nm thick were cleaved with a diamond knife. The Nafion membrane and resin support are highlighted. Magnification ×40000. 50

Chapter 3.

Figure 3.1: A Randles equivalent circuit. Typical impedance equivalent circuit used for a working electrode in a standard three-electrode electrochemical cell, with uncompensated solution resistance (R_U), charge transfer resistance (R_{CT}), double layer capacitance (C_{DL}) and Warburg impedance. 57

Figure 3.2: A proposed simple equivalent circuit for fuel cell impedance studies with electrolyte resistance (R_{PE}), charge transfer resistance (R_{CT}) and double layer capacitance (C_{DL}). 58

Figure 3.3: Position of high surface area Pd reference electrodes in fuel cell test apparatus. 60

Figure 3.4: Detail of impedance response with unsputtered membrane and sputtered membrane at high frequency. Decadic frequencies indicated; 4=10kHz, 3=1kHz. Cell supplied with hydrogen, humidified at 70°C, cell at 65°C. 61

Figure 3.5: Impedance response with unsputtered membrane in fuel cell with reference electrodes in situ. Decadic frequencies labelled; 4=10kHz, 3=1kHz. Cell supplied with hydrogen, 7.5 cm^3 min^{-1} to both sides, humidified at 70°C, cell at 65°C. 62

Figure 3.6: Impedance response with sputtered membrane in fuel cell with reference electrodes in situ. Decadic frequencies labelled; 4=10kHz, 3=1kHz. Cell supplied with hydrogen, 7.5 cm^3 min^{-1} to both sides, humidified at 70°C, cell at 65°C. 64

Chapter 4.

Figure 4.1: Illustration of indirect sputter coating process Far left figure: secondary substrate shown in light grey, onto which is sputtered the Pt layer (black). The secondary substrate is then laminated to the Nafion membrane (dark grey, centre

figure). The secondary substrate is dissolved and the membrane pressed to the backing layer (dappled, far right figure). 68

Figure 4.2: CV of indirectly-sputtered platinum on Nafion working electrode in 0.5 mol dm^{-3} H_2SO_4, CO saturated for 20 mins then N_2 sparged for 40 mins whilst held at 0.4V versus RHE, then cycled at 25 mV s^{-1}. Potentials measured with saturated mercury/mercurous sulphate reference electrode corrected to reversible hydrogen scale. 71

Figure 4.3: Schematic diagram of the process of transmission imaging of indirectly coated membrane. 72

Figure 4.4: Typical transmission image of an indirectly sputtered membrane. Magnification ×68. Inset: the same image converted to binary black and white following the process described in the text. Magnification ×21. 73

Table 4.1: Roughness factors and estimated extent of platinum coverage for two indirectly-coated membranes. 74

Chapter 5.

Table 5.1: Tungsten carbide catalyst preparation methods. 83

Figure 5.1: 2 mg cm^{-2} WC(A) on RDE, 900rpm, in 0.5M H_2SO_4, sweep rate 5mVs^{-1}, sparged with reactant gases room temperature (20±5)°C. 85

Figure 5.2: Left: Levich analysis of current density at 0.4V vs RHE, 2 mg cm^{-2} $WC_{(A)}$ on glassy carbon RDE in 0.5mol dm^{-3} H_2SO_4, sparged with hydrogen, (20±5)°C, showing current density versus square root of rotation rate. Right: Koutechy-Levich plot, reciprocal current density versus (rotation rate)$^{-½}$ of same data. 86

Figure 5.3: Cyclic voltammogram of Tungsten Carbide Catalyst A in half-cell fed by H_2, electrolyte- room temperature 0.5 mol dm^{-3} H_2SO_4. Scan rate 5 mV s^{-1}, vs MMSE, corrected to reversible hydrogen scale, (20±5)°C. 89

Figure 5.4: Anodic hydrogen oxidation current density on various tungsten carbide catalyst fed with gaseous reactants under the conditions shown. Currents are steady-state, taken after 600s to give stationary current at potentials shown, without iR correction. The working electrode was a circular with 1 cm diameter. The reference electrode was held in the solution at the temperature shown. 90

Figure 5.5: Anodic hydrogen oxidation current on tungsten carbide catalysts. Currents are steady-state, taken after 600s to give stationary current at potentials shown, without iR correction. The working electrode was a circular with 1 cm diameter. The reference electrode was held in the solution at the temperature shown, 75°C 0.5 mol dm^{-3} perchloric acid. 91

Figure 5.6: X-ray powder diffraction pattern for tungsten carbide produced by carburising nanopowder. 94

Figure 5.7: X-ray powder diffraction pattern for tungsten carbide catalyst by polymer precursor method. 95

Figure 5.8: Anodic hydrogen oxidation current on tungsten carbide catalysts corrected to unit mass (left) and real surface area (right). Tungsten carbide catalysts prepared by carburising tungsten oxide nanopowder (open) and polymer precursor (filled). Currents are steady-state, taken after 600s chronoamperometry. Currents measured in half cell in 75°C perchloric acid vs MMSE, corrected to reversible hydrogen electrode scale. 96

Chapter 6.

Figure 6.1: Background currents for fuel cell with tungsten carbide (A) anode and JM Pt cathode. Humidified hydrogen gas fed to Pt electrode. Nitrogen (25 cm^3 min^{-1}) fed to tungsten carbide electrode. Hydrogen gas humidified at 70°C. Fuel cell heated to 65°C. Scan rate 1 mVs^{-1}. 102

Figure 6.2: Fuel cell currents and power density for tungsten carbide (catalysts A and C) anode and JM Pt cathode. Humidified hydrogen gas fed to anode at 15 cm^3 min^{-1}. Air (25 cm^3 min^{-1}) fed to Pt cathode (fuel cell test). Hydrogen gas humidified at 70°C. Fuel cell heated to 65°C. Data points recorded after 0.5 s at each point.. 103

Figure 6.3: Fuel cell data from figure 6.2 (above) corrected for BET surface area of catalysts. Humidified hydrogen gas fed to anode at 15 ml/min. Air (25 ml/min) fed to Pt cathode (fuel cell test). Hydrogen gas humidified at 70°C. Fuel cell heated to 65°C. Data recorded after 0.5s at each point. 106

Figure 6.4: Fuel cell currents for tungsten carbide (catalysts C) anode and JM Pt cathode. Humidified hydrogen gas, pure and containing 100ppm CO fed to anode at 15 cm^3 min^{-1}. Air (25 cm^3 min^{-1}) fed to Pt cathode (fuel cell test). Hydrogen gases humidified at 70°C. Fuel cell heated to 65°C. Data recorded after 0.5s at each point. 107

Chapter 7.

Figure 7.1: Polarisation curves for fuel cell with reactively sputtered platinum on membrane (filled circles) and on gas diffusion electrodes (open circles). Cell heated to 65°C; hydrogen (20 cm^3 min^{-1}) humidified at 70°C, cathode supplied with air (25 cm^3 min^{-1}). Pt on carbon electrodes (data from chapter 4) same conditions: crosses. Data recorded after 0.5s at each point. 112

Figure 7.2: Power curves for same fuel cells. Cell heated to 65°C; hydrogen (20 cm^3 min^{-1}) humidified at 70°C, cathode supplied with air (25 cm^3 min^{-1}). Pt on carbon electrodes (data from chapter 4) same conditions: crosses. Data recorded after 0.5 s at each point. 113

Figure 7.3: Extent of catalyst utilisation for sputtered catalyst for hydrogen oxidation, simple-pore model. Solid line: 140nm catalyst (as used in this work), 338 K. Dotted line: 280nm catalyst layer, 338 K. Dashed line: 140nm catalyst (as used in this work), 303 K. Dotted-dashed line: 280nm catalyst layer, 303 K. 117

Figure 7.4: Extent of catalyst utilisation for sputtered catalyst for oxygen reduction, simple-pore model. Solid line: 140nm catalyst (as used in this work), 338K. Dotted line: 280nm catalyst layer, 338K. Dashed line: 140nm catalyst (as used in this work). 303K. Dotted-dashed line: 280nm catalyst layer, 303K. 118

List of Abbreviations and Symbols.

SI and other units and chemical symbols have their usual meanings.

Å	Angstrom (10^{-10} m).
a	Specific roughness, R_f / thickness.
ads (subscript)	Adsorbate.
AFC	Alkaline fuel cell.
AFM	Atomic force microscopy.
B	Full-width at half maximum height of the peak (XRD experiments).
BET	Brunauer, Emmett and Teller method of surface area analysis.
C	Correction factor (XRD experiments).
c^0	Bulk reactant concentration.
C_{DL}	Double layer capacitance.
CV	Cyclic voltammogram/voltammetry.
D	Diffusion coefficient.
E_{cell}	Cell voltage.
ECSA	Electrochemically active surface area.
E_{OC}	Open circuit voltage.
F	Faraday's constant, 96485 C $mole^{-1}$.
FRA	Frequency response analyser.
GDE	Gas diffusion electrode.
GPES	General purpose electrochemical software, by Ecolab, Utrecht.
HOR	Hydrogen oxidation reaction.
ICP-AES	Inductively-coupled plasma atomic emission spectroscopy.
j	Current density.
j_0	Exchange current density.
JCPDS	Joint committee for powder diffraction studies.
j_d	Diffusion controlled current density.

j_k	Kinetically controlled current density.
JM	Johnson Matthey PLC (precious metal supplier).
m	Mass transport coefficient.
MEA	Membrane electrode assembly.
MMSE	Mercury/mercurous sulfate electrode.
n	Number of electrons transferred.
PAFC	Phosphoric acid fuel cell.
PEMFC	Polymer electrolyte membrane fuel cell.
ppb	Parts per billion.
ppm	Parts per million.
PSSA	Polystyrene sulfonic acid.
PVA	Polyvinyl alcohol.
ORR	Oxygen reduction reaction.
R	Gas constant (also resistance).
R_{CT}	Charge transfer resistance.
RDE	Rotating disk electrode.
R_f	Roughness factor, ratio of electrochemical to geometric surface area.
RHE	Reversible hydrogen electrode.
R_{PE}	Polymer electrolyte resistance.
SEM	Scanning electron microscopy.
SOFC	Solid oxide fuel cell.
T	Crystallite diameter (XRD experiments).
TEM	Transmission electron microscopy.
T_g	Glass transition temperature.
~~W~~	Warburg impedance.
wt%	Percentage by weight.
XRD	X-ray diffraction.

Z	Impedance.
β	Symmetry factor.
γ	Pore radius (simple pore model).
η	Overpotential.
θ	Fractional coverage of the monolayer (electrochemical desorption experiments).
θ	Diffraction angle (XRD experiments).
λ	X-ray wavelength (XRD experiments).
λ	Penetration depth of current (simple pore model).
ν	Solution viscosity.
ψ	Extent of utilisation (simple pore model).
ω	Rotational frequency (of RDE).

Chapter 1: Introduction.

1.1 Fuel Cells.

Fuel cells are the subject of a great deal of ongoing research interest, particularly with regard to their application to the portable power and automobile transport markets. They are a particularly attractive replacement for the internal combustion engine, due to growing concern over emissions of pollutants implicated in climate change and other environmental problems. Fuel cells potentially offer low or zero-emission power at high efficiency. They can also offer high volumetric and gravimetric power density, making them potentially competitive replacements for current battery technology in portable electronics such as laptop computers and mobile phones. They are quiet and contain no moving parts. There is therefore a wide range of academic and industrial interest in this promising technology.

Fuel cells are galvanic electrochemical cells, which convert chemical energy directly into electrical energy. Unlike batteries, they do not require charging and produce power as long as they are continually fed with reactants. The first fuel cell was demonstrated in 1839 by Swansea-born physicist Sir William Grove. He passed hydrogen gas over porous platinum electrodes, producing a noticeable electric shock felt by a chain of volunteers. Grove did not consider his invention to be a serious electricity generating technology, as it required many cells in series to produce a noticeable current, and was less convenient and efficient than a contemporary voltaic pile. He did, however, recognise that his cell was limited by the small area of platinum in contact with both gas and electrolyte [1]. Fuel cells therefore received little serious interest as power generation units until they were used to provide on-board power for the Gemini and Apollo space missions. The spacecraft already carried large reserves of liquid hydrogen and oxygen on board for primary rocket

power, so NASA engineers decided that fuel cells would provide an ideal source of secondary power, with drinkable water as the only by-product.

Further renewed interest was fuelled by the oil crises of the 1970's and the increasing environmental concerns of the late 20th century, such as climate change blamed on CO_2 emissions from cars and electricity generation. Today, a large number of automobile and portable electronics manufacturers are producing prototype models with fuel cell power.

There are a number of different types of fuel cells consuming many different fuels. They are often classed according to the electrolyte that they contain, including phosphoric acid fuel cells (PAFCs), alkaline fuel cells (AFCs, used on the Apollo space programs), solid oxide fuel cells (SOFCs, wherein the electrolyte is a yttria-stabilised zirconia matrix, which conducts oxygen ions at elevated temperatures) and polymer electrolyte membrane fuel cells (PEMFCs). The most common fuel used is hydrogen, though several other fuels are used, typically small organic molecules such as methanol. The oxidant is oxygen, often from air. The design of all types of fuel cell follows the same basic principles- a fuel is introduced to the anode side of the cell where it is oxidised and yields electrons which pass around an external circuit, doing work. Oxidant is introduced to the cathode side of the cell, where it is reduced. The electrolyte completes the electrical circuit; conduction in the electrolyte is provided by ions moving from one electrode to the other.

Hydrogen is used for fuel cells because it has high gravimetric energy density, facile oxidation kinetics and yields a potential of 1.23 V when oxidised in acidic conditions by aerial oxygen:

At the anode:

$$H_2 \rightarrow 2H^+ + 2e^- \qquad E^{\ominus}=0V.$$

At the cathode, the oxidant is admitted:

$$O_2 + 4H^+ + 4e^- \rightarrow 2H_2O \qquad E^{\ominus}=1.23V\ .$$

In acidic conditions the overall reaction is therefore:

$$2H_2 + O_2 \rightarrow 2H_2O \qquad E^{\ominus}=1.23V\ .$$

These reactions require an electrocatalyst to proceed. Platinum is the most active electrocatalyst for fuel cell reactions at accessible temperatures. The exchange current density j_0 for the hydrogen oxidation reaction (HOR) is extremely high. For the oxygen reduction reaction (ORR) the kinetics are less favourable (j_0 is lower) though platinum remains the catalyst of choice. In figure 1.1 below, the heterogenous catalytic properties of various metals are explored in terms of their j_0 for the hydrogen evolution reaction in acidic electrolytes. The candidate metals form a "volcano" plot. The reason for this is that catalytic behaviour for the hydrogen evolution reaction is dependant on a balance between the energy of desorption of the gaseous H_2 and the energy of adsorption of the H^+ ions in an acidic environment. The hydrogen oxidation reaction and oxygen evolution reactions show similar behaviour.

Figure 1.1: 'Volcano' plot of exchange current density, j_0/mAcm^{-2}, vs enthalpy of adsorption of hydrogen (Metal-hydrogen bond enthalpy/kJ mol^{-1}) on various metals. Taken from *Electrochemistry* by Rieger [2], data from Trasatti [3].

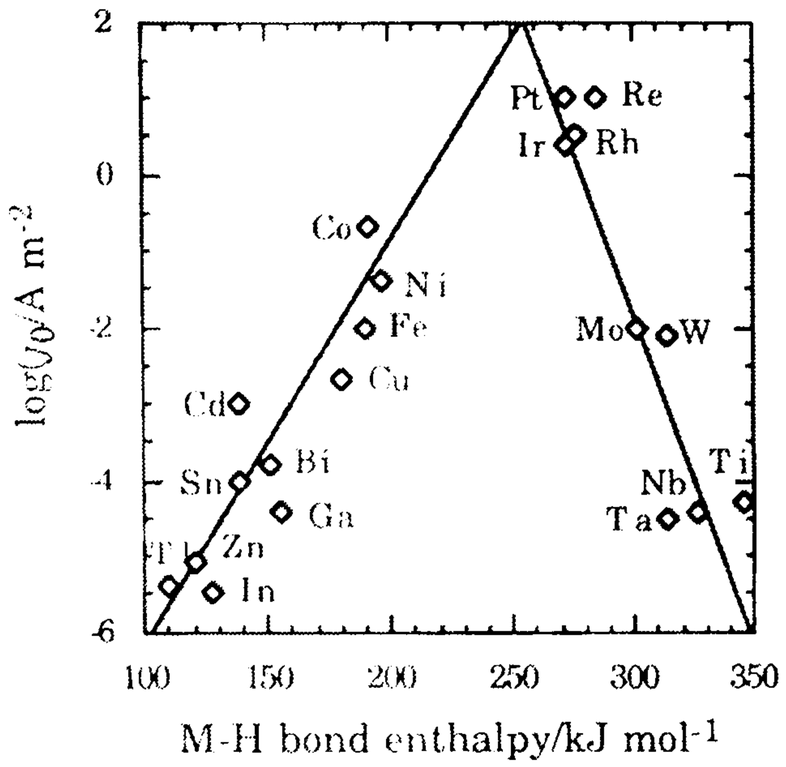

Carbon monoxide strongly adsorbs onto platinum at moderate temperatures, poisoning the catalyst. Therefore the required purity of the fuel depends on the type of cell being used. For low temperature PEM fuel cells, hydrogen with a total CO content as low as 10 ppm is required [4]. Higher temperature fuel cells, such as the SOFC and MCFC, can oxidize CO under fuel cell conditions and do not have platinum electrodes. Intermediate temperature cells that have platinum electrodes such as PAFCs can tolerate a higher CO content as the CO can desorb at the increased cell temperatures, because the equilibrium coverage of CO is lower at elevated temperatures. This is of importance because the proportion of CO and other impurities is affected by the method by which the hydrogen is produced. Hydrogen can be produced from hydrocarbon fuels such as methanol or natural gas by reformation. The product gas is known as reformate, which contains CO_2 and is rich in CO and unreacted hydrocarbons. On-board reformers have been suggested for fuel cell powered vehicles to take advantage of the superior volumetric energy density of liquid hydrocarbon fuels over gaseous hydrogen. Sulfur is an even more potent

poison of platinum catalysts; PEMFC performance is compromised by a sulfur content as low as 1 part per billion (ppb) [4].

Another promising fuel is methanol, which can be directly oxidised over various precious metal catalysts. The reactions that take place in acidic conditions are:

At the anode:

$$CH_3OH + H_2O \rightarrow CO_2 + 6H^+ + 6e^- \qquad E^e=0.01V.$$

At the cathode:

$$6H^+ + {}^3/_2O_2 + 6\,e^- \rightarrow 3H_2O \qquad E^e=1.23V.$$

Overall:

$$CH_3OH + {}^3/_2\,O_2 \rightarrow 2H_2O + CO_2 \qquad E^e=1.22V\ .$$

The anode catalyst employed is typically a bimetallic alloy such as platinum-ruthenium. Platinum exhibits catalytic activity for methanol oxidation but is rapidly poisoned by a carbon monoxide-like intermediate of the oxidation reaction [5]. This poisoning is mitigated by the ruthenium component of the catalyst, which oxidises the carbonyl and formic acid intermediates. Methanol continues to attract research interest as an electroactive fuel because of its high volumetric energy storage density. As it is a liquid at room temperature, it could be easily integrated into the existing storage and refuelling infrastructure for transportation.

One of the barriers to fuel cell commercialisation is the high capital cost of the materials. Platinum is an extremely expensive material; therefore there is a strong incentive to reduce the total amount of platinum used without compromising the fuel

cell's overall performance. This can be achieved by increasing the catalyst's surface area per unit mass, and manufacture of high-surface area platinum catalysts is well advanced.

1.2 Polymer Electrolyte Membrane Fuel Cells.

It is polymer electrolyte membrane fuel cells that hold the greatest promise for the automobile and portable electronics markets. They operate at a low temperature (up to 85°C) and are relatively simple to construct. At the heart of this type of fuel cell is a solid polymer membrane, which conducts protons when hydrated. By far the leading material used for this purpose is DuPont's Nafion. Nafion is a perfluorosulfonate polymer based on a hydrophobic PTFE backbone, with hydrophilic branches consisting of short chains with sulfonic acid head groups. The material is physically robust, and chemically inert as it is fully fluorinated. It is also electronically insulating. It was developed as a separator membrane for the Chlor-Alkali process, where chlorine, hydrogen and caustic soda are produced from the electrolysis of brine. The structure is shown in figure 1.2.

Figure 1.2: The chemical structure of Nafion, as originally reported by Grot [6], n=6-10, m=0-2, typically 2.

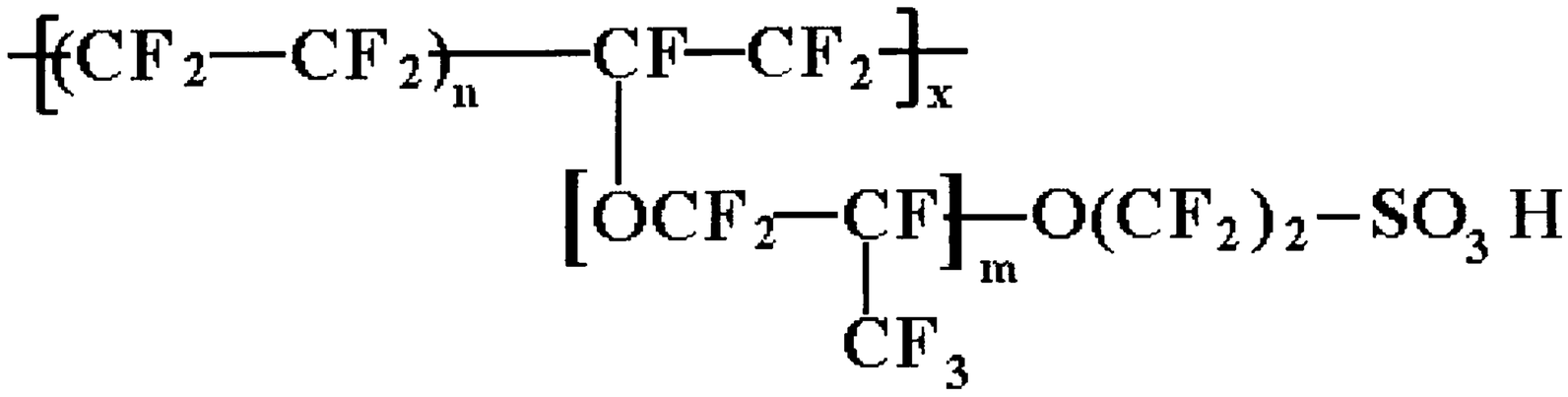

The value of n is typically 6-10, but can be varied to produce different structures of Nafion with different equivalent weights, where the equivalent weight is the mass of dry Nafion per mole of sulfonic acid groups.

When Nafion is manufactured, the side chain head groups are in the form of sulfonyl fluoride, $-SO_2F$. This material can then be converted to a sodium or potassium form, $SO_2^- Na^+$ or $SO_2^- K^+$ with a sodium or potassium hydroxide solution in water and dimethyl sulfoxide. This form of the material can then be ion exchanged in acid to yield sulfonic acid head groups. Because of the electron-withdrawing effect of the fluorintated groups, protons on the head group are strongly acidic. When the polymer is hydrated, these cations are free to migrate along hydrophilic channels, conferring on the polymer its property of ionic conduction.

The morphology of hydrated Nafion has not been conclusively described, and is the subject of current research interest [7], often studied by X-ray scattering and neutron scattering techniques. Most early work on the structure of hydrated Nafion suggested a cluster-network model, where the hydrophilic side chains form clusters around 40 Å in diameter, connected by hydrophilic channels around 10 Å in diameter. The channel structure is shown schematically in figure 1.3.

Figure 1.3: The suggested channel structure of hydrated Nafion. Taken from Hammann, Hamnett and Vielstich [8].

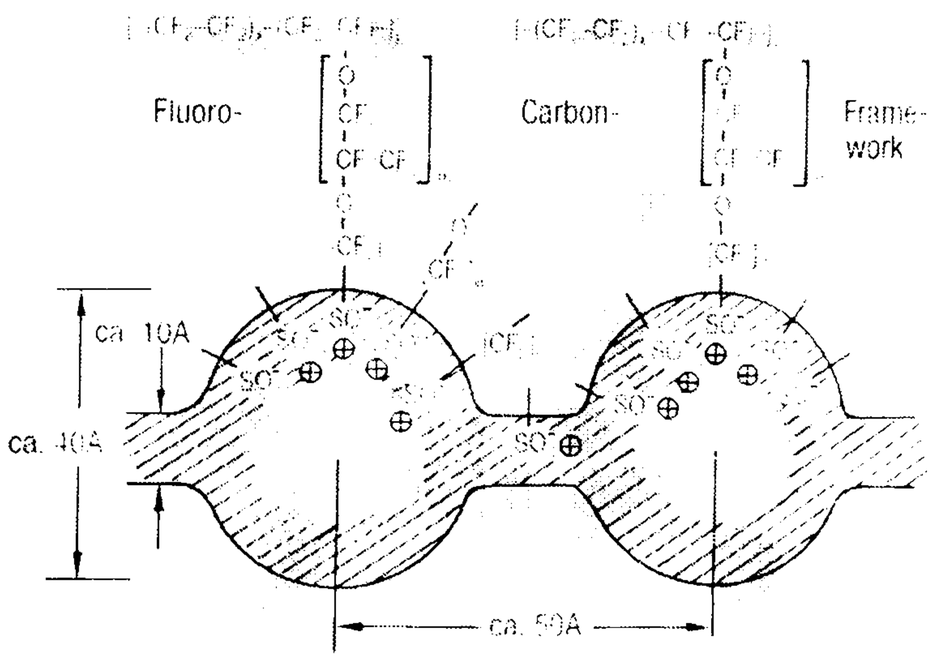

A range of alternate morphologies have been proposed more recently, including a lamellar-style "sandwich" model proposed by Haubold et al [9] and rod-like particles,

proposed by Rutabat and co-workers [10]. What is agreed is that hydrated Nafion has a multiple phase structure based on hydrophobic regions consisting of the fluorinated backbone of the polymer, hydrophilic regions bounded by the ionic head groups of the side chains, and water itself.

Polymer electrolyte fuel cells are usually fuelled with hydrogen, though they can operate as a direct methanol fuel cell (see section 1.1) as both fuels are oxidised in acidic media and the electrolyte can readily conduct protons from the anode to cathode. Nafion can be cast into thin membranes that can be located between the electrodes, acting as an electronically insulating separator. This facilitates the building of fuel cell stacks, necessary to combine the power output of several individual fuel cell units to give performance acceptable to commercial applications.

A schematic of a PEM fuel cell is shown in figure 1.4. Reactant gases are admitted on either side of the electrolyte membrane and flow through channels machined in the current collectors, which are usually graphite blocks. Immediately contacting the membrane are gas diffusion electrodes made of porous graphite materials such as carbon paper or carbon cloth. The catalyst is located at the interface between the gas diffusion electrode and the polymer electrolyte. Hydrogen, and occasionally air, is humidified before entering the fuel cell in order to maintain Nafion membrane hydration, essential for proton conductivity.

Figure 1.4: Schematic view of a hydrogen-fuelled PEM fuel cell, in cross-section.

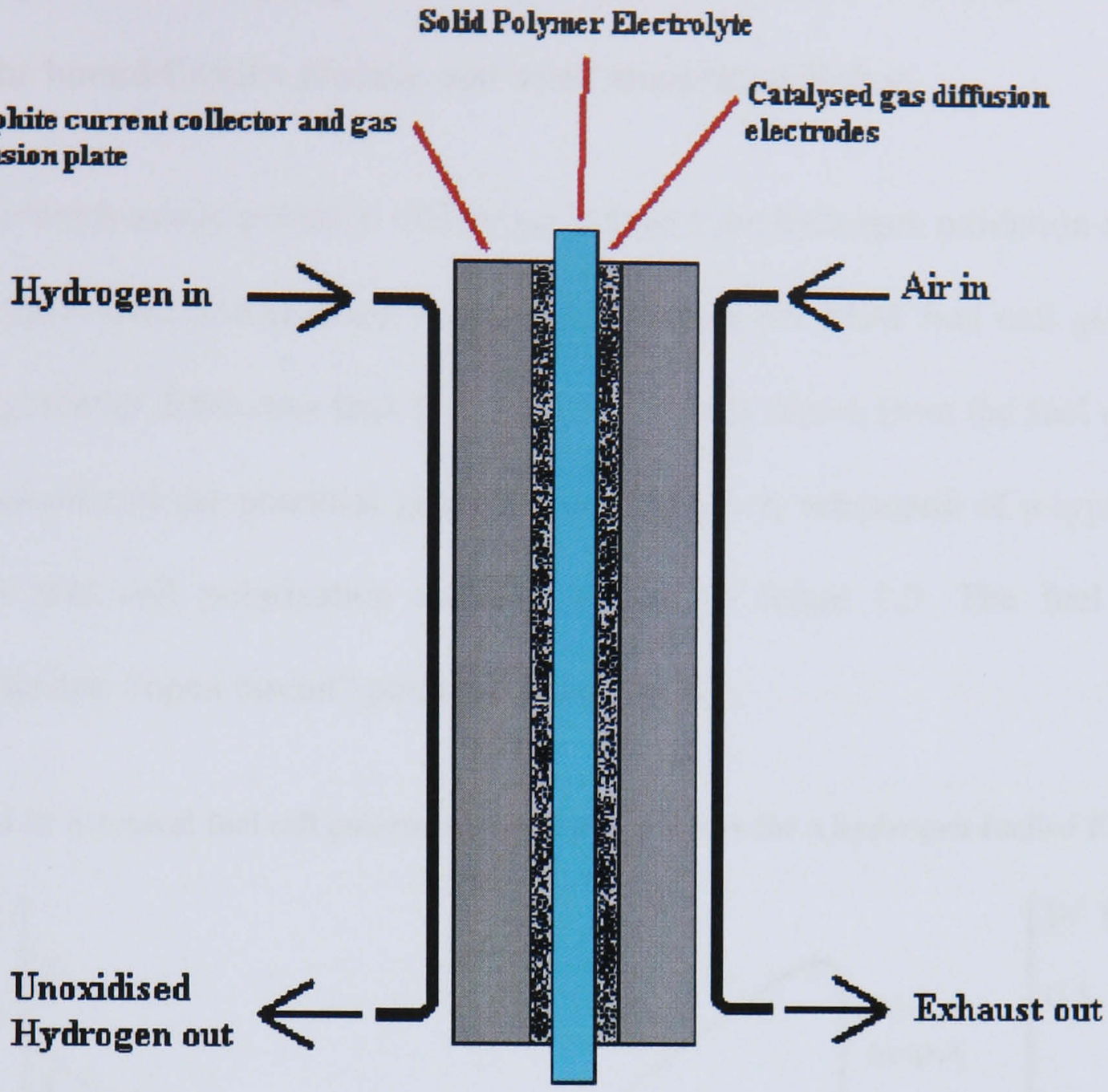

The electrochemical processes that take place in a fuel cell require a supply of gaseous reactants, access to the catalyst and contact with the Nafion. This means that the reactions take place solely at a triple-phase contact area between gas, catalyst and electrolyte. Fuel cell operation can therefore be improved by maximising the area of this triple phase contact. Catalyst particles that are located entirely within the polymer electrolyte are out of electronic contact with the graphite electrodes and in a region where gaseous reactant cannot diffuse. Catalyst particles located away from the electrolyte in the gas diffusion electrode similarly do not catalyse the overall fuel cell reaction. To increase the utilisation of the platinum catalyst, fuel cell membrane-electrode assemblies (MEAs) are manufactured with active layers. These layers contain intimate mixtures of platinum nanoparticles supported on high surface area

carbon powders and hydrophobic PTFE in order to prevent flooding with liquid water from the humidification process, and small amounts of Nafion.

The thermodynamic potential difference between the hydrogen oxidation reaction and the oxygen reduction reaction is 1.23 V. However the PEM fuel cell gives a rather lower potential difference than this. When current is drawn from the fuel cell, the cell is polarised and the potential generated is reduced. A schematic of a typical state of the art fuel cell polarisation curve is shown in figure 1.5. The fuel cell has a characteristic "open circuit" potential shown as E_{OC}.

Figure 1.5: A typical fuel cell polarisation and power curve for a hydrogen-fuelled PEM fuel cell.

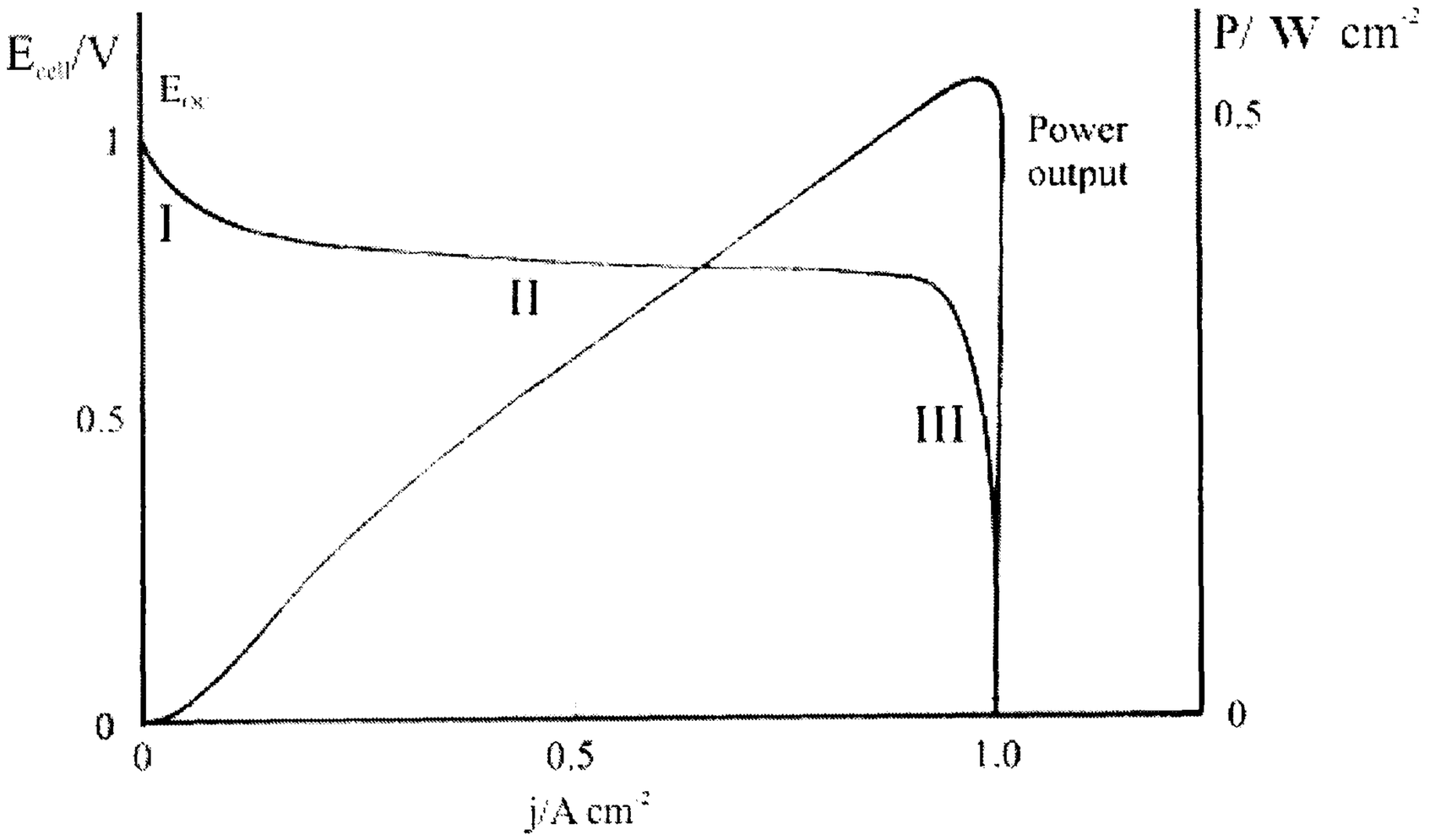

To draw an appreciable current, the electrodes must operate at a kinetic overpotential, η, given by the Butler-Volmer equation:

$$j = j_0\left[\exp\left\{\frac{(1-\beta)F\eta}{RT}\right\} - \exp\left\{\frac{\beta F\eta}{RT}\right\}\right]$$

where j is the current density, j_0 the exchange current density, β the reaction symmetry factor, η the electrode overpotential and F, R and T have their ususal meanings of the Faraday constant, gas constant and temperature. The kinetic overpotentials are subtracted from the overall fuel cell potential. This effect is shown on the schematic fuel cell polarisation curve, figure 1.5, marked as region I.

Above a certain current density, the kinetics of the reactions at the electrodes become more rapid and are no longer limiting. In region II, above, the current density drawn from the fuel cell rapidly increases. In this region, the potential drawn from the cell is limited by ohmic losses within the electrodes and (primarily) the polymer electrolyte. As these losses are purely due to Ohm's law resistances, they are often referred to as iR losses. Finally, in region III, at the highest current densities available, the performance of the fuel cell starts to be limited by the availability of reactants diffusing to the catalysed electrodes. The potential in this region is under mass transport control. As the current drawn increases to a maximum, the cell no longer generates a potential and is operating at short circuit.

As indicated by the schematic power curve shown on figure 1.5, typical PEM fuel cells draw their maximum power at around 0.5V, though when used for practical energy conversion applications they are operated at around 0.8-0.7V where the fuel efficiency is greater. Furthermore, by operating at higher potentials the heating effects due to resistance losses are lowered. For automotive uses, cells are usually combined in a series stack and their output subjected to some form of power conditioning.

The structure of the catalysed area has implications for the shape of the polarisation curve, and thereby the performance of the cell. The kinetic overpotentials are related to the exchange current density of the HOR and ORR on the catalyst of choice, hence

the platinum catalyst, the electrochemically active surface area should be as high as possible. Potential losses due to iR effects are minimised by maintaining Nafion hydration and maximising electronic conductivity of the catalyst/electrode interface. Mass transport losses are mitigated by maximising diffusion of the reactants to the catalysed region. Design of the electrodes has a major effect on this aspect of fuel cell performance. The electrodes and catalyst support must be sufficiently porous to allow gaseous reactants access to the catalyst/electrolyte interface. The pores must be wet-proofed to prevent flooding with liquid water arising from the humidification of the reactant gases and the product water produced at the cathode. Electrode design must therefore maximise the triple-phase electroactive area to increase the total current at low overpotentials; the overall width of the catalysed layer should be reduced to improve ionic and electronic conductance, and improve mass transport of the gaseous reactants; and a wetproof, porous yet continuous gas diffusion phase must be sought.

Platinum catalysts for fuel cells predate the invention of the PEM cell. Grove's original cell contained platinum catalysts. However, the amount of platinum used on the Gemini space programme PEM cells was considerable, and the associated cost was a significant barrier to commercialisation. More recent research has been focussed on utilising the platinum more efficiently. Earlier high-surface area catalysts were made from platinum black bound with PTFE, typically at a relatively high loading, around 4 mg cm^{-2}. Later, PEMFC designers began to impregnate the catalyst layer with Nafion ionomer [11]. The use of a carbon support allowed the production of catalysts with platinum particles of diameters of a few nanometres, reducing the platinum loading to around 0.4 mg cm^{-2} or lower [12]. Platinum nanoparticles can be synthesised in a variety of ways, usually involving a reduction of a chloroplatinate complex, platinum sulfito complex or other platinum salt [13].

1.3 Sputter Deposition.

Sputter deposition is a widely used technique for depositing a thin film of metal. It has found applications in such diverse areas as semiconductor wafers, mirror coatings and providing conduction to insulating samples for electron microscopy imaging. The sputtering process involves evacuating a chamber containing a disc of the material to be deposited (the target) and the sample to be coated (the substrate). A small amount of gas, typically argon, is bled into the chamber, and a potential difference is applied between the target and the walls. Under these conditions, the gas is ionised to a conducting, glowing plasma. Charged gas particles then stream towards the target, impacting on its surface at sufficiently high energy to eject atoms of the metal, which are then deposited on the surface of the substrate. This process can produce thin films of catalyst with relatively high surface areas.

Sputtering was developed by Sir William Grove [14], the inventor of fuel cells. Although sputtering had been used previously to create platinum surfaces for other electrochemical studies, the technique was first used to deposit catalysts for fuel cells by Weber and co-workers [15]. There has been sporadic research interest in this topic ever since. Mukerjee et al [16] studied the effect of adding a sputter-deposited platinum layer onto a conventional fuel cell catalyst layer. They concluded that locating a higher proportion of the catalyst as close as possible to the gas-electrolyte interface could bring about a fourfold increase in the exchange current density (based on geometric electrode surface area) for the ORR for comparable catalyst loading.

Later work by Hirano, Kim and Srinivasan [17] advanced the approach further, demonstrating that sputter deposition of platinum onto standard, uncatalysed GDEs could give comparable cathode performance to proprietary GDEs at very low loading (0.1 mg cm^{-2}) though the anode activity was limited by a high anode overpotential.

possibly due to mass transport limitations. Further work by Cha and Lee [18] represented a significant advance in the efficient use of platinum. They found that enhanced performance could be achieved by sputtering very thin layers of platinum, around 5nm thick, in a layered structure. In between sputtered layers, a Nafion-Carbon ink was applied and dried. Fuel cell performance comparable to that shown by conventional 0.4 mg cm^{-2} fuel cell electrodes was achieved with loadings as low as 0.04 mg cm^{-2}. Work by O'Hayre et al [19] showed a well-defined peak in the performance of sputtered fuel cell catalysts at extremely low loading- around 0.014 mg cm^{-2}, accompanied by a similar peak in the electrochemically active surface area of the platinum catalyst.

If the inert argon plasma gas usually used in the sputtering chamber is replaced with a reactive gas such as oxygen, the ejected target material particles have a chance to react. The sputtered particles are ejected in a relatively energetic state and pass through the glowing plasma of ionised oxygen gas, so it is highly likely that the resultant coating sputtered onto the substrate is oxidised, creating a layer that is largely or wholly oxide. This technique is known as reactive sputtering. Reactive sputtering has been used to deposit oxides of titanium for optical electronics [20], and to deposit platinum oxide in various forms for applications as electrodes in electronic devices, where Pt oxides are used to connect platinum to oxide material [21]. There is much research literature on the nature of platinum oxide films produced by reactive sputtering [21-25]. It appears that there is a number of differing platinum oxide structures that can be formed. It is possible to produce crystalline phases, designated α-PtO_2 [25] by controlling the conditions carefully. In this work the oxides were characterised by XRD and Raman scattering, and the paper provides a phase diagram showing the oxide phase obtained for varying oxygen content in the plasma gas, and

sputtering power. Higher sputtering power and increased partial pressure of oxygen were shown to produce amorphous phases, designated a-PtO_2 [23].

High surface area platinum catalysts have been obtained by reduction of platinum oxides for many years. This approach is the basis of Adams' catalyst, used since 1922 for the hydrogenation of various organic compounds [26]. A porous, highly dispersed platinum structure can be obtained by reduction of platinum oxide; a stream of 4% hydrogen in argon at room temperature, or CO at 200°C, flowed over an amorphous a-PtO_2 layer was sufficient to fully reduce the material to Pt with small particle sizes (5-10 nm) as confirmed by XRD analysis. This result suggests that such reduced films may make useful high surface area Pt electrodes. Further work by Maya et al [27] confirms that electrodes made using this technique demonstrate high electrochemically active surface area per unit geometric surface area. They characterised their electrodes with X-ray diffraction and AFM, producing detailed images of the distinctive microstructures of platinum available by reactive sputtering. They also showed the significance of the lower density of both the sputtered platinum oxide (2.0 g cm^{-3}) and the reduced platinum (3.4 g cm^{-3}) compared to the bulk density of these materials, typically around 8 g cm^{-3} and 21.25 g cm^{-3} respectively.

There is clearly scope for further research into the application of sputtering in general, and reactive sputtering in particular, to create highly dispersed platinum electrodes at low loading. This approach to improving fuel cell electrodes is chosen here for further study because it offers a route to high surface area platinum catalysts at low loading. The success of this approach can be assessed in three ways. Firstly, the electrochemically active surface area per unit mass of catalyst gives another measure of the dispersion of the catalyst. This quantity is known as the specific surface area and has units of $cm^2\ g^{-1}$. Secondly the electrochemically active surface area of the

catalyst can be assessed and compared to the geometrical surface area occupied by the catalyst, giving a quantity known as roughness factor, R_f, which is has units of $cm^2\ cm^{-2}$:

$$R_f = \frac{\text{electrochemically active surface area}}{\text{geometric surface area}}$$

A further figure of merit for the effectiveness of platinum catalyst utilisation is the specific roughness, **a**. This is calculated by dividing the roughness factor R_f by the catalyst layer thickness, so has units of $cm^2\ cm^{-3}$.

A second reason for the choice of the sputtering/reactive sputtering approach is the extremely thin catalyst layer that results. This yields a substantial increase in the specific roughness when compared to classical fuel cell electrodes. Extensive work in the literature highlights the advantages of localising the catalyst at the electrolyte/gas diffusion electrode interface. In a classical fuel cell the reaction takes place in a particularly narrow region of the catalysed electrode. An improved specific roughness combined with careful design of the overall fuel cell components is therefore considered a route to improved performance under half- and full fuel cell conditions.

1.4 Non-Noble Metal Fuel Cell Catalysts.

Whilst the utilisation of platinum in state-of-the-art fuel cells is decreasing, the use of precious metals contributes significantly to the capital cost of fuel cell units, and major demands on world platinum supplies may increase the cost. Alternatives to platinum catalysts are therefore sought. As can be seen from figure 1.1, there are few genuine competitors to platinum as the pre-eminent metallic heterogeneous catalyst for the hydrogen oxidation/evolution reaction. Research attention has therefore been focussed on the possibility of non-noble metal replacements. At the cathode, alternative oxygen reduction catalysts have included cobalt porphyrin-type materials

[28], as well as other cobalt compounds and iron compounds [29]. At the anode, there has been a great deal of interest in the use of transition metal carbides as potential replacements for platinum. The addition of carbon forms interstitial alloys with transition metals with regular, well understood structures and high electronic conductivity.

Tungsten carbide was first noted as having similar catalytic behaviour to platinum-group metals by Böhm [30] and later by Levy [31]. Since this work, there have been many papers discussing the use of tungsten carbides for various conventional organic reactions such as hydrocarbon conversion [32] and catalytic conversion of automobile exhaust [33]. Curry and Kendrick [34] investigated the surface compositions and catalytic properties of tungsten carbides made by various temperature-programmed carburisation methods. They used the dehydrogenation of butane as a test reaction to investigate the catalyst activity. They found that increasing the space velocity of reactant gases increased the surface area of the catalysts, as did increasing the proportion of H_2 in the carburising gas mixture. They reported that the highest surface area catalysts demonstrated similar activity to standard Pt-Sn/γAl_2O_3 dehydrogenation catalysts.

Because of the similarity of some transition metal carbides to platinum group metal catalytic activity, researchers soon turned to the possibility of similar electrocatalytic activity [35-37]. It is noted that tungsten carbides show modest kinetic activities for hydrogen oxidation in acidic electrolytes; more importantly they are not susceptible to poisoning by carbon monoxide or sulfur-containing compounds, which represents a significant advantage for possible fuel cells running on impure fuels such as reformate. Barnett et al [38] explored a range of nickel, tungsten and molybdenum

containing carbides for electrocatalytic activity towards methanol oxidation, and concluded that the key requirement of these catalysts for methanol oxidation in acidic solutions was passivity towards corrosion in acid. Nickel/tungsten and nickel/tungsten/molybdenum carbides demonstrated moderate catalytic activity for methanol and hydrogen anodic oxidation; carburised nickel/molybdenum showed no activity.

The production methods of tungsten carbide have long been known to influence the catalytic activity of the materials [37]. Giraudon et al [39] studied the effect of varying the composition of the carburising gases on the resulting catalysts composition and surface area. They indicated that their highest surface area available was 27 m^2 g^{-1}, with a core of W_2C covered with a shell of WC, as elucidated by XPS. McIntyre, Burstein and Vossen [40] thoroughly investigated the effect of a proportion of CO on the anodic oxidation of hydrogen on tungsten carbide. Their results showed that, contrary to earlier assertions in literature [30], there was a small catalyst poisoning associated with carbon monoxide, resulting in a drop in current density of around 2-6% at 0.29V vs RHE. This effect was rapidly reversed when pure H_2 was restored.

There is reason to suppose that tungsten carbides may be a promising replacement for platinum in fuel cells, offering major cost advantages, and a tolerance to CO and sulfur poisons that platinum cannot match, opening the way to a wider use of reformate-derived hydrogen in a fuel cell with these catalysts. They do not offer comparable currents for anodic oxidation of fuels in a fuel cell, but these materials do show appreciable catalytic performance at higher catalyst loading. There is therefore an opportunity to further research the catalytic behaviour of these materials in a fuel

cell environment, and explore novel approaches to their synthesis and preparation for use.

1.5 Scope of the Thesis.

This thesis aims to present an account of a substantial effort to research approaches to increasing the commercial viability of fuel cells for transportation and portable applications. One of the main obstacles to commercialisation of established fuel cell technology is the high cost of platinum metal catalysts and platinum-group alloys. Sputter deposition and reactive sputter deposition have been chosen as a route to a high surface area, minimal thickness platinum layer. It is anticipated that the efficiency of utilisation of platinum could be maximised by employing these techniques, because the technique has previously been shown to produce roughened catalyst layers on an extremely fine scale, and because localising the catalyst to within a narrow thickness around the electrolyte/electrode interface is anticipated to make use of an increased proportion of the catalyst for the fuel cell reactions. The performance of electrodes in a working fuel cell made using reactive sputter deposition technique will be investigated in detail.

A second approach to surmounting the problem posed by the cost of platinum, and consequent high capital cost of fuel cells, is to use non-noble metal catalysts on the fuel cell electrodes. Previous work in literature suggests that a suitable replacement for platinum exists in the tungsten carbides. These catalysts will therefore be further investigated for suitability in fuel cells and their performance in a fuel cell environment will be investigated. There has been little work in literature establishing novel routes to the synthesis of these materials, so new approaches to high surface area tungsten carbides will be explored.

The aim of this work is therefore to make contribution to the scientific knowledge about these two routes to reducing the costs of fuel cells. The thesis outlines and discusses work towards these aims, and the limitations of the work. It also suggests further work that could continue these investigations, and new directions the work could take in the future.

Chapter 2: Sputter Deposition of Catalysts.

2.1 Introduction.

As discussed in the introduction, section 1.3, sputtering has been shown previously to produce a highly roughened, ultrathin layer of platinum catalyst; this roughness can be further enhanced by the use of an oxidising plasma gas mixture and subsequent reduction. It was decided to employ this technique to produce membrane electrode assembly components for fuel cells.

Sputter deposition conventionally uses argon as the plasma gas, which is inert and has relatively massive ions. This means a large number of target particles are ejected per impact with high-energy argon ion. The ratio of particles ejected per ion impact is known as the sputter yield- this is typically around 5-20 for platinum sputtered with argon [41]. Oxygen ions are less massive and are not inert, leading to a lower sputter yield and reactions in the plasma between the gaseous ions and the ejected material from the target.

Following evacuation, gas is introduced to the chamber at low pressure. An electrically conducting plasma is formed by applying a potential difference between the target and the walls of the chamber. This potential difference can be either a DC applied potential or a radio frequency potential. A number of different conditions can be varied which have an effect on the resulting sputter-deposited layer. These include pressure of gas in the sputter chamber; applied current; sputter target-substrate separation distance and (as mentioned above) the composition of gas. If the pressure is too high a plasma cannot be initiated at the potentials applied to the electrodes; if the pressure is too low then insufficient current flows for a sustained glowing

discharge to form. The sputtering current is another characteristic parameter of the process. Because the sputtering process involves the flux of charged ions from the plasma to the target, the current that passes through the sputtering circuit gives a measure of the rate of ejection, and consequently deposition. The ejected particles spread out from the target and impact on the sample; the rate of sputter deposition is therefore influenced by the sample to target distance. The pressure of the gas has an influence on the morphology of the resulting films, as studied by Klabunde and others [42]. The influence of the energy fluxes within the plasma was modelled by Druseda, who performed a Monte Carlo simulation of the effect of the variations in the different energetic regions of the plasma on the resulting structure of the catalysed layer [43, 44].

Fine control of the sputtering conditions, in particular the gas pressure, can have effects on the particle size of the resulting deposited film. Small metal crystallites in the deposited film give it a high surface area at low metal loadings. Reactive sputter deposition from an Ar/O_2 plasma mixture is one of a relatively few routes to solid platinum oxide; others being the anodic oxidation of solid platinum or exposure of metallic platinum to highly elevated pressures of oxidising gas. As a result, the technique has been used since the work of Westwood [45] to produce thin films of platinum oxide. As discussed in the introduction, the film has metallic character, though the reported resistivity of the film also varies with changing sputtering conditions [46]. The authors presented results showing the resistivity of their films varied between 1 Ω cm and 10^{-5} Ω cm as the proportion of oxygen in the gas mixture varies between 100% and 0%. The latter figure is close to the value for bulk Pt, at 1.06×10^{-5} Ω cm. The film has been shown to contain a number of different possible crystalline and amorphous phases. The reduction of the resulting film is readily

achieved under flowing hydrogen gas or electrochemically, leaving metallic platinum with a highly porous microstructure. In this chapter, these techniques are applied to the manufacture of high surface area electrodes for fuel cells.

2.2 Experimental

Nafion 117 membranes, (Solution Technologies, USA) were used as the substrates for the catalyst layers. Membranes were prepared by boiling in 0.5M H_2SO_4 for 30 mins, followed by boiling in 3 wt% H_2O_2 for 30 mins. They were then rinsed in boiling Milli-Q water (Millipore, Watford, UK) for 60 mins with several changes of water. The membranes were dehydrated in a vacuum oven at 80°C, 20-60 mbar (2-6 kPa) for 1 hr.

Gas diffusion electrodes were made from wetproof carbon paper, 6 wt% PTFE (Toray). XC72-R carbon (Vulcan) was added to the surface at a loading of 4 mg cm^{-2}, by sonicating the carbon in water (Milli-Q) with a small amount of tetrahydrofuran (THF) (BDH, UK). The resultant ink was painted in stages onto the carbon surface, and the THF/water solvent was allowed to evaporate. A PTFE binder was added to the carbon surface by dropping a suspension of PTFE particles in water onto the hydrophillic carbon surface, such that the PTFE loading was 40 wt%. It was assumed the PTFE suspension would not wet the underlying hydrophobic carbon paper. The electrode was dried at 80°C and 5 mbar (0.5 kPa) in a vacuum oven, then the PTFE binder was annealed at 350°C for 120 mins.

The electrochemical cell for cyclic voltammetry measurements consisted of a Hg/Hg_2SO_4 reference electrode (Radiometer, Copenhagen). The counter electrode was a platinum flag. The working electrodes were supported by two pieces of non-wetproof carbon paper and held in a Teflon holder made in house (see figure 2.1).

Contact to the electrode was made by a gold wire. The cell assembly can be seen in figure 2.1. The cell was rigorously cleaned by the use of an acidified potassium permanganate solution, rinsed with an acidified hydrogen peroxide solution and Millipore water, several times. Solutions were degassed thoroughly with nitrogen via a pasteur pipette or bubbler. All voltammetry experiments were performed at room temperature in 0.5M H_2SO_4. Measurements were made by an Autolab Potentiostat (Ecochemie, Utrecht).

Figure 2.1: Schematic of the electrochemical cell used for reduction of catalysts and surface area determination in this chapter, showing the working electrode arrangement. The reference electrode is a mercury/mercurous sulfate electrode. The electrolyte was 0.5 mol dm^{-3} H_2SO_4. Not shown are the connections to the potentiostat.

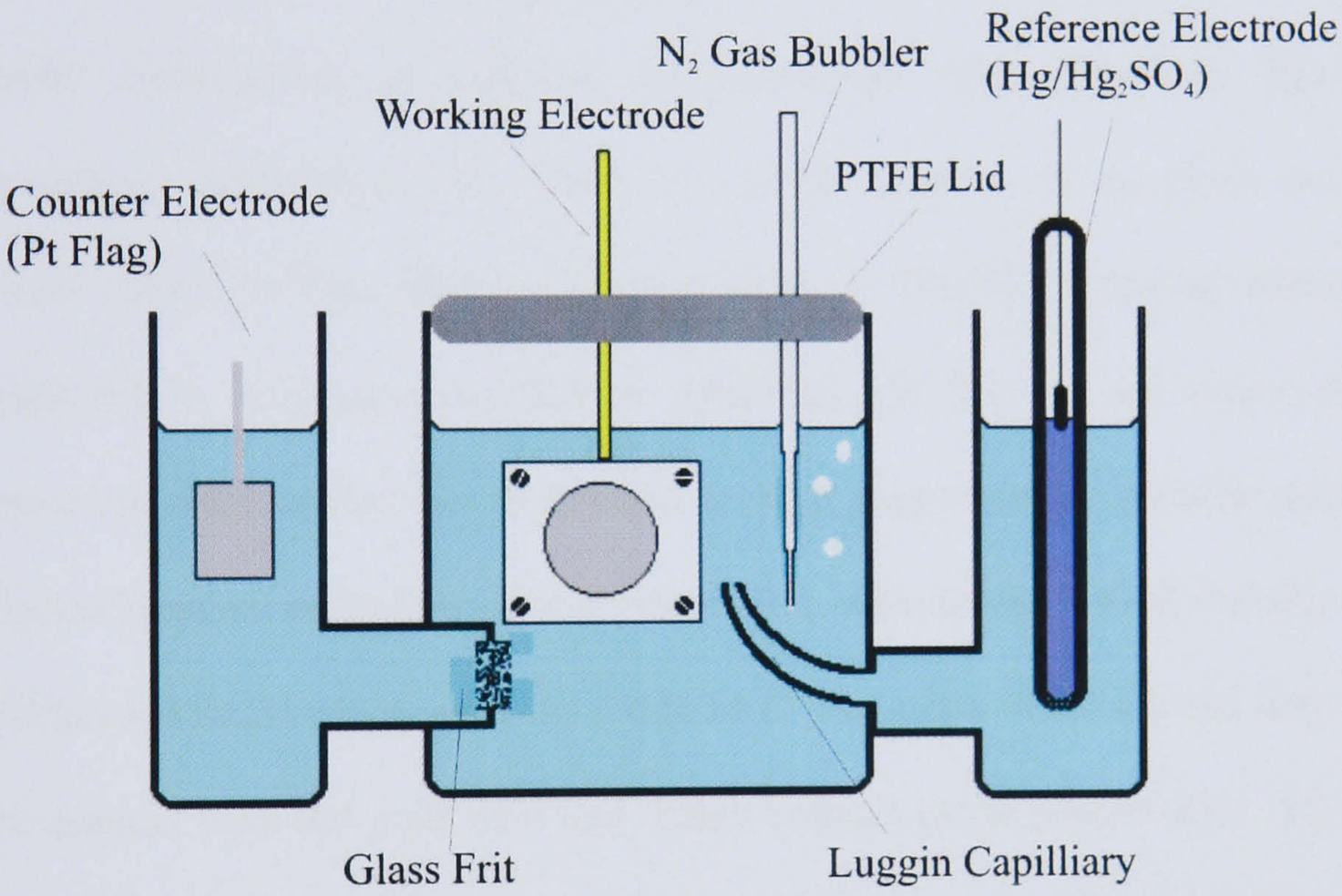

SEM images were recorded on a JEOL electron microscope and captured using digital imaging software. Electron accelerating voltages were typically 2kV; images were captured in vacuo at 10^{-5} Torr (1.33×10^{-3} Pa).

For elemental analysis, inductively coupled atomic emission spectroscopy was performed by Dr Vic Din at the Natural History Museum, London. Samples were prepared for ICP-AES by dissolving the noble metals from the surface in aqua regia

(3:1 HNO_3:HCl), accompanied by sonication to ensure all the metal was successfully dissolved.

TEM cross-sectional images were performed by Ian Brown, Biological Services, Wye College. Samples were mounted in Epon or Araldite resin and sectioned with a diamond knife. Sections were mounted on 700 mesh copper grids.

Gas diffusion electrodes and Nafion membranes were coated with platinum by sputter deposition and reactive sputtering. Typically the catalysed area was 1.5cm × 1.5cm square. The electrochemically active surface areas of the electrodes were assessed by cyclic voltammetry in standard three-electrode cell, shown in figure 2.1. The sputtering conditions were 100% O_2 or Ar plasma at as close as possible to 7×10^{-3} mbar (0.7Pa), 960 s sputtering time at 75 mA sputtering current. Surfaces sputtered in oxygen were further sputtered for 90 s in an argon plasma. This procedure was carried out to provide a small proportion of metallic platinum to aid electrochemical reduction. It was found that, without this added metallic component, electrochemical reduction of the oxide layer was often limited to the area surrounding the contact with the gold wire that makes contact to the potentiostat. The membranes showed a visual difference between the metallic areas and the oxidised layer; it was concluded that there was an electrical conduction problem across the catalyst layer that was limiting reduction of the platinum oxide layer. Oxidised platinum was reduced by holding the potential of the working electrode at 0V vs RHE or lower for around 30 mins, or by repeatedly cycling the potential between –0.02V and 1.4V vs RHE.

2.3 Results and Discussions.

In order to assess the electrochemically active surface area of platinum, a cyclic voltammogram must be recorded with the electrode in an acidic electrolyte degassed with nitrogen. A typical cyclic voltammogram of polycrystalline platinum in sulfuric acid is shown below.

Figure 2.2: Cyclic voltammogram of a typical polycrystalline platinum electrode in 0.5M H_2SO_4, N_2 bubbled, 5 mV s^{-1}, room temperature, measured vs MMSE corrected to the RHE scale.

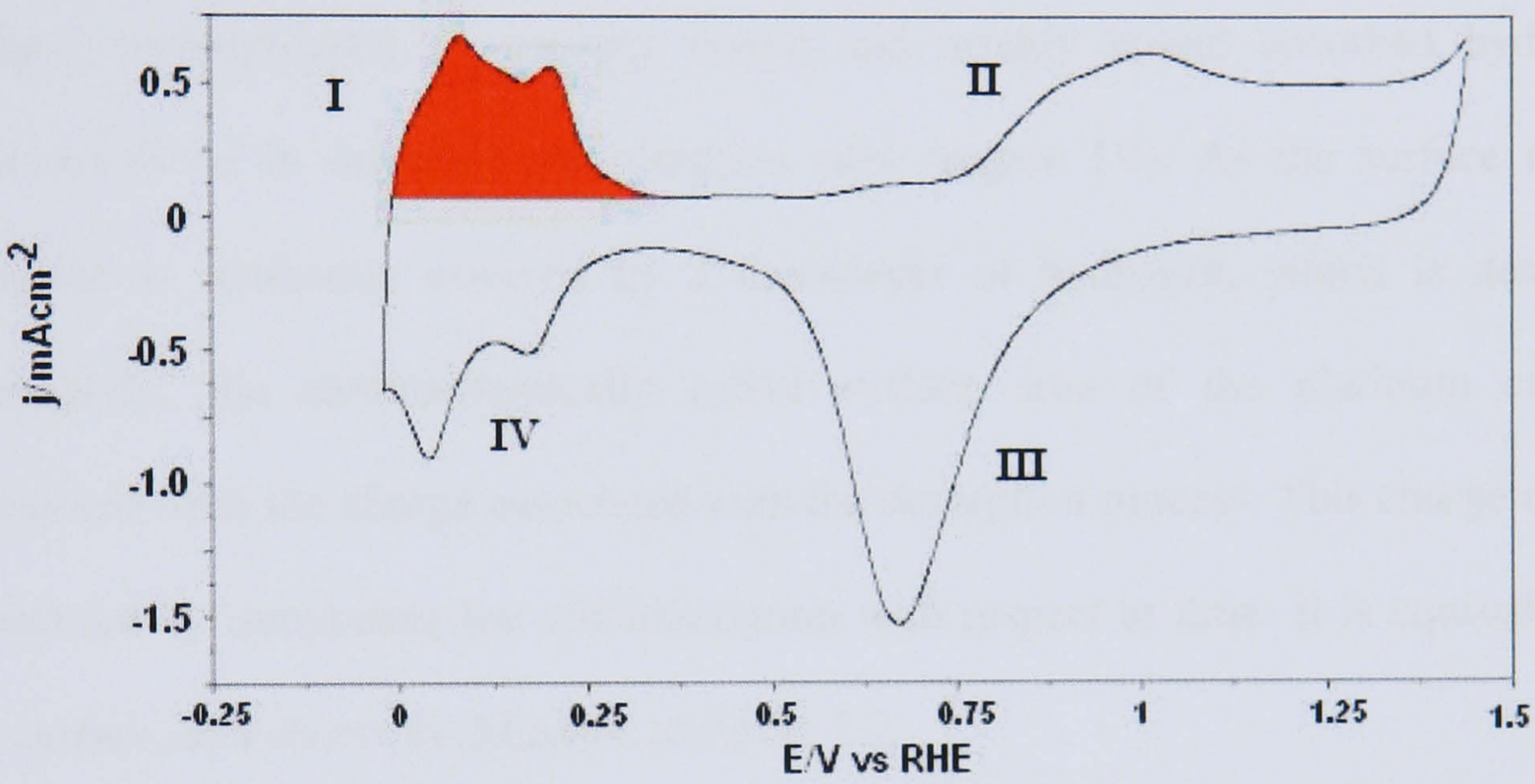

The voltammogram consists of four main features. At 0V vs RHE, the surface of the platinum is covered by a layer of adsorbed hydrogen. As the potential is swept positive, the hydrogen is oxidatively desorbed (region I). The CV shows two major peaks and one minor shoulder peak, because the hydrogen is desorbed at various potentials depending on the site of adsorption on the platinum surface. Each platinum atom is known to be capped with a single hydrogen atom. At higher potentials, no electrochemical processes take place at the electrode; the small current that flows here is associated with the charging of the double-layer capacitance at the electrode. At around 0.7V vs RHE, the electrode becomes covered in a porous oxidised layer

(region II). This layer consists initially of Pt-OH_{ads} species, then a Pt-O_{ads} species, before the onset of oxygen evolution at around 1.6V. There is a great deal of work in the literature on the structure and composition of this oxide layer. As the potential sweep is reversed, the oxide layer is reduced. There is a noticeable overpotential associated with this process; hence the oxide layer is reduced at 0.8V vs RHE, marked as region III. At lower potentials, the current again drops in the double-layer region. Finally, H^+ ions are reductively re-adsorbed in two stages on to the platinum surface, corresponding to strongly bound and weakly bound adsorbed hydrogen believed to be in different co-ordination sites (region IV). As the surface of the platinum is uniformly covered by a monolayer of hydrogen, which is desorbed oxidatively, the electrochemically active surface area of the platinum can be calculated from the charge associated with the desorption process. This charge can be calculated by integrating the voltammogram with respect to time- it is equivalent to the surface area shown highlighted in figure 2.2.

This voltammogram is typical for a bright, polycrystalline platinum electrode. The voltammetric response on single crystal platinum faces is quite different. The surface area can be calculated if the charge associated with a monolayer of hydrogen is known. On Pt (111), the figure is 240 $\mu C\ cm^{-2}$; on Pt(100) the value is 208 $\mu C\ cm^{-2}$ and on Pt (110) the figures from literature vary from 147 $\mu C\ cm^{-2}$ to 298 $\mu C\ cm^{-2}$ depending on which atoms are defined as surface atoms [47]. A hydrogen monolayer on a polycrystalline platinum electrode is fully oxidised by 210 $\mu C\ cm^{-2}$ [48, 49]. The values for polycrystalline platinum are consistent with an approximately equal dispersion of these two faces or a surface composed largely of Pt(100) [49].

Another technique for assessing the surface area of platinum electrocatalysts is carbon monoxide stripping. This technique exploits the formation of a strongly adsorbed monolayer of carbon monoxide on the surface of platinum when the electrolyte is sparged with the gas. The platinum working electrode is held at a potential below that which the CO is oxidatively desorbed and the electrolyte is degassed with nitrogen. The potential is then swept positive and the CO desorbs, giving a peak as shown dashed red on figure 2.3. Once again, the peak can be integrated to give the charge associated with a monolayer of CO. The charge per unit area is generally taken to be 420μC cm^{-2} [48].

Figure 2.3: CO stripping voltammetry of Pt-catalysed GDE in 0.5M H_2SO_4, degassed with N_2, scan rate 15mVs^{-1}, where the electrode was held at 0.3V for 20 mins whilst the electrolyte was saturated with carbon monoxide gas. The electrolyte was then thoroughly degassed with nitrogen for 40 mins before scanning the potential to anodic potentials.

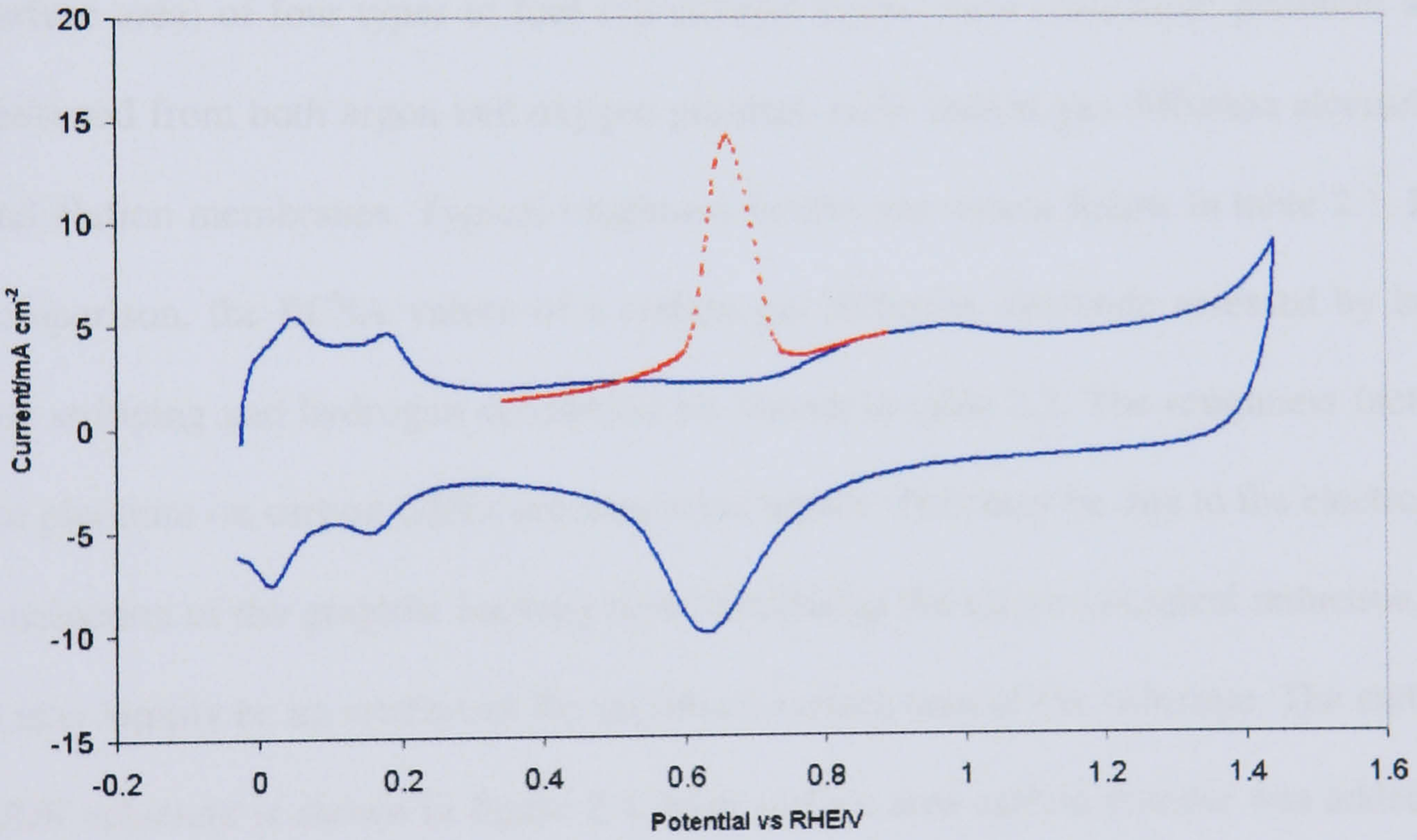

The desorption reaction is:

$CO_{ads} + H_2O \rightarrow CO_2 + 2H^+ + 2e^-$.

However studies have shown that the actual ratio of CO adsorbed to platinum is between 0.6 and 1 [50]. Also, adsorption methods for assessment of the surface area

are affected by the presence of adsorbing anions from the electrolyte. For this reason perchloric acid is often used in preference to sulfuric acid, as the sulfate counter anion is non-specifically adsorbing. A rigorous treatment of the CO stripping peak also requires subtraction of the non-faradaic, double-layer capacitive charge, and other faradiac processes from the electrolyte. A second voltammetric scan confirms complete desorption of the CO and allows calculation of the non-faradaic and background faradaic contributions to the charge passed. CO stripping can be unsuitable on certain electrode surfaces if proton desorption peaks are overlapped with the CO desorption peak, as occurs on the Pt(111) crystalline face [51].

The roughness factors (electrochemically active surface area per unit geometric surface area) of four types of fuel cell catalyst layers were calculated; platinum was sputtered from both argon and oxygen plasmas, onto carbon gas diffusion electrodes and Nafion membranes. Typical roughness factors are shown below in table 2.1. For comparison, the ECSA values of a carbon gas diffusion electrode assessed by both CO stripping and hydrogen desorption are shown in table 2.2. The roughness factors for platinum on carbon GDEs are somewhat higher. This may be due to the electronic conduction of the graphite backing layer facilitating the electrochemical reduction, or it may simply be an artefact of the increased surface area of the substrate. The carbon GDE substrate is shown in figure 2.4; high surface area carbon powder was added to provide a continuous substrate for sputtering.

Figure 2.4: Schematic of Pt sputtered onto a carbon gas diffusion electrode composed of graphitic carbon paper and a layer of Vulcan XC72R.

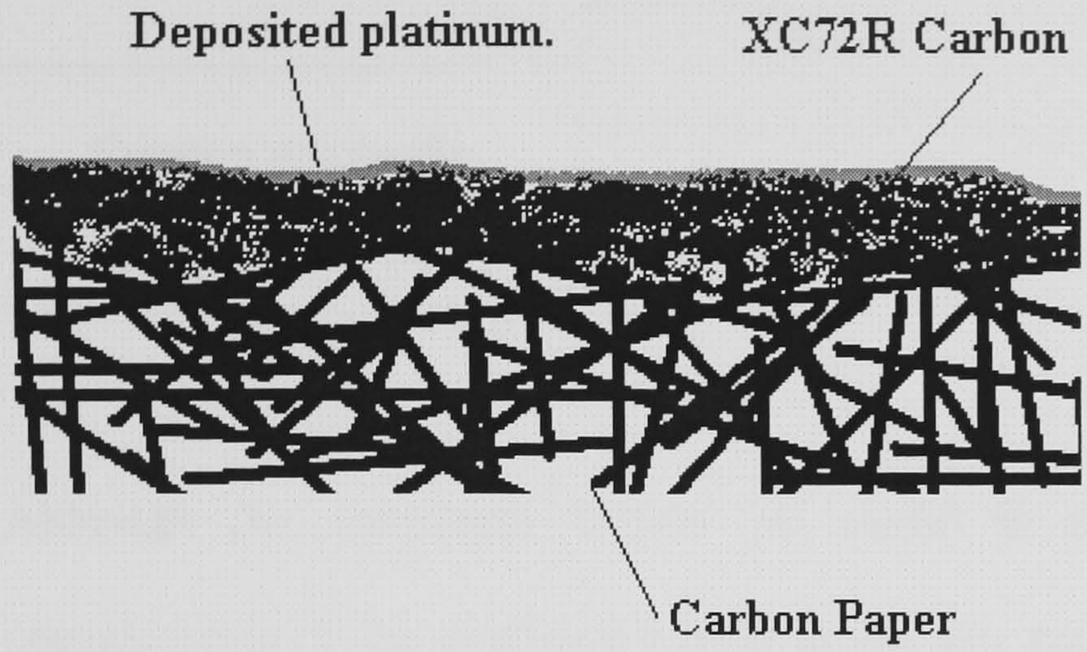

Table 2.1: Typical roughness factors for the range of electrodes employed in this work by sputter deposition method and coated substrate.

	Plasma Gas	Roughness Factor, R_f ±5
Carbon electrode	Argon	50
	Oxygen	154
Nafion membrane	Argon	31
	Oxygen	138

Although the roughness factors are stated to the nearest single $cm^2\,cm^{-2}$, a consideration of the confidence level in this key result is required. The results were arrived at through a process of optimisation of the sputtering conditions. The results were reported because they were observed to be reproducible, but should perhaps be estimated as accurate to two significant figures.

Table 2.2: Comparing CO stripping and hydrogen adsorption measures of Electrochemically Active Surface Area of a reactively sputtered Pt on carbon gas diffusion electrode. Geometric electrode area: 1.12 cm^{-2}.

	ECSA measured by Hydrogen adsorption/cm^2	ECSA measured by CO stripping/cm^2
Reactively sputtered carbon gas diffusion electrode	190.5	135.2

The discrepancies between the two figures are understandable from the literature evidence that suggests CO monolayer desorption represents a fractional coverage as low as θ=0.6 to 0.7 [50]; there is also the effect of the adsorption of the electrolyte counter ion.

SEM images of the catalyst layers are shown in figures 2.5 and 2.6 below. Figure 2.5 shows a SEM image of a sputtered platinum layer on a carbon gas diffusion electrode, cleaved with a scalpel blade. The image is taken from an angle of 70° from normal to

the surface. Images were recorded using digital imaging software on a JEOL electron microscope. The instrument image magnification is 500×, but the image has been resized. The scale bars confirm the magnification. The catalysed platinum layer is highlighted. Also of note is the XC72R high surface area carbon powder, indicated, and the fibres of the Toray carbon paper backing layer, visible in the bottom right corner of the image.

Figure 2.5: SEM image of Pt sputtered onto a carbon gas diffusion electrode, showing the catalyst, high surface area carbon layer and the carbon fibres of the carbon paper substrate. The GDE was cleaved by a scalpel blade. Magnification ×540.

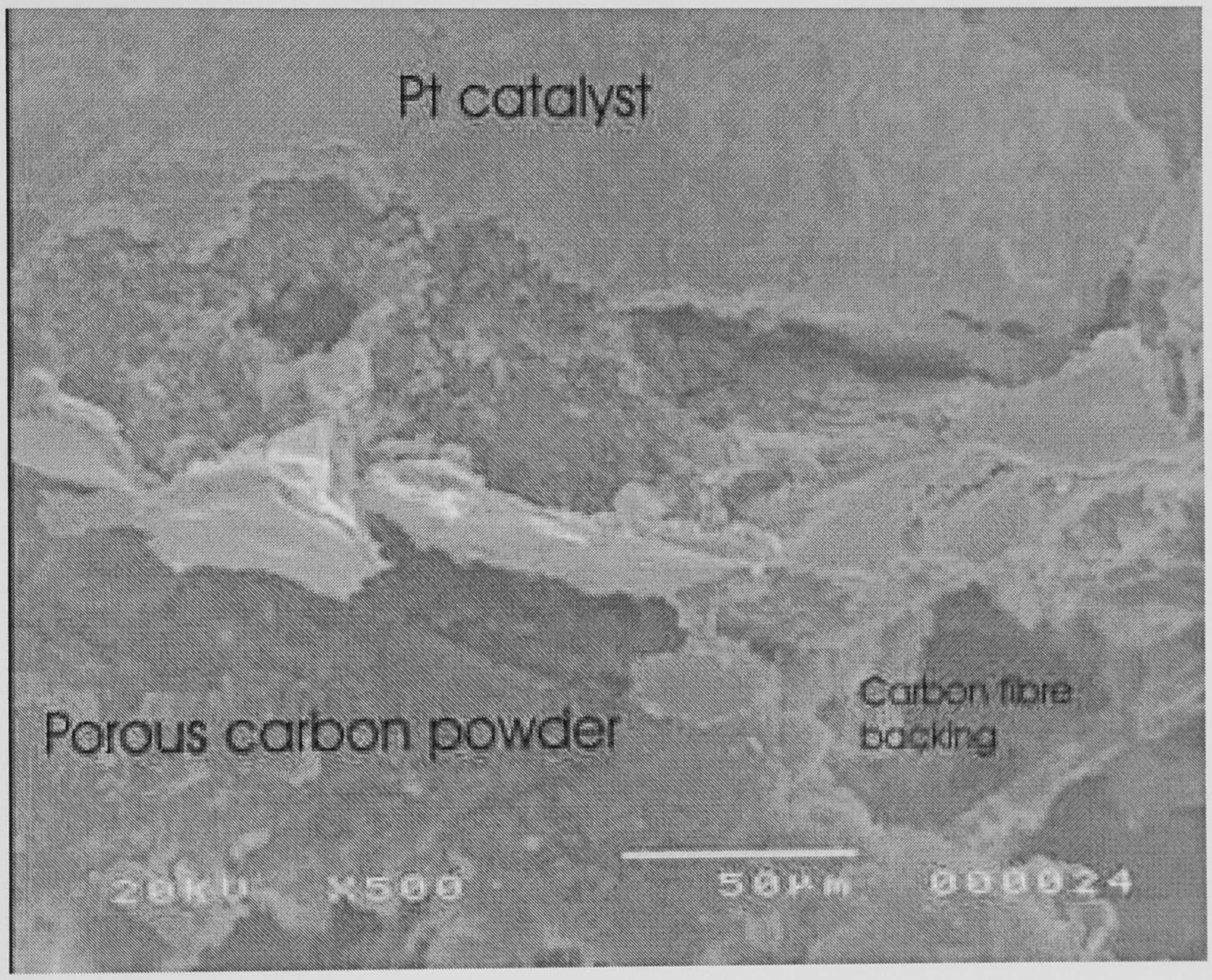

It can be seen that some of the platinum layer has been forced away from the rest of the catalyst by the cleaving process. Figure 2.6 shows a SEM image of a platinum sputtered Nafion membrane, also cleaved with a scalpel blade at 90° to the surface. Once again the image is shown at 70° normal to the surface of the membrane; some platinum material can be seen detaching along the line of the cut.

Figure 2.6: SEM image of Pt sputtered onto Nafion membrane, cleaved by a scalpel blade, showing the Nafion membrane and catalyst layer. Image recorded at 70° from normal to the catalyst surface. Magnification ×420.

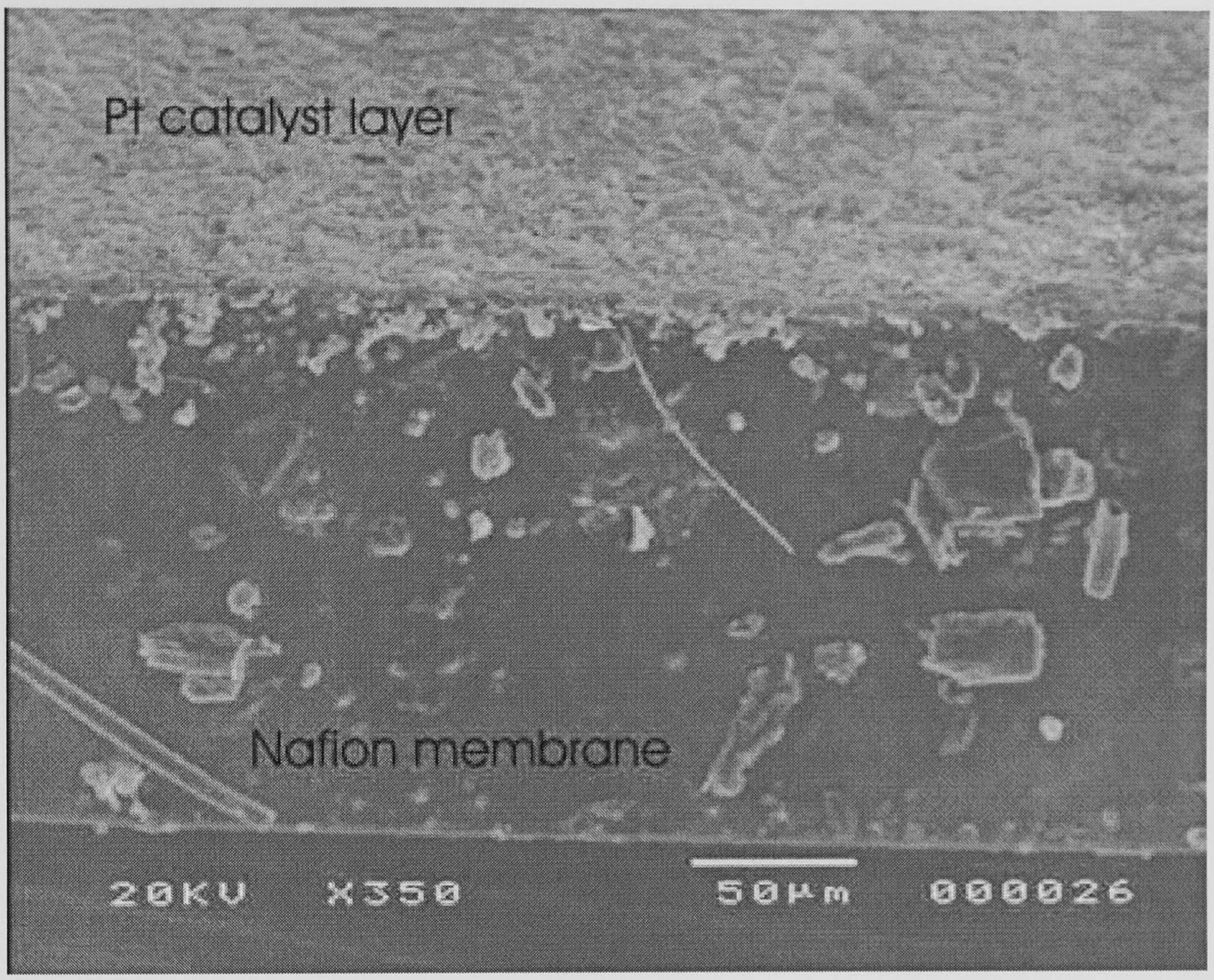

The catalyst layer is shown at higher magnification in figure 2.7 (around 15000×).

Figure 2.7: SEM of Pt sputtered on Nafion at higher magnification, cleaved by a scalpel blade, showing the Nafion membrane and catalyst layer. Image recorded at 70° from normal to the catalyst surface. Magnification ×17500.

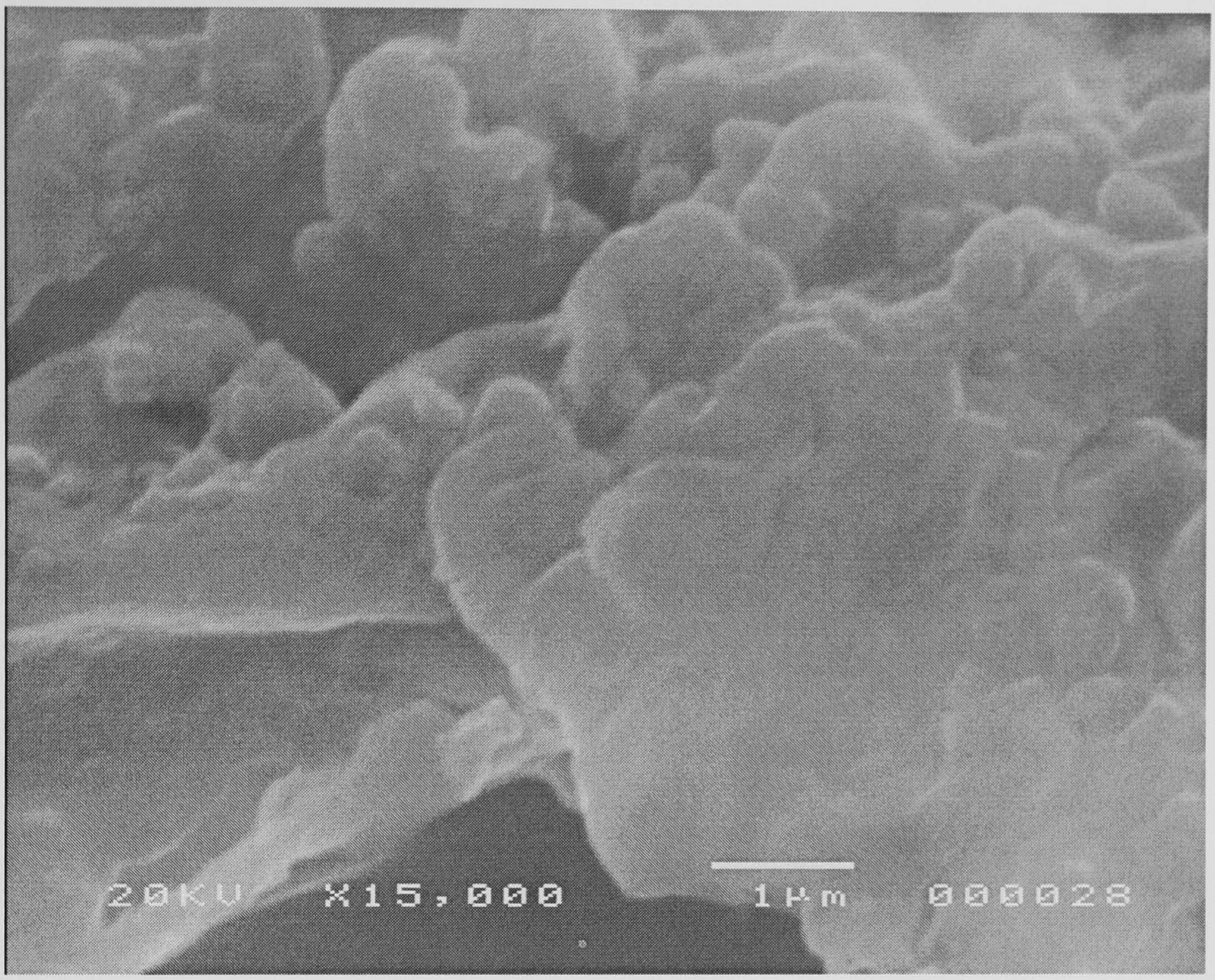

The sputter-deposited catalyst layer is clearly extremely thin, of the order of a few microns or less. There is also an extensive microstructure, with platinum particles forming agglomerates of diameter 0.5-3 μm. Even at this magnification, the image shows extensive porosity and hints at much higher surface roughness.

In order to obtain an image of the cross-sections of the sputtered catalyst layer, small areas of the membrane were embedded in Epon or Araldite resin. Ultrathin sections, approximately 90nm thick, were then sliced from the resin block using a diamond knife. These ultramicrotome sections were mounted on 700 mesh copper TEM grids. The membranes were Nafion 117 sputtered with platinum in an oxygen plasma,

reduced under flowing hydrogen at 150°C to avoid the need for electrochemical reduction in a cell (figures 2.8 and 2.9) or unreduced (figure 2.10).

Figure 2.8: Cross-section TEM of platinum catalysed membrane embedded in epoxy resin. Sections of the resin 90 nm thick were cleaved with a diamond knife. The Nafion membrane and resin support are highlighted. Magnification ×12000.

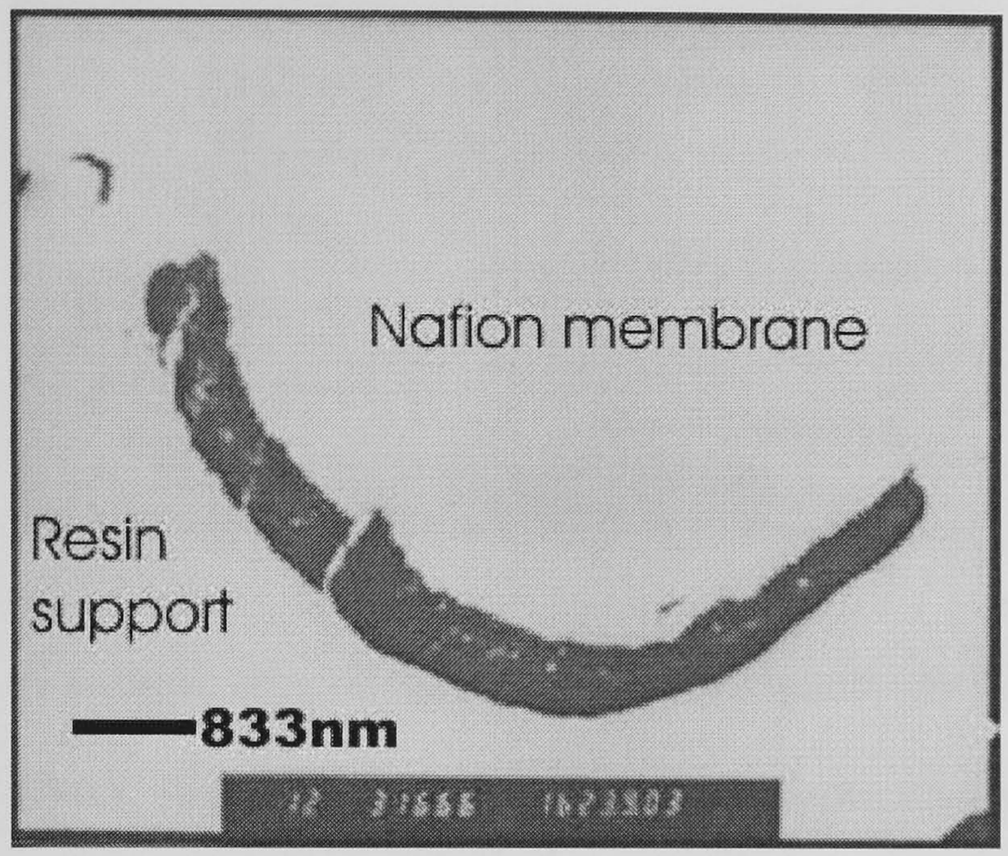

Figure 2.9: Cross-section TEM of platinum catalysed membrane embedded in epoxy resin, section 90 nm thick. The Nafion membrane and resin support are indicated. Magnification ×80000.

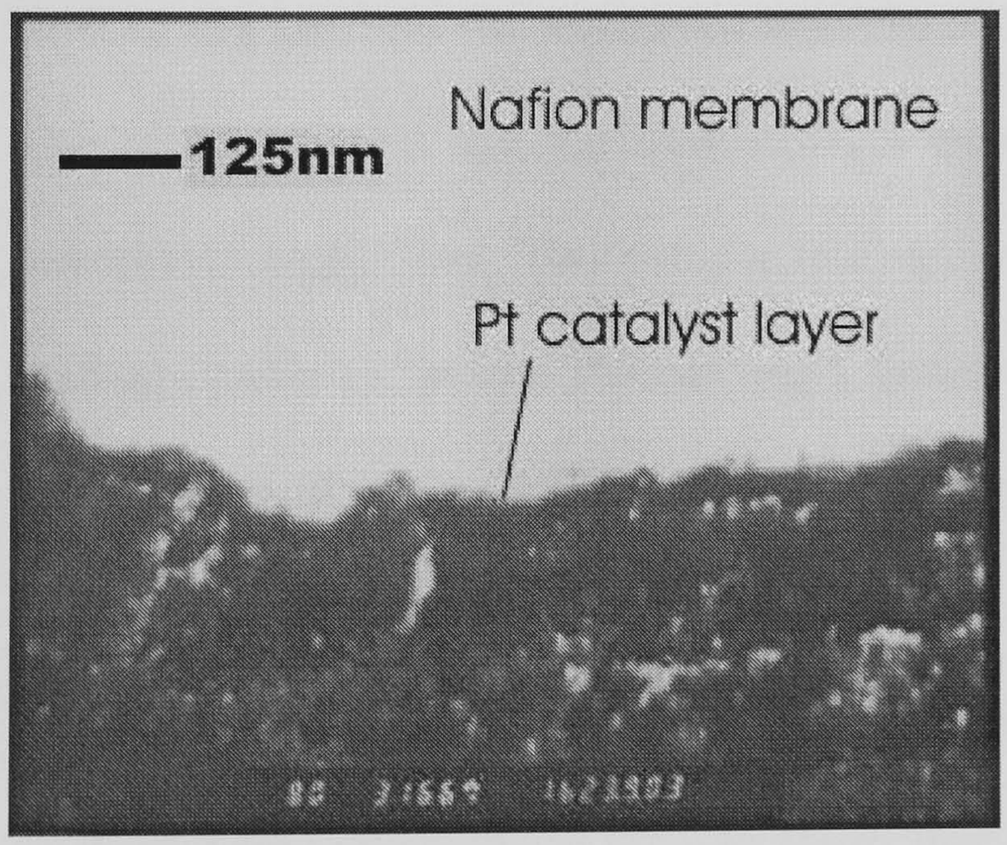

The membranes and supporting resin is indicated; the platinum metal appears as the much darker areas. The magnifications are shown in $10^3\times$ at the bottom of the micrographs and in the figure captions; scale bars are also provided.

BIBL LONDON UNIV.

Figure 2.10: Cross-section TEM of platinum catalysed membrane embedded in epoxy resin. Sections of the resin 90 nm thick were cleaved with a diamond knife. The Nafion membrane and resin support are highlighted. Magnification ×40000.

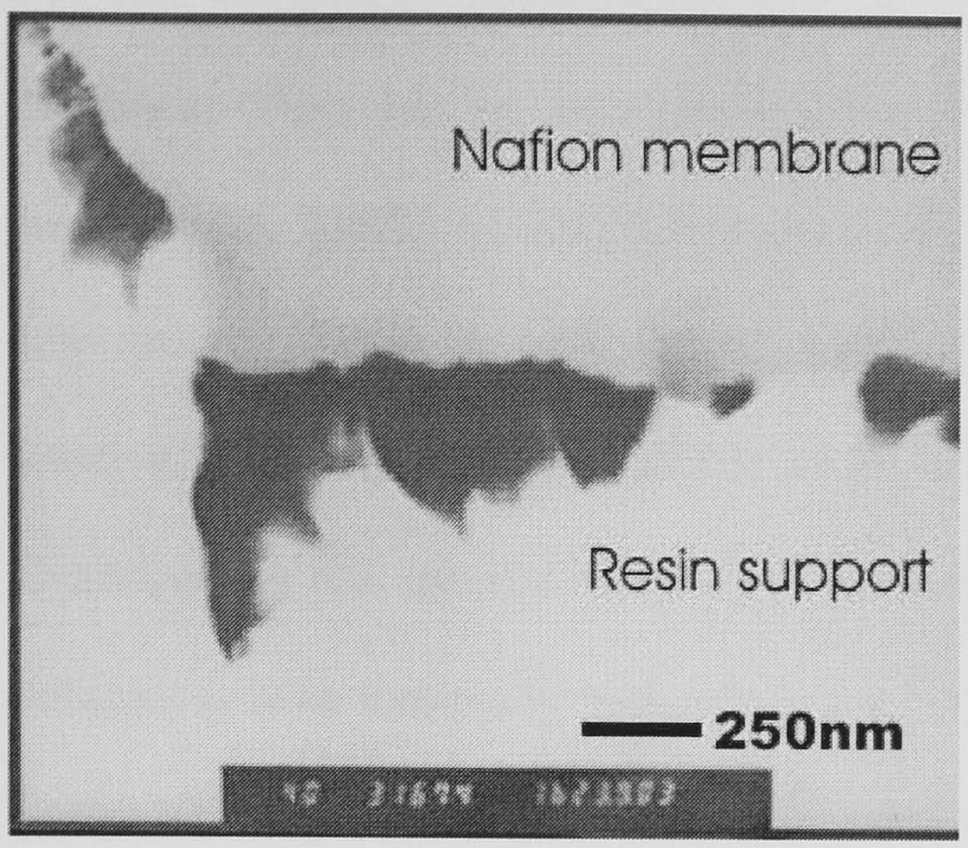

A sample area of sputtered Nafion membrane was immersed in aqua regia (3:1 conc HNO_3 : conc HCl) in order to dissolve the platinum coating. The resulting aqua regia digest was subjected to ICP-AES analysis in order to establish the typical loading of platinum for the sputtering conditions employed. The platinum loading was found to be 0.15 mg cm^{-2} for the sputtering conditions detailed in section 2.2, experimental. This result suggests that the catalyst has a specific surface area of 920 cm^2 mg^{-1}, a remarkably high figure. This value is in excess of that typically seen for unsupported platinum particles, around 300 cm^{-2} mg^{-1}, though carbon supported catalysts can show surface areas of around 1200 cm^2 mg^{-1}. As a comparison, this specific surface area is equivalent to that obtained in a Pt catalyst for which all particles have a radius of 1.5 nm. It is suggested that the reduction of a sputter deposited layer produces a structure based on extensive porosity rather than discrete particles.

The roughness factors obtained for reactively sputtered platinum are impressive, and are of the approximate magnitude expected for a working fuel cell electrode. The measured platinum loading can then be used to calculate the platinum particle size,

assuming the catalyst particles are simple spheres. The thickness of the catalyst layer was then calculated. The calculated particle diameter of 3.0 nm is extremely small, at the lower limit for an unsupported platinum particle in the fuel cell catalyst environment. Similarly, 140 ± 40 nm is a much thinner catalyst layer than seen in conventional fuel cell technologies (see introduction). Clearly the technique of reactive sputtering produces catalyst layers of high roughness at minimal thickness. Consequently the specific roughness factor, equal to the roughness factor per unit volume, **a,** is an extremely high value, $\mathbf{a} = (1.1 \pm 3) \times 10^6$ cm^{-1}. This figure is several orders of magnitude higher than the value calculated for a proprietary fuel cell electrode from E-TEK inc. $\mathbf{a} = 1.59 \times 10^3$ cm^{-1} based on data reported by Hirano *et al* [52]. However, these values for thickness and particle size are inferred indirectly. The TEM and SEM micrographs give some clues as to the microstructure of the catalyst layer. The SEM images (figures 2.5, 2.6 and 2.7) do not readily show the catalyst layer thickness as the cleaving method employed did not lead to a clean cross section. The highest magnification SEM available shows clusters of platinum of a somewhat larger size than the calculated particle size, but there appears to be extensive porosity and further internal surface roughness. The TEM images show thin layers of platinum that are surprisingly non-uniform on the sub-micrometer scale. It may be that some material detaches slightly from the membrane during the embedding process in the resin. The membranes are mounted by repeatedly attempting to saturate the sample with the epoxy components, so some deformation may have taken place. TEM micrographs at higher resolution also show an extensive microstructure (figure 2.9) and porosity. The sections are around 90nm thick, so the presence of light patches of direct electron transmission on the image show a high degree of porosity and a low

density of material. It is this extensive porosity that contributes to this extremely high roughness at low platinum metal loading.

These calculated particle sizes are particularly small, though they are only slightly lower than the particle sizes reported by Maya et al [27]. For platinum produced by sputtering from an argon/oxygen mixture and reduced in 4% hydrogen in argon they reported crystallite sizes of 5-10 nm using X-ray diffraction line-broadening. They also found an enhancement in the roughness factor for electrochemical reduction of the sputtered platinum oxide films ($R_f = 150$) compared with hydrogen reduction methods ($R_f = 115$). In this investigation the catalysts investigated electrochemically for surface area were reduced electrochemically, while the membranes sectioned for TEM imaging were reduced in flowing hydrogen at elevated temperature. There may be some agglomeration associated with this process, giving lower roughness factors. It may also be the case that hydrogen reduction at elevated temperatures contributed to the non-uniform thickness of the catalyst layer seen in the TEM micrographs. However, it appears from figure 2.10 that a figure for the catalyst layer thickness of 140 nm is a reasonable mean thickness. The platinum membrane shows some peaks and areas of increased thickness, and some areas of minimal loading.

An estimate of platinum catalyst layer thickness is based on porosity and loading, and confirmed by the TEM images requires a necessarily broad error estimate, hence the lower confidence value of ± 40 nm.

2.4 Conclusions.

Reactive sputtering has been shown to produce extremely thin, high surface area catalyst layers for PEM fuel cells at low loading. Specific catalyst roughness values have been as high as $\mathbf{a} = (1.1 \pm 3) \times 10^6\ m^{-1}$, orders of magnitude higher than those

reported for conventional E-TEK fuel cell electrodes. Reactive sputtering therefore satisfies the aims discussed in chapter 1 (introduction); the surface area of a minimal amount of platinum has been maximised and the catalyst has been located in an extremely narrow region on the surface of either the carbon gas diffusion electrode or the Nafion membrane. Reactive sputter deposition is therefore considered a suitable route to platinum fuel cell catalysts that satisfies the aims of this thesis.

Chapter 3: Conductivity of Nafion Membranes.

3.1 Introduction.

Nafion is a physically robust material. It can be cast into flexible polymer sheets in a range of thicknesses for fuel cell applications and use in electrochemical reactors such as chlor-alkali cells. Because of the entirely fluorinated structure- the polymer backbone has the structure of PTFE- the material is chemically inert. The polymer has a glass transition temperature (T_g) of around 130°C, depending on processing method. Nafion begins to degrade at temperatures between 175°C-240°C [53].

Sputter deposition and reactive sputter deposition produce a thin layer of platinum, which forms in the low-pressure conditions of the plasma. Platinum atoms are ejected from the target by the impact of argon ions at high energy, accelerated by a voltage typically around 100-150V, with a flow of ions giving a current of around 2.5-7.5 mA cm^{-2} at the target. To liberate individual atoms of platinum from a metallic target, ions of the plasma gas necessarily collide with the metallic target at high energy. The resultant sputtered platinum travels through the low-pressure platinum and impacts upon the surface of the substrate. The rise in temperature of the substrate as a whole is not substantial, as the total amount of material deposited is not large. However, the localised thermal effect of the deposition process can be observed. Unsecured Nafion membrane substrates curl to a convex shape when sputtered with platinum; this is believed to be due to changes in the Nafion structure at the surface. It may be that the localised heating effect causes accelerated drying of the surface Nafion. Throughout this work membranes were dehydrated at around 80°C, 60 mbar (6kPa) for 30 mins, before sputtering, but it is possible that residual hydration may remain.

A study by Yoon et al [54] is perhaps relevant. Yoon and co-workers investigated approached to preventing methanol crossover in direct methanol fuel cells (DMFCS), which causes depolarisation losses by oxidising on the intended cathode. The authors exploited the resistance to methanol crossover of palladium. A thin layer of palladium (up to 100 nm) was sputtered onto the surface of a Nafion-117 membrane, and the methanol permeation was measured in a methanol diffusion cell. The proton conductivity was also measured, and was found to decrease approximately linearly with the thickness of palladium, independent of methanol concentration. The authors did not speculate on the mechanism for the reduction in conductivity, though they refer to the hydrogen absorption properties of palladium. Their method of measurement involved placing platinum electrodes either side of the composite membrane and assessing the AC impedance response. This approach would not, however, distinguish conductivity from proton transport through the palladium from electronic conductivity by metallic platinum. In any case, the work reports a figure for Nafion resistivity of 48.5 Ω cm compared to a quoted (but not referenced) literature value of 12.5 Ω cm. It is possible that the effects of sputter deposition have contributed to this marked reduction in conductivity.

The conductivity of fuel cell membranes cannot easily be assessed by measuring the DC resistance of a membrane-electrode assembly. The membrane electrode assembly features two electronic conductors either side of an ionic conductor, with a number of separate resistances in series, which must be resolved. The ionomer must be hydrated and electrochemical reactions have to take place on the catalysts of each electrode for a DC current to pass through a MEA.

Polymer electrolyte conductivity is instead assessed by alternating current techniques. The impedance of an electrical circuit is given by:

$$Z(f) = \frac{E(t)}{i(t)}$$

Where $E(t)$ is the variation of potential difference with time, and $i(t)$ is the current response. Impedance and resistance are related concepts, but impedance can be defined as the sum of the resistance and reactance:

$$Z = (R - jX_C) \text{ where } j = \sqrt{-1}$$

Impedance response is assessed using frequency response analysis (FRA) instruments. Interpreting AC impedance can give information about the resistances and capacitances present in an electrical circuit. The impedance response of electrochemical cells has been extensively studied, and can give information on the interfacial capacitances and reaction kinetics in simple systems. The technique has also been applied extensively to the study of fuel cells.

The impedance response of a system can be resolved into an in-phase component and an out-of-phase component:

$$Z(f) = Z'\sin(2\pi ft) - Z''\cos(2\pi ft)$$

A complex-plane plot of Z` on the real, horizontal axis and –Z`` on the imaginary, vertical axis is known as a Nyquist plot. The overall impedance is then given by a vector from the origin.

The interpretation of impedance responses depends on modelling the system being studied using an equivalent circuit which contains the resistances and capacitances found in a real system. The impedance response of a resistor in series with a capacitor

appears on a complex plane plot as a vertical line with normal to Z`=R, with Z`` given by:

$$-Z'' = \frac{1}{2\pi f C_d}$$

The capacitance is given by the inverse of the gradient of a plot of Z'' against f^1.

The impedance of a resistor and capacitor in parallel appears on a Nyquist plot as a semicircle intercepting the Z' axis twice, once at Z'=R, at the low frequency limit of the range, and again at Z'=0 at the highest frequency where the capacitance behaves as a short-circuit.

A process occurring at a standard working electrode in an electrochemical cell is typically modelled using a Randles circuit [55], shown below in figure 3.1. The charge transfer resistance is modelled as R_{CT}; C_{DL} is the double layer capacitance; the uncompensated solution resistance is shown as R_U. A further impedance response, the Warburg impedance, shown as —**W**—, is added to take account of the frequency dependant resistance behaviour of electrochemical reactions with low R_{CT} due to rapid electron transfer kinetics.

Figure 3.1: A Randles equivalent circuit. Typical impedance equivalent circuit used for a working electrode in a standard three-electrode electrochemical cell, with uncompensated solution resistance (R_U), charge transfer resistance (R_{CT}), double layer capacitance (C_{DL}) and Warburg impedance.

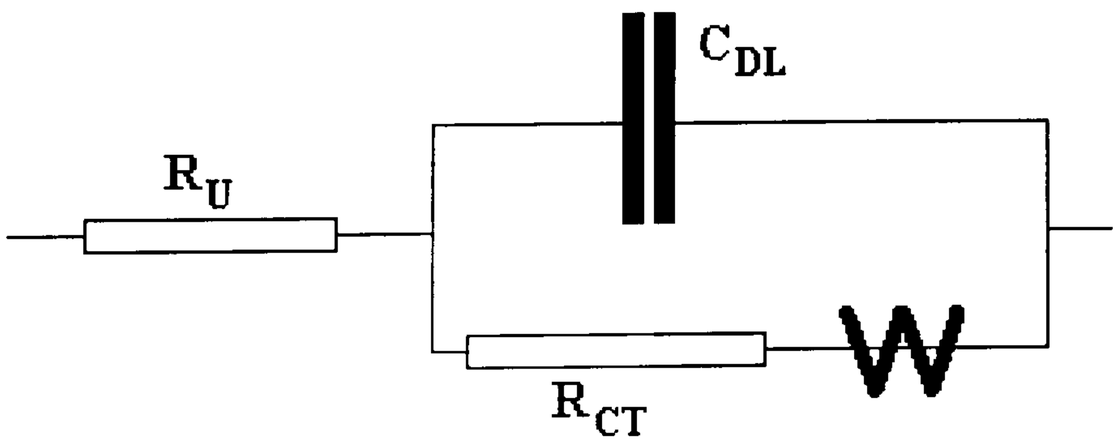

There is a substantial body of work in the literature discussing the application of AC impedance to the study of the reactions in, and properties of, fuel cells, as discussed by Muller, Frank, Colborn and Wilkinson [56] and reviewed by Selman and Lin [57].

For fuel cell studies, the system has two electrodes and an electrolyte. A simple equivalent circuit for AC impedance studies is suggested in figure 3.2.

Figure 3.2: A proposed simple equivalent circuit for fuel cell impedance studies with electrolyte resistance (R_{PE}), charge transfer resistance (R_{CT}) and double layer capacitance (C_{DL}).

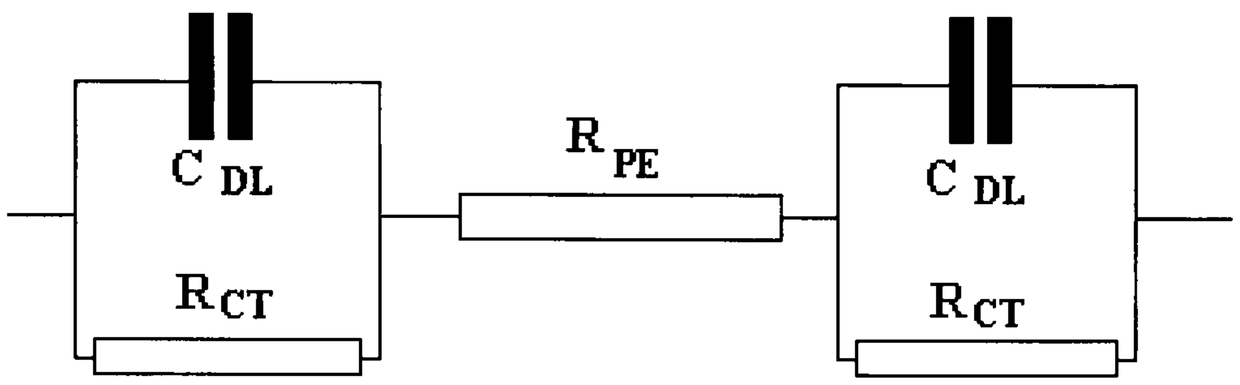

The circuit features two charge transfer resistances and interfacial capacitances in parallel, and an electrolyte resistance in series. In this work, AC impedance was used to probe the ionic conductance of the polymer electrolyte membrane. The R_{PE} (polymer electrolyte resistance) value is extracted from the impedance by finding the high-frequency intercept of the complex-plane plot with the horizontal axis (the real impedance axis). At the higher end of the frequency spectrum, the current associated with a perturbation of the potential does not pass through the R_{CT} components whilst the capacitances C_{DL} partially charge and discharge. During the short charging times available at high frequency the capacitances do not become resistive so the series resistance is dominated by R_{PE}. It is then possible to calculate the conductivity of the membrane of a fuel cell MEA from this high frequency intercept of the Z' axis.

Nafion proton conductivity varies widely, particularly with variations in ionomer hydration [58]. At maximum hydration, the conductivity of Nafion is given as $83 \times 10^{-3}\ \Omega^{-1}\ cm^{-1}$ by DuPont's own product information [59], data taken from

Zawodzinski *et al* [60]. Impedance studies of the conductivity of the membranes was originally measured by a two-electrode impedance measurement [60, 61]. To obtain a more accurate assessment of the ionomer conductivity, a four-electrode method was employed by Cahan and Wainwright [62] and Sone et al [63] to remove the effect of cable and contact impedances and to isolate the membrane impedance. A variety of experimental arrangements have been employed. Halim et al [61] sandwiched several layers of membranes between polished platinum sheets in a heated, sealed cell. Silva, De Francesco and Pozio [64] mounted membranes between graphite current collector blocks and uncatalysed carbon paper electrodes.

In the work reported in this chapter, the effect on the conductivity of Nafion membranes was assessed by comparing the impedance responses of a reactively sputtered membrane with that of an identically prepared unsputtered membrane. MEA impedance was initially measured by a four-electrode method with contact to the MEA made via the current collectors. An enhanced method was developed employing reference electrodes in contact with the membrane in close proximity with the electrodes.

3.2 Experimental.

Nafion membranes were prepared by boiling in 3 wt% H_2O_2 (VWR) for 30 mins, in 0.5 mol dm^{-3} H_2SO_4 (VWR) for 30 mins, then in several changes of Millipore water for 1 hr. They were then dehydrated by heating in a vacuum oven at 80°C, 75 mbar (7.5kPa) for 2hrs. Reactively sputtered membranes were coated in Pt for 960s on each side. For full details of the reactive sputtering process, see chapter 2, experimental section. The platinum coating was removed by dissolution in aqua regia (3:1 concentrated HCl: concentrated HNO_3, both VWR). In order to ensure continuity of

treatment the unsputtered membranes were also treated with aqua regia. Membrane electrode assemblies were formed by hot-pressing off the shelf Johnson Matthey platinum on carbon paper electrodes either side of the membranes at 154°C, 75 kg cm^{-2} (7.36 MPa). The MEAs were placed in a full fuel cell manufactured in house. The fuel cell incorporates graphite current collectors with a machined serpentine flow field. Reactant gases were supplied via mass flow controllers (Bronkhorst, Ruurlo, Netherlands) and humidified by a Nafion gas drying tube (PermaPure, Toms, NJ) fed with heated water. The impedance response of the cell was assessed using an Autolab potentiostat (Ecochemie, Utrecht, Netherlands) frequency response analyser. Contact with the MEA was made either through the current collectors or via reference electrodes in contact with the membrane. Reference electrodes were manufactured by sealing gold wire (60 μm diameter, Goodfellow, UK) into soda glass tubes, then adding high surface area palladium by abrasion. A 20μl drop of Nafion emulsion in water (5wt%, Aldrich) was added to the tip of the reference electrode. The reference electrodes then made contact with the membranes in gaps in the catalysed electrodes (see figure 3.3).

Figure 3.3: Position of high surface area Pd reference electrodes in fuel cell test apparatus.

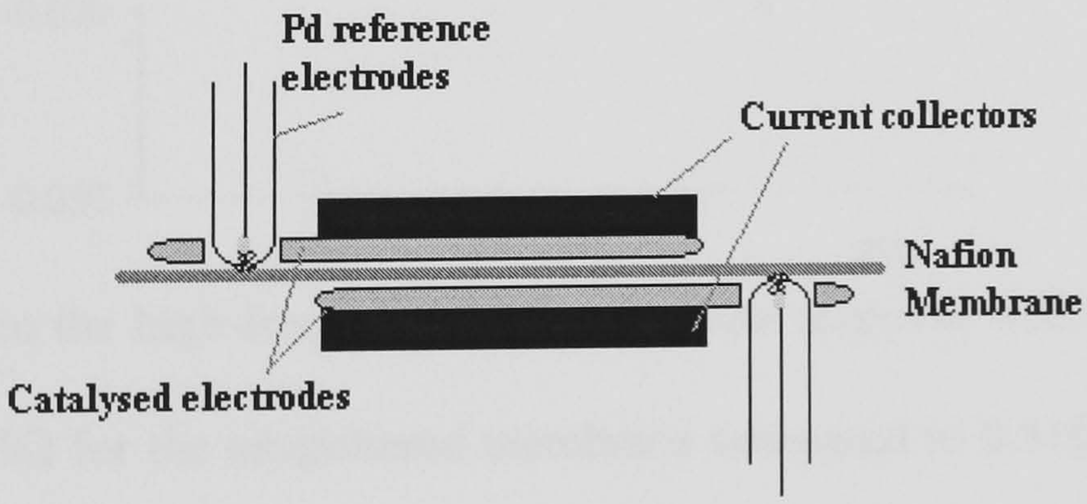

3.3 Results and discussions.

An initial investigation into the effect of reactive sputtering on Nafion conductivity was carried out by measuring the AC impedance response of two MEAs mounted in a fuel cell. Data was recorded between 100 kHz and 100 Hz. Figure 3.4 below shows the impedance response; the data are somewhat truncated in the low and high frequency regions to show the high-frequency intercept of the impedance response with the Z' axis.

Figure 3.4: Detail of impedance response with unsputtered membrane (open circles) and sputtered membrane (crosses) at high frequency. Decadic frequencies indicated; 4=10kHz, 3=1kHz. Cell supplied with hydrogen, humidified at 70°C, cell at 65°C.

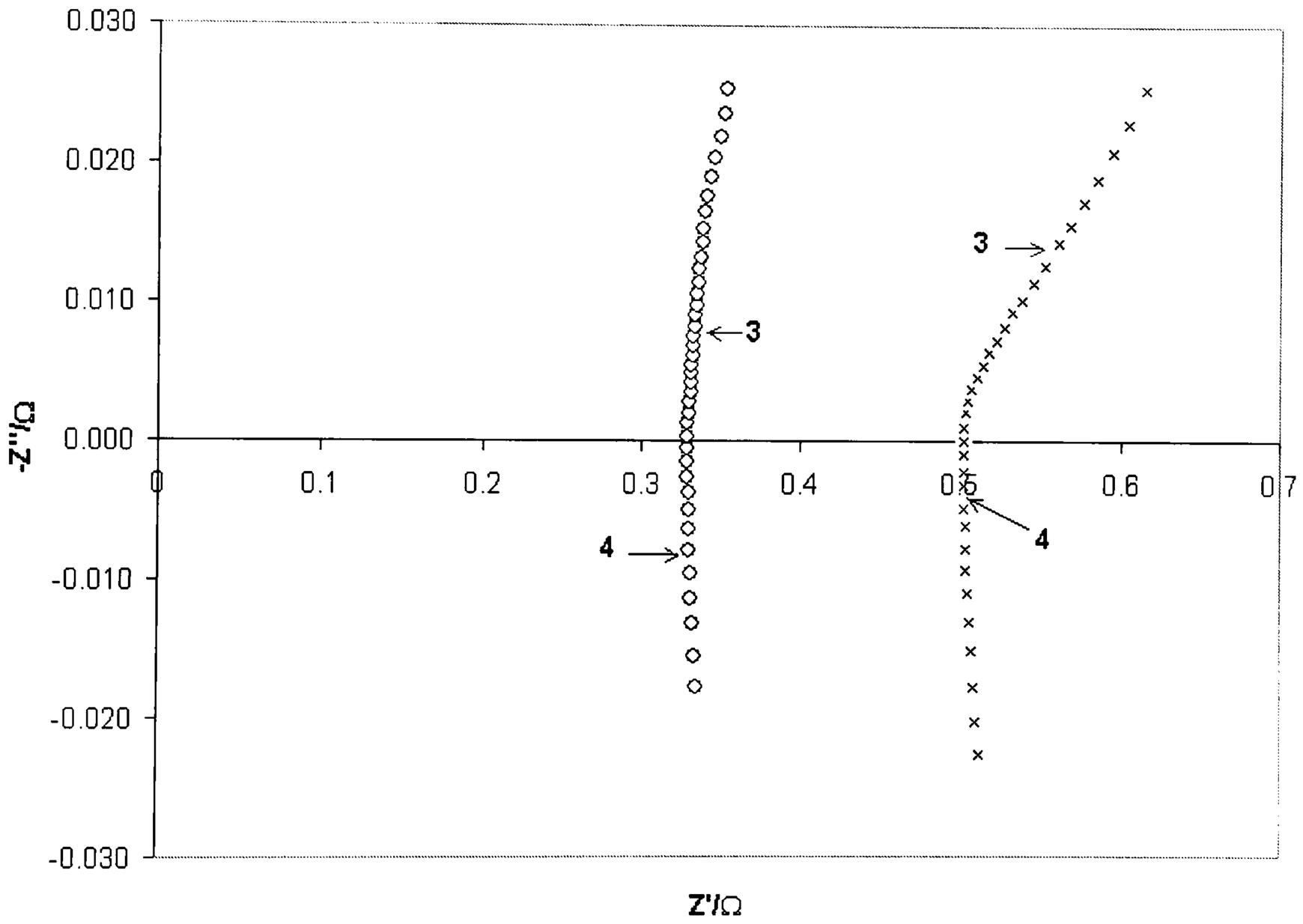

From the high-frequency intercept of the response with the Z` axis, the resistance is 0.33Ω for the unsputtered membrane compared to 0.51Ω for the reactively sputtered membrane. These results give conductivity figures of $24.2 \times 10^{-3}\ \Omega^{-1}\ cm^{-1}$ (unsputtered) vs $15.7 \times 10^{-3}\ \Omega^{-1}\ cm^{-1}$ (sputtered). Both these figures would represent relatively low conductivity for a well-hydrated Nafion membrane. However, these

measurements are taken with all four electrodes of the FRA connected to the current collectors either side of the fuel cell.

A more appropriate way to measure the impedance of a fuel cell MEA is to sense the potential either side of the membrane using reference electrodes. This eliminates series resistances within the current collector hardware and gives a clearer estimate of the potential at the interface between the catalysed electrode and the membrane. A better estimate of membrane impedance can therefore be made.

Figure 3.5 below shows the plot of Z` vs –Z`` between 10kHz and 100Hz of the unsputtered Nafion membrane in a fuel cell. The unsputtered membrane was mounted between high surface area Pt on carbon electrodes (Johnson Matthey) and placed in a fuel cell as described above. The membrane was supplied with hydrogen gas (7.5ml min^{-1}), humidified at 70°C to both sides. The cell was heated to 65°C. Humidified gas was allowed to flow for 90 min before performing any experiment in order to ensure the complete humidification of the membrane.

Figure 3.5: Impedance response with unsputtered membrane in fuel cell with Pd reference electrodes in situ. Decadic frequencies labelled; 4=10kHz, 3=1kHz. Cell supplied with hydrogen, 7.5 cm^3 min^{-1} to both sides, humidified at 70°C, cell at 65°C.

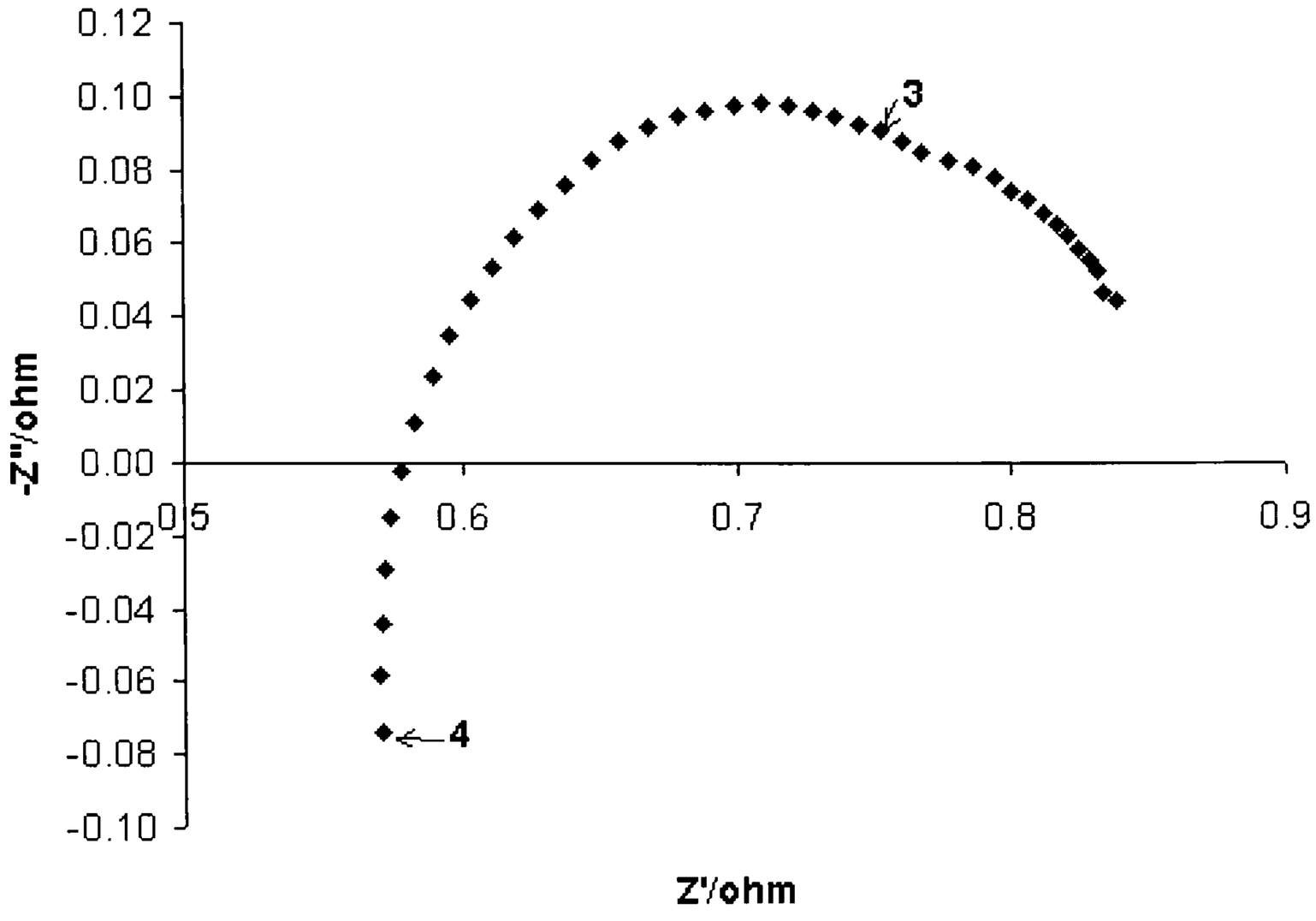

The complex plane plot shows a semicircle as might be expected from the equivalent circuit shown above. The high-frequency termination of the semicircle intercepts with the membrane at 0.583Ω, giving a resistivity of 73.0 Ω cm, equivalent to a conductivity of 13.7×10^{-3} Ω^{-1} cm^{-1}.

Figure 3.6 below shows the impedance response for a sputtered membrane with Pt removed by aqua regia dissolution. The membrane was mounted between identical high surface area Pt electrodes in a fuel cell at 65°C, supplied with hydrogen humidified at 70°C at 7.5 cm^3 min^{-1} to each side.

Figure 3.6: Impedance response with sputtered membrane in fuel cell with reference electrodes in situ. Decadic frequencies labelled; 4=10kHz, 3=1kHz. Cell supplied with hydrogen, 7.5cm^3 min^{-1} to both sides, humidified at 70°C, cell at 65°C.

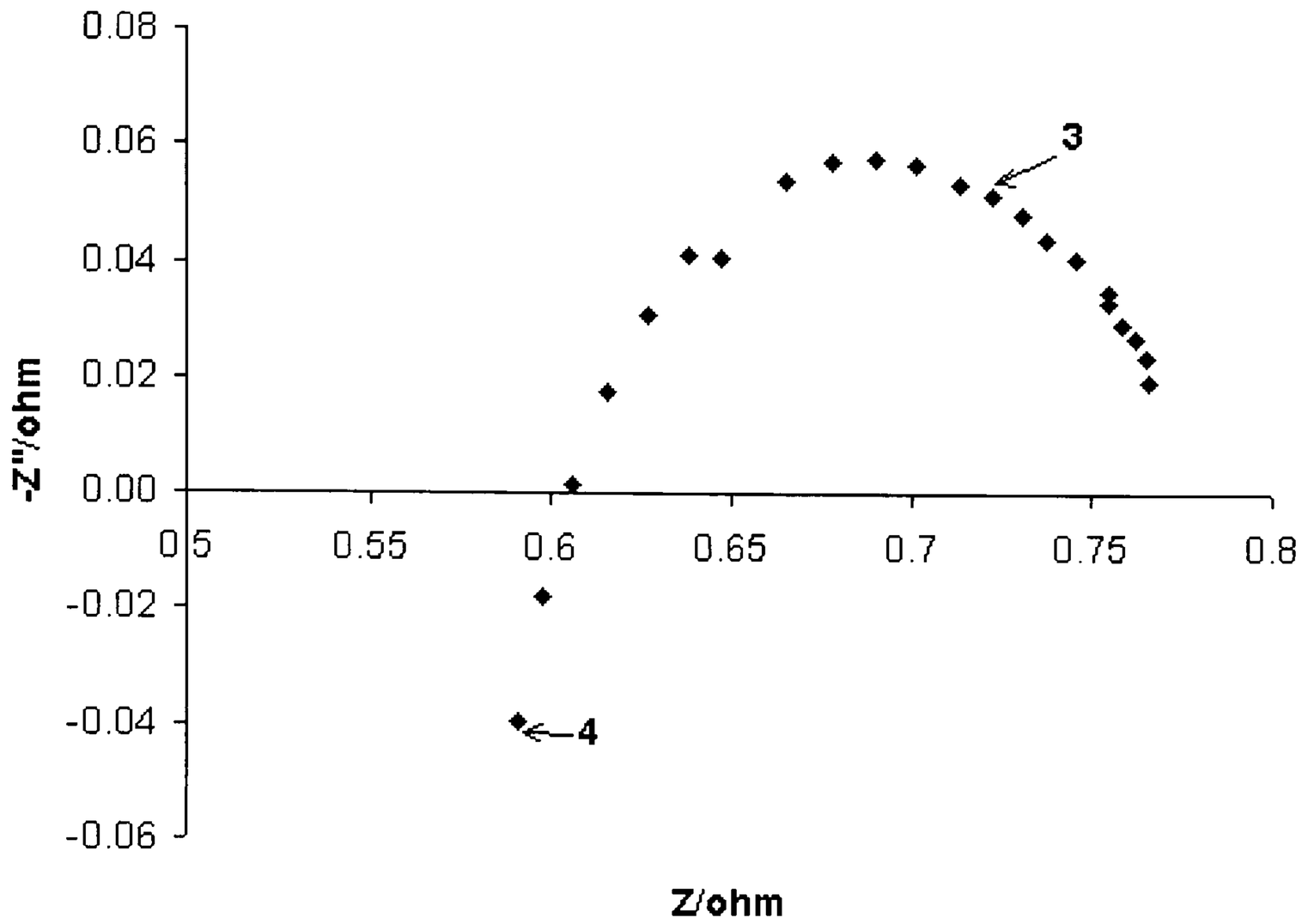

Once again the complex plane impedance plot shows a semicircle, with a high frequency termination at 0.61Ω, giving a conductivity of 13.1 ×10^{-3} Ω^{-1} cm^{-1}.

The difference in conductivity seen in latter experiments with in-situ reference electrodes is smaller than that seen with the connections made solely through the current collectors of the fuel cell, suggesting that the reference electrode technique isolates resistances other than the value we wish to measure. In addition, the conductivity measurements seen with the reference electrode method are smaller than those calculated from the current collector impedance, and significantly smaller than the manufacturer's conductivity values [59]. Significantly, both methods give a higher resistance value for the MEAs with sputtered membranes compared to the unsputtered membranes.

It is surprising that the conductivity values obtained with the reference electrodes are smaller than the conductivity estimates made in the earlier experiment. There are a

number of contact resistances in series that would complicate impedance measurements made on the fuel cell current collectors, though the use of palladium reference electrodes in contact with the membrane provides a relatively novel and convenient method of sensing the potential either side of R_{PE}, the polymer electrolyte resistance shown in the equivalent circuit (figure 3.2). The conductivity of well-hydrate Nafion is such that the contribution of the resistance due to the membrane may account for a limited proportion of the overall resistance of the MEA, current collector and electrode contacts. Therefore a four-electrode impedance method must seek to minimise the contributions from other resistances. It may be that localising Pd reference electrodes on the surface of the membranes is an enhancement of the experimental method of determining the membrane conductivity in a fuel cell environment, but that an artefact of this experiment has contributed to the lower values seen here. The section of Nafion membrane contacted by the reference electrodes is at a small remove from the serpentine flow field of the graphite blocks. Therefore this part of the MEA may be less well hydrated than the section between the flow fields, which contain the humidified reactant gases.

With both experimental methods, the conductivity value obtained for the unsputtered membrane was lower than the manufacturers' value of $83 \times 10^{-3}\ \Omega^{-1}\ cm^{-1}$. This may be due to the resistance value being complicated by other serial resistances not eliminated by the use of either palladium reference electrodes or four point impedence measurements. Furthermore it is possible that this experimental arrangement does not give optimum conditions for maximum membrane conductivity. The results of Zawodzinski *et al* [60], from which the DuPont figures were taken, were obtained by suspending the membrane over an aqueous LiCl solution in a sealed cell in a temperature-controlled bath for four days.

However, both experimental approaches give reduced conductivity for the Nafion membrane reactively sputtered with platinum when compared with the unsputtered membrane. It is clear that there is a detrimental effect on membrane conductivity due to the effect of the sputter deposition process. The reduction in the membrane conductivity is tentatively ascribed to local degradation arising from the heating effect of the sputtered target atoms. There may be a need to seek an alternative catalyst layer structure that preserves the high surface area at minimal thickness seen in chapter 2.

3.4 Conclusions.

Sputter deposition remains an effective approach to depositing a high surface area platinum catalyst at low platinum loading, but with direct deposition of catalyst on the membrane comes a penalty of increased electrolyte resistance. The ohmic resistance of the fuel cell is the factor which limits fuel cell performance at intermediate potentials on a polarisation curve (see introduction). It can be seen that small differences in membrane resistivity can make a sizeable difference to the current density of a PEM fuel cell at the potentials at which fuel cells might typically operate.

Chapter 4: Indirect Deposition of Sputtered Platinum Catalysts.

4.1 Introduction.

As sputter deposition is quite an energetic process, it is reasonable to question what effect sputter deposition can have on the surface of the Nafion membrane. As demonstrated in Chapter 3, there is a difference in conductivity of membrane electrode assemblies (MEAs) constructed with reactively sputtered gas diffusion electrodes and MEAs with platinum reactively sputtered onto the Nafion membrane. This suggests that there is an effect attributable to the actual sputtering process. This effect may possibly be local thermal effects arising from the impact of the ejected platinum, which interfere locally with the conductivity of the membrane.

There is therefore a need to sputter the platinum onto a surface other than the Nafion membrane. Whilst high roughness factor electrodes are available by reactive sputtering platinum oxide layers on carbon GDEs, direct application of the platinum catalyst onto the Nafion membrane is attractive. This is because intimate contact between the electrolyte and the catalyst layer improves the ionic conductance of protons from the catalyst surface into the bulk of the electrolyte, and improves utilisation of the catalyst by ensuring that no area of catalyst is out of ionic contact with the membrane. Compare this with deposition on the face of the gas diffusion electrode where the roughness of the GDE may mean some sputtered catalyst being at some distance from the membrane surface. Direct deposition of the platinum onto the surface of the platinum membrane ensures the catalyst layer forms on the template of the outside surface of the Nafion membrane, and remains as close as possible to the interface between the electronic conductor, the gaseous fuel and the electrolyte [16].

A method of transferring a thin, high roughness factor catalyst layer onto a sheet of Nafion was therefore sought. It was decided to use an alternative substrate, on which a layer of platinum would be sputter-deposited. The secondary substrate could then be bonded to the Nafion membrane. This substrate could then be removed by dissolution or chemical reaction, leaving the platinum catalyst layer on the surface of the Nafion membrane.

Figure 4.1: Illustration of indirect sputter coating process. Far left figure: secondary substrate shown in light grey, onto which is sputtered the Pt layer (black). The secondary substrate is then laminated to the Nafion membrane (dark grey, centre figure). The secondary substrate is dissolved and the membrane pressed to the backing layer (dappled, far right figure).

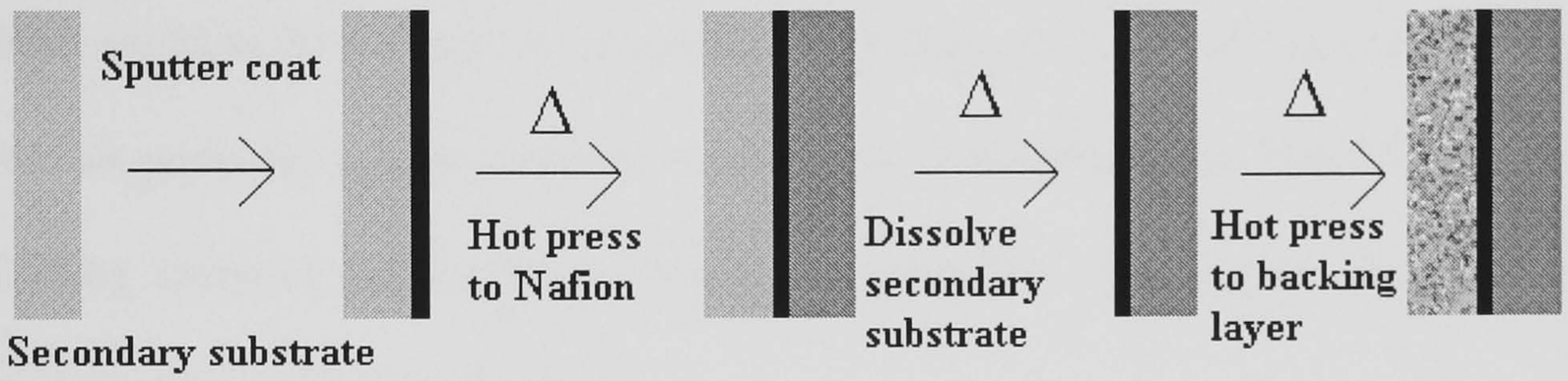

Aluminium foil provides an ideal surface for sputter deposition. It is inert in the sputtering environment, and does not liberate vapour or moisture in the vacuum that precedes sputter deposition. Following deposition and contact with the Nafion membrane, aluminium foil can be removed by dissolution in hydrochloric acid:

$$2Al\ (s) + 6HCl\ (aq,\ 0.1\ mol\ dm^{-3}) \rightarrow 2AlCl_3\ (aq) + 3H_2\ (g)$$

The aluminium chloride formed undergoes some degree of hydrolysis in acid solution. Aluminium also dissolves in hydroxide solution:

$$2Al\ (s) + 2NaOH\ (aq,\ 0.05\ mol\ dm^{-3}) + 6H_2O \rightarrow 2Na^{+}(aq) + 2[Al(OH)_4]^{-} + 3H_2(g)$$

The concentration of the dissolving solution is kept deliberately low as the evolution of the hydrogen gas formed in both cases interferes with the adhesion of the platinum metal to the Nafion membrane [65].

Another possible group of removable substrates, which circumvent the problem of gaseous reaction products from the dissolution process, are soluble polymers cast into sheets. With soluble polymer substrates, extremely gentle reaction environments for the removable process are accessible. Candidate polymers include polystyrene sulfonic acid (PSSA) and polyvinyl alcohol films (PVA); however PSSA films cast from solution do not have a sufficiently high glass transition temperature to withstand the hot pressing process required to bond the membrane to the Nafion. PVA films are finding commercial use for a variety of applications that require soluble polymers, such as disposable laundry bags.

Reactive sputter deposition on a soluble secondary substrate is considered to be a promising approach to the problem of depositing a thin layer of high surface area platinum on a Nafion membrane without the possible deleterious effects of direct sputter deposition on the surface.

4.2 Experimental.

A platinum target (Emitech, UK) was reactively sputtered in oxygen at plasma gas pressures of around 4×10^{-3} mbar to 10^{-2} mbar (0.4 – 1 Pa) for 960 s at a sputtering current of 75 mA, then with an additional coating of platinum sputtered in argon for 90 s at 100 mA (see chapter 2) in an Emitech K575X sputtering unit in a total of five sputtering cycles. The substrates were domestic aluminium foil and polyvinyl alcohol films (Aquafilm, UK). A thin layer of Nafion, typically around 2 mg cm^{-2}, was added to the sputtered surface of the aluminium substrates by dropping a 10 wt % Nafion

solution in water onto the surface which was heated on a hotplate. In order to deposit a thin layer of Nafion onto the PVA-Pt films, Nafion was dropped onto the surface from a 10 wt % solution in methanol in order to prevent premature dissolution of the PVA films. The methanol solvent was allowed to evaporate at room temperature. These films were then hot pressed to Nafion 117 membranes at 75 kg cm^{-2} (7.36 MPa) and 155°C for ten minutes. When pressing to the PVA films, Nafion membranes needed to be treated in 0.025 mol dm^{-3} NaOH at room temperature for 120 mins to convert the Nafion to the Na^+ form. This prevented a brown discolouration of the assembly during the hot pressing process when the acidified membranes were employed, possibly due to a reaction with the soluble polymer. When cooled, the pressed assembly was lowered into water at 80-90°C to dissolve the PVA membrane for 1-2 hrs. Aluminium films were dissolved in 0.05 mol dm^{-3} NaOH at room temperature. The electrochemically active surface areas were assessed by the same method employed for the directly sputtered membranes and electrodes (see chapter 2).

4.3 Results and Discussion.

4.3.1 Assessment of Roughness Factors of Films.

Indirectly sputtered platinum films were created by reactively sputter depositing platinum onto aluminium foil and polyvinyl alcohol films. These platinum layers were transferred onto Nafion membranes by depositing a thin layer of Nafion from solution onto the platinum surface, hot pressing to Nafion and dissolving the secondary substrate. It was found to be possible to deposit a platinum catalyst on the surface of the Nafion in this way. Figure 4.2 below shows a CO stripping cyclic voltammogram of a platinum-catalysed Nafion membrane, indirectly deposited via an

aluminium foil. The platinum voltammetry is well defined; the CO peak is highlighted.

Figure 4.2: CV of indirectly-sputtered platinum on Nafion working electrode in 0.5 mol dm^{-3} H_2SO_4, CO saturated for 20 mins then N_2 sparged for 40 mins whilst held at 0.4V versus RHE, then cycled at 25 mV s^{-1}. Potentials measured with saturated mercury/mercurous sulphate reference electrode corrected to reversible hydrogen scale.

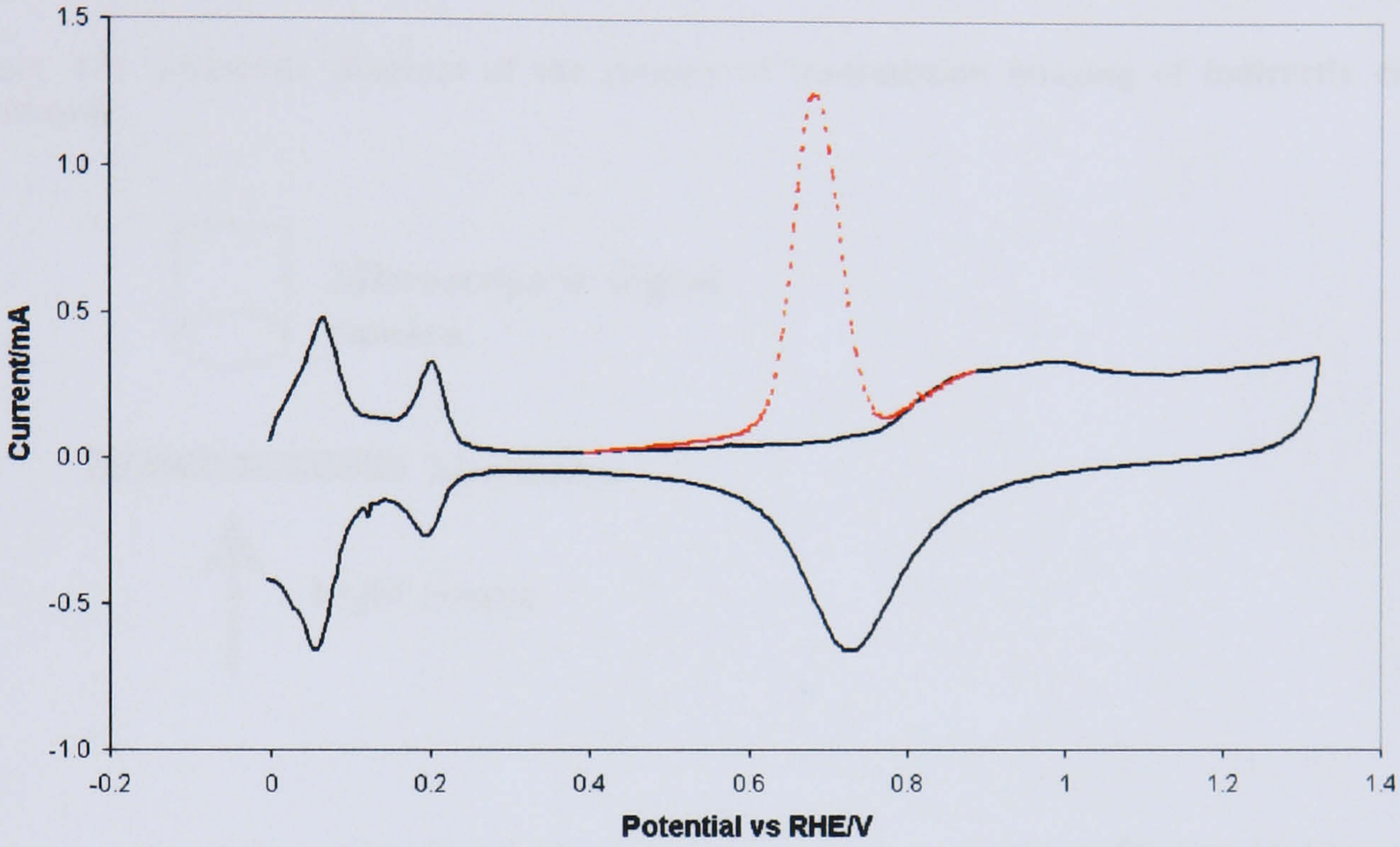

4.3.2 Cracking of Catalyst and Loss of Catalyst from Nafion Layer.

Platinum catalyst layers formed in this way are not complete, with cracks and not conductive across the entire membrane, and full adhesion of the catalyst layer is not achieved. There is some interference with the adhesion of the platinum layer from hydrogen evolution from the dissolution of aluminium. Another barrier to the formation of a coherent film is the swelling and contraction of the Nafion membrane and the solution-cast Nafion layer during the hot pressing and aluminium and PVA-dissolution process.

The roughness factors achieved with aluminium foil as a secondary substrate were significantly poorer than those achieved with direct reactive sputter deposition on the Nafion membrane. This was ascribed to incomplete transfer of the platinum films. In

order to assess the extent of transfer, images of the membrane were taken with a Edmund Scientific (Barrington, NJ) microscope with digital camera attachment with an optical zoom. A transmission geometry with the films illuminated from below was used in order to visualise discontinuities in the membrane- see figure 4.3.

Figure 4.3: Schematic diagram of the process of transmission imaging of indirectly coated membrane.

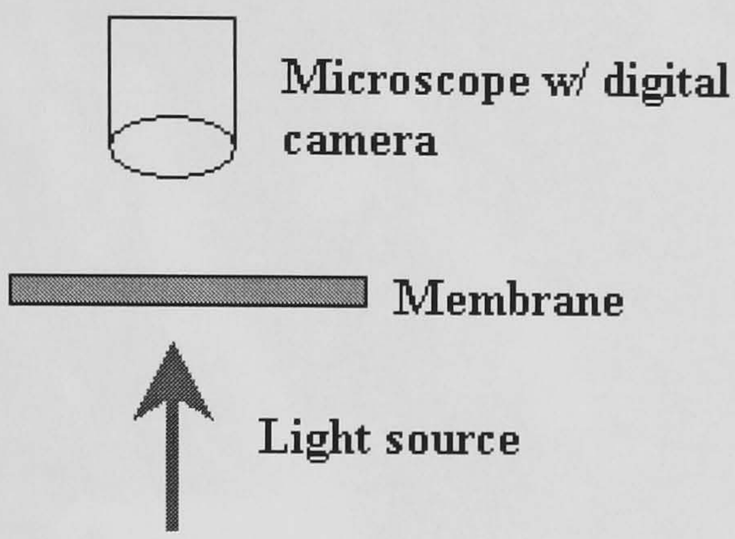

Images were analysed by Corel photo-paint image processing software. Images were taken at a calculated magnification of 208× (the nominal magnification on the microscope equipment was 250×). The resultant .jpg format images were converted to binary 1-bit black and white figures. All areas above 50% grayscale saturation (bit value 128/256) were converted to dark; all below 50% to light. A typical image of the indirectly-coated membrane is shown in figure 4.4. The many discontinuities present in the film can be clearly observed, from small scale crazing of the platinum layer to longer cracks running from top left frame to bottom right. These cracks are believed to follow patterns of striation on the Nafion from the extrusion process.

Figure 4.4: Typical transmission image of an indirectly sputtered membrane. Magnification ×68. Inset: the same image converted to binary black and white following the process described in the text. Magnification ×21.

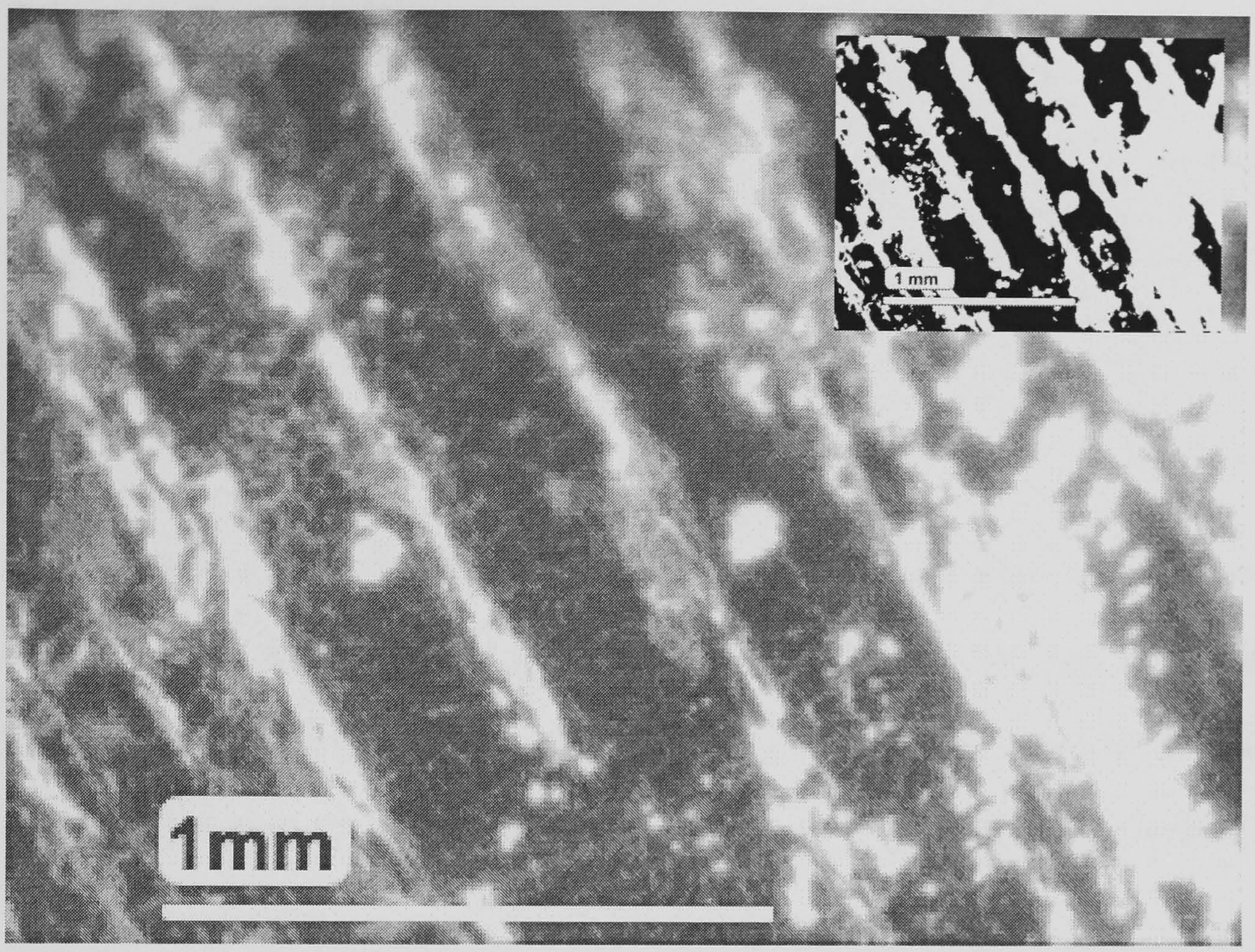

At the magnifications employed, the membrane area surveyed was considerably smaller than the total area of the membrane. Therefore, the extent of coverage for these membranes was estimated from the mean ratio of platinum taken from 5 images of various parts of the membranes. Two membranes with varying extents of platinum coverage as estimated by visual assessment were analysed by this technique. For comparison an image was taken of a directly reactive sputtered membrane. The coverage of platinum for the directly reactive sputtered membrane was estimated at 97.0% using images analysed by this method. Table 4.1 shows the comparison between roughness factors achieved and estimated extent of platinum coverage. The sputtering and transfer methods for the two membranes were identical, but the extent of membrane coverage by this method is highly variable as illustrated by the discrepancy between the two roughness factor values.

Table 4.1: Roughness factors and estimated extent of platinum coverage for two indirectly-coated membranes.

Membrane Number	Roughness Factor	Estimated platinum coverage (%)
1	1.2	38.8
2	0.3	4.4

It is possible to project estimated roughness factors for the deposited platinum by comparing the electrochemically active surface area with the area of deposited platinum as found by transmission image analysis. By this method, estimated roughness factors of 5.15 for membrane 1 and 6.81 for membrane 2 are calculated.

The shortcomings of the indirect deposition method are clear. The extent of platinum coverage is limited by poor adhesion of the transferred layer. However, it is clear from the relationship between calculated platinum coverage and roughness factor that the indirect deposition method does transfer a proportion of the sputtered platinum layer to the Nafion membrane. The resulting roughness factor may have been higher, had some of the platinum catalyst not been isolated in islands isolated from electronic conduction to the current collector.

4.4 Conclusion.

It has been shown that an indirect transfer method using sputter deposition on a secondary substrate can transfer a modest proportion of the high surface area platinum layers reported in chapter 2. However the transfer of the platinum layers is some way short of being complete. Furthermore the roughness factors of the resulting electrodes are significantly lower than the figures of 130-150 $cm^2\ cm^{-2}$ reported in

chapter 2, even if the experimentally determined ECSA is compared to the platinum coverage estimated from the transmission image analysis. The poor roughness factors are thought to be due to the limited transfer of the catalysts, but worsened by possible isolation from conduction of islands of deposited platinum. It is also possible that some loss of roughness may be due to some sintering of the platinum during the hot pressing process (see experimental) during the formation of the fused membrane before dissolution of the aluminium. The platinum particles which form the catalyst layer are unsupported and it is perhaps unsurprising that the full roughness factors shown for the directly deposited catalysts are not seen.

Further enhancement of the extent of coverage is required to develop coherent platinum catalyst layers. The technique shows limited promise as a route to the deposition of a catalyst layer in intimate contact with the Nafion membrane without the reduction in the proton conductance of the material.

Chapter 5: Investigations Into Tungsten Carbides As Possible Non-Noble Metal Fuel Cell Catalysts.

5.1 Introduction.

The use of platinum as a fuel cell electrocatalyst clearly imposes a cost constraint on the commercialisation of fuel cells. The bulk cost of platinum is high, so there is a strong incentive to reduce the loading of the catalyst on the electrodes and maximise the surface area of the available platinum. However, there are alternatives to platinum that catalyse the reactions that take place in a fuel cell. Other metallic catalysts have been considered, as have bimetallic catalysts and other alloys. Porphyrin structures have been investigated for cathodic oxygen reduction. For hydrogen oxidation catalysis, transition metal carbides and nitrides are attracting a large amount of research interest.

Transition metal carbides and nitrides have been investigated for fuel cell reactions because they have the potential to offer promising activity per unit cost, even if the specific activity is significantly lower. The carbide and nitride compounds that attract interest are isoelectronic with platinum group metals, and have some metallic character that confers electronic conductivity, a requirement for electrocatalytic applications.

Tungsten carbide is chosen for investigation in this work. Levy's [31] early study into this material found that the gas-phase reaction between hydrogen and oxygen on tungsten was accelerated by modifying the tungsten with carbon. Other early investigations showed electrocatalytic activity for the anodic oxidation of hydrogen. In addition, these catalysts are highly passive, in that they are resistant to corrosion in acids. They are also not significantly poisoned by carbon monoxide in the gaseous reactants [40]. The cost of the materials is of course significantly lower than that of

platinum. For these reasons, tungsten carbide materials were thought to warrant further investigation for anodic oxidation of hydrogen.

In this work, tungsten carbide catalysts will be synthesised by reducing and carburising tungsten oxide in a flowing mixture of hydrogen and methane. Tungsten metal is not directly carburised because it would be expected to undergo some sintering at the temperatures required [39], and because of difficulties in producing finely divided tungsten. The conversion of tungsten oxide to tungsten carbide involves a reduction step and a carburisation step; the mechanism was studied in detail in the work of Lofberg [66].

The catalyst will be tested in standard three-electrode electrochemical cells, gas-fed half cells with aqueous acid electrolyte and a full fuel cell test. It is anticipated that the catalyst may have different behaviour in a solid polymer electrolyte than in an acidic electrolyte. The effect of a proportion of carbon monoxide in the reactant gas stream will also be investigated. A detailed examination of the catalytic activity of the tungsten carbide materials synthesised in this work would not be complete without an attempt to evaluate the kinetics of hydrogen oxidation on these materials. All such assessments require a measurement of the diffusion limited current. Once a sufficiently high overpotential is applied, all of the hydrogen reaching the surface of the electrode will be effectively instantaneously electrochemically oxidised. Provided mass transport of the hydrogen to the electrode is time independent then the current should remain constant with time and be proportional to the rate of hydrogen mass transport. Thus, above a certain overpotential, the current seen is invariant with potential, and is said to be diffusion limited as the barrier to greater reaction is not the kinetic limitation of electron transfer but the rate of supply of reactant. For a fuel cell

electrode, a diffusion limited current is typically observed when the fuel cell is running at low cell voltage and higher currents. As discussed in chapter 1, (introduction), the fuel cell is typically thought to be operating under kinetic limitation at larger cell potentials where the overpotentials at each electrode are small. At intermediate cell potentials the current drop is largely associated with the ohmic resistance of the cell. At still lower cell potentials, the overpotential at each electrode is highest and the cell current becomes limited by the transport of reactants. The maximum cell current is obtained when the cell is operating at short-circuit conditions with a cell potential of 0V. Each electrode is operating at maximum overpotential, so the electron transfer kinetics are as rapid as possible.

It is important to recognize that the diffusion limited current is directly related to the mass transport coefficient of any system by the expression:

$$j_d = mnFc_0$$

Where j_d is the transport limited current density, m is the mass transport coefficient (units m s^{-1}), n is the number of electrons transferred and c_0 the reactant bulk solution concentration. However, the mathematical determination of the mass transport coefficient for a fuel cell is not straightforward as it is dependent on the operating conditions and fuel cell geometry in a complicated way.

It is somewhat easier to calculate diffusion limiting currents when using the rotating disk technique as there is a straightforward mathematical relationship between the various parameters in the system (disk rotation rate, solution viscosity etc.) with the mass transport coefficient due to the simplified and symmetrical geometry of the system. In such experiments diffusion limited currents are assessed by performing steady-state voltammetry on electrodes with well-understood hydrodynamics. In the

rotating disk electrode (RDE) technique the rotation of the disk propels solution close to the surface outwards. Fresh solution is then drawn inwards, normal to the surface of the disk. The system gives a diffuse double layer of well-defined thickness. Increasing the rotation rate increases the rate at which solution is refreshed at the interface, increasing the current. For such a system, the mass transport coefficient is proportional to the square root of the rotation rate. The mass transport coefficient is given by:

$$m_{rde} = 0.62 D^{\frac{2}{3}} v^{\frac{-1}{6}} \omega^{\frac{1}{2}}$$

Under diffusion controlled conditions the transport limited current density, j_d, at the electrode is:

$$j_d = 0.62 nFD^{\frac{2}{3}} v^{\frac{-1}{6}} c_0 \omega^{\frac{1}{2}}$$

Where D is the reactant diffusion coefficient, c_0 the reactant bulk solution concentration, v the viscosity of the electrolyte and ω the rotation rate of the electrode. This latter relation is known as the Levich equation.

For a reaction such as the hydrogen oxidation, which is first order with respect to hydrogen partial pressure, the kinetic current density can be calculated [67]:

$$\frac{1}{j} = \frac{1}{j_d} + \frac{1}{j_k}$$

Where j is the measured current density, j_d is the diffusion limited current density and j_k is the kinetic current density. A plot of 1/j versus $1/(\omega^{1/2})$ should give a straight line with a value at $1/(\omega^{1/2})=0$ which gives $1/j_k$.

Other papers in the chemical literature have focussed on the carburisation of well-dispersed tungsten oxide particles, such as precipitates from acid treatment of ammonium tungstate.

An alternative route to small particle tungsten oxide for carburisation is explored in this work. The Pechini method was patented in 1967 [68], and is named for its inventor, M. U. Pechini. It is also known as the polymer precursor method, and can be used to form well-dispersed Perovskite structures such as oxides of transition metals. The method produces homogenous compositions of the metals used, and leads to small crystallites. It is experimentally simple to perform, and requires only low temperatures, so is appealing as a low-cost approach to various metal oxide structures. The method is based on the dissolution of the metal required in a solution containing ethylene glycol; citric acid is added to yield polymerised metal citrates. The water is boiled off and the resulting solid resin baked at 155°C, which decomposes the citrate polymer, leaving an extremely porous metal oxide structure.

The Pechini method, and variations on it, is extensively used to produce Perovskite structure oxides where transition metal ions can be substituted into a lanthanide oxide lattice. Materials of this kind find wide use in catalysis and electronics [69]. Fuentes et al [70] synthesised molybdenum and tungsten containing peroxides by the polymer precursor method. They are also finding some applications in fuel cell electrocatalysis. Stojanović et al [71] reported the syntheses of various $LaCr_{1-x}Ni_xO_3$ (0-x-1) by the Pechini method for possible use as anode catalysts for solid oxide fuel cells. Laberty-Roubert et al [72] used the Pechini method as a route to the yttria-stabilised zirconia electrolyte used in SOFCs. Wijayasinghe et al [73] investigated the Pechini method synthesis of $LiFeO_2$-NiO solid solutions for cathode materials for molten carbonate fuel cells.

5.2 Experimental.

5.2.1 Production of Tungsten Carbide.

Tungsten oxide nanopowder (Aldrich, 25.3 $m^2 g^{-1}$, 33 nm particle diameter) was placed in a ceramic crucible, which was placed in a quartz tube in a tube furnace. The material was heated under a flowing 1:3 [25vol% H_2 in CH_4] mixture of hydrogen and methane (BOC) under slight positive pressure through the use of a bubbler. The reactant material was typically heated at 1°C per minute to 800°C and maintained at that temperature for around 1h. The reactor was then cooled, and the product tungsten carbide was annealed by various processes outlined below. Tungsten oxide was also synthesised by a Pechini-type method. Tungsten metal (Aldrich) was dissolved in 27 wt% hydrogen peroxide (Aldrich). Citric acid was added in a 3:1 molar ratio. The hydrogen peroxide was decomposed by holding a platinum flag under the surface for several minutes. Ethylene glycol (BDH) was stirred into the solution in a 1:1 ratio with the citric acid. The solution was boiled to drive off the majority of the water, then heated to 150°C in an oven, yielding a porous resin. The resin was heated to 400°C in a furnace to ensure complete drying. The result was a highly porous green tungsten oxide powder. This powder was then carburised in the same way as the Aldrich tungsten oxide nanopowder.

The tungsten carbide materials were subjected to Brunauer, Emmett and Teller nitrogen adsorption surface area analysis (BET analysis). BET measurements were performed using a Micrometrics ASAP 2010 BET analyser under liquid N_2 conditions from 77.3 K. The catalysts were also characterised by X-ray powder diffraction. Samples were analysed by a Phillips X-ray diffractometer by an incident

CuKα X-ray beam of wavelength 1.541 Å with a Ni filter. The samples were scanned from 10°<2θ<90° and compared to existing powder patterns to assign peaks [74-77].

5.2.2 Rotating Disk Experiments.

Electrodes used to assess the diffusion limited current for hydrogen oxidation on tungsten carbide in aqueous acidic electrolyte were prepared as follows. An ink with tungsten carbide catalyst A (made from carburising tungsten oxide nanopowder (Aldrich) and a Nafion binder was prepared by ultrasonic agitation. The catalyst was added by evaporating a drop on the surface of a glassy carbon disk electrode sheathed in PTFE. The catalytic loading was 2 mg cm^{-2}, bound with 25 wt% Nafion. The glassy carbon RDE was mounted in a rotator and controlled by a MSRX speed controller (Pine Instruments, Grove, PA). It was immersed in 0.5 mol dm^{-3} H_2SO_4, in a standard electrochemical cell as shown in chapter 2, experimental section. The reference electrode was a mercury/mercurous sulfate electrode (MMSE) and potentials were corrected to the RHE scale. The counter electrode was a coil of platinum wire. The electrolyte was bubbled with argon or hydrogen (both Air Products, BIP grade) for 1 hr preceding each experiment to ensure saturation, and continuously throughout. The potential of the rotating disk electrode was scanned from 0V to 0.5V at 5 mV s^{-1} vs RHE with the electrode stationary and rotated at various rates between 900 rpm and 6400 rpm.

5.2.3 Manufacture of Electrodes.

3-5 millilitres of water sufficient to suspend the catalysts (Milli-Q, Millipore) were added to the resulting tungsten carbide materials. In order to ensure complete dispersion, the suspensions were sonicated in an ultrasound bath (Ultrasonics UK) to give a homogenous ink. A PTFE emulsion, Fluon GP-1 (Asahi Glass Ltd.) was added

to the ink to give a binder, which, on evaporation, would yield a tungsten carbide layer with 25 wt% PTFE binder. The ink was added dropwise to the surface of a carbon paper disc (Toray). The PTFE content of the as-received carbon paper was 6 wt%. This was found to be too low a PTFE content to provide the wet-proofing necessary for half cell reactions, where the carbon paper and catalyst is mounted between a gaseous reactant chamber and a liquid electrolyte. The PTFE content of the carbon paper was therefore increased. GP-1 emulsion, with a few microlitres of THF added to allow the emulsion to wet the carbon paper, was added dropwise to the surface of the carbon paper; the solvents were evaporated in a drying oven and the PTFE was sintered at 356°C. Following the addition of the catalyst ink to the surface of the carbon paper, the water was evaporated in a drying oven at 80°C. The catalyst layer was sintered at 356°C to bind and wetproof the tungsten carbide layer.

5.2.4 Testing of electrodes.

For half-cell testing, the catalysed carbon paper was mounted at the opening of a cylindrical gas chamber in a PTFE/glass construction half-cell, with the catalyst facing the liquid electrolyte side. Electrical connection to the working electrode was made by a platinum ring mounted in contact with the carbon paper backing, on the gas admission side.

A mercury/mercurous sulfate reference electrode (MMSE) was mounted in a compartment of the half-cell apparatus equipped with a Luggin capillary; a coiled platinum wire counter electrode was also mounted in the cell. Gaseous reactants (Hydrogen, BOC, research grade and Argon, BOC, research grade) were fed to the electrode by sealing the gas compartment with a septum then injecting the gas via a needle at a slight positive pressure achieved by using a bubbler on the outlet line.

Voltammetry and chronoamperometry was recorded on an Autolab potentiostat by GPES software.

5.3 Results and Discussions.

Tungsten carbide catalysts were manufactured by three separate approaches. The different processes used in their synthesis are outlined in table 4.1.1.

Table 5.1: Tungsten carbide catalyst preparation methods.

Catalyst	Carburisation (in 25%H_2: 75%CH_4)	Tungsten Oxide Starting Material	Passivation
$WC_{(A)}$	Heated to 800°C at 2°C/min	Nanopowder (Aldrich)	Heated in research grade N_2 to 600°C
$WC_{(B)}$	As above	Nanopowder (Aldrich)	Heated in 10% O_2 in Ar to 600°C.
$WC_{(C)}$	As above	Pechini method tungsten oxide	Heated in research grade N_2 to 600°C

Tungsten carbide materials made by reducing and carburising tungsten oxide at elevated temperatures are annealed to prevent rapid re-oxidation on exposure to air [78]. The process passivates any reactive sites on the surface. The composition, surface structure and catalytic activity of tungsten carbide catalysts are known to be highly sensitive to the reaction conditions and composition of the carburising-reducing gas mixture [39]. Catalysts A, B and C differed in the passivation gas mixture used; B was passivated with 10% oxygen in argon, whilst A and C were passivated by heating to 600°C in research grade nitrogen (<0.02% O_2).

Figure 5.1 below shows the voltammetric sweeps for the tungsten carbide catalyst on the glassy carbon rotating disk electrode in aqueous 0.5 mol dm^{-3} H_2SO_4 electrolyte. The activity of the catalyst can be confirmed from the larger current at 0.4V vs RHE when the electrolyte is bubbled with hydrogen compared with argon.

Figure 5.1: 2 mg cm^{-2} WC(A) on RDE, 900rpm, in 0.5M H_2SO_4, sweep rate 5mVs^{-1}, sparged with reactant gases, room temperature (20±5)°C.

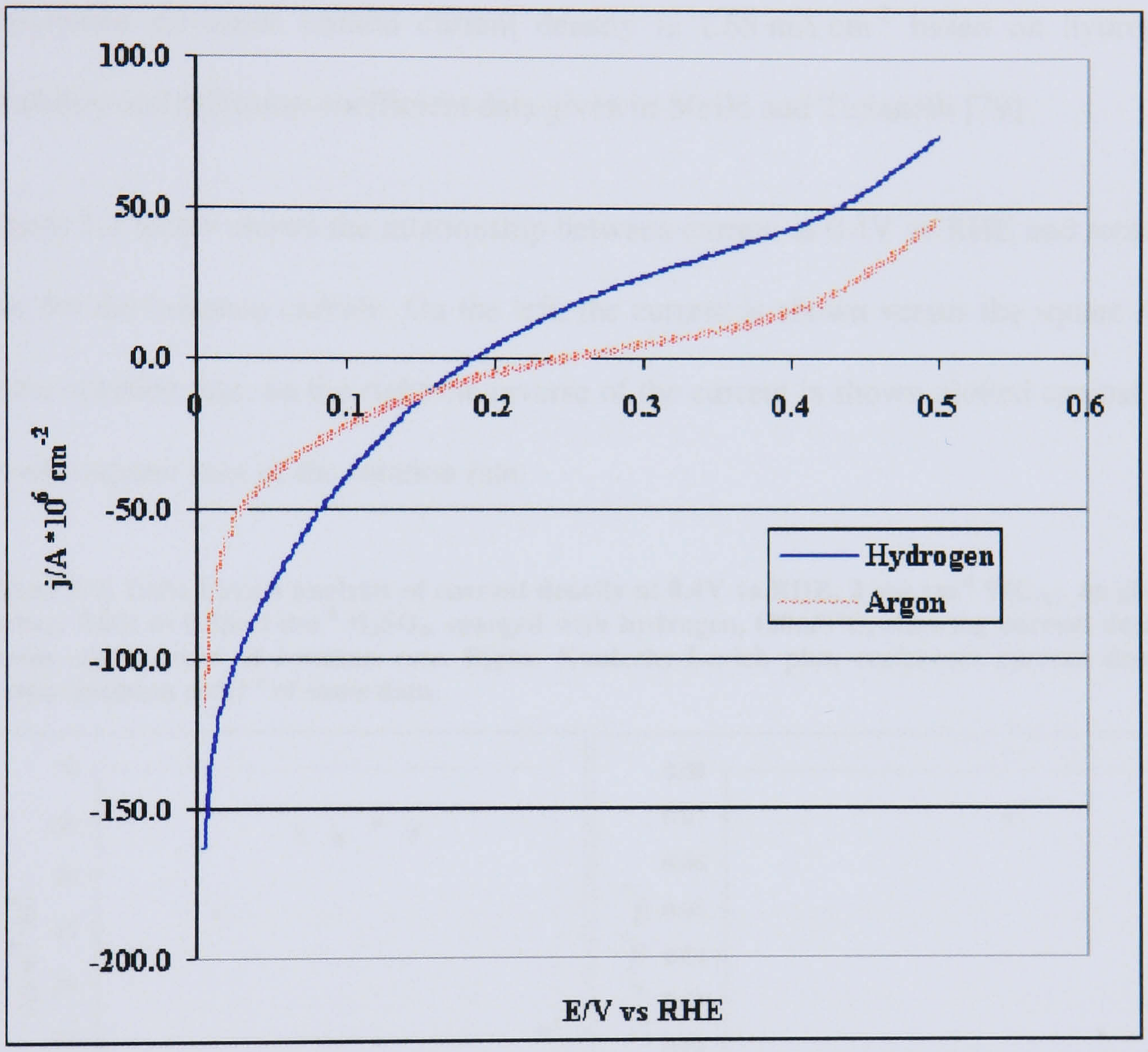

There appear to be complications arising due to background currents, possibly due to corrosion of the catalyst, around the thermodynamic potential for hydrogen oxidation. It is therefore not possible to construct a Tafel plot, as this would require an assessment of current density within a narrow potential range of the thermodynamic potential to extract j_0. It should be noticed, however, that the form of the

voltammetric waves do not resemble conventional steady state waves seen in rotating disk electrode experiments. Typically when a dissolved species undergoes an electrochemical reaction with rapid electron transfer kinetics on the electrode in question, the current rapidly approaches a plateau as the overpotential for the reaction, η, increases. In this case, this behaviour is not clearly identifiable. The anticipated diffusion limited current density is 1.68 mA cm^{-2} based on hydrogen solubility and diffusion coefficient data given in Mello and Ticianelli [79].

Figure 5.2 below shows the relationship between current at 0.4V vs RHE and rotation rate for the tungsten carbide. On the left, the current is shown versus the square root of the rotation rate; on the right the inverse of the current is shown plotted against the inverse square root of the rotation rate.

Figure 5.2: Left: Levich analysis of current density at 0.4V vs RHE, 2 mg cm^{-2} $WC_{(A)}$ on glassy carbon RDE in 0.5mol dm^{-3} H_2SO_4, sparged with hydrogen, (20±5)°C, showing current density versus square root of rotation rate. Right: Koutechy-Levich plot, reciprocal current density versus (rotation rate)$^{-½}$ of same data.

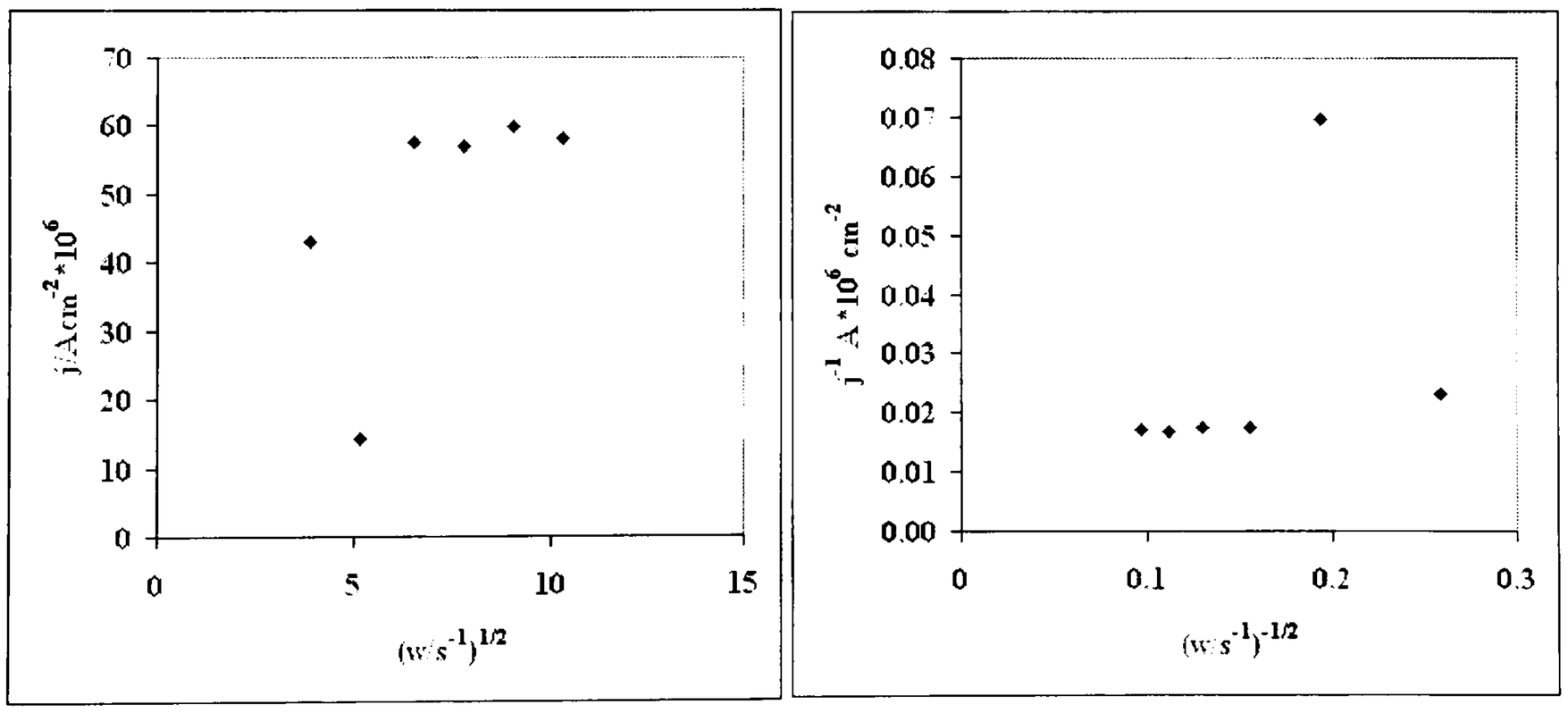

Significantly, there is no linear correlation between the current and square root of rotation rate, or between the inverse of current and the inverse square root of rotation rate.

It has therefore not been possible to calculate a diffusion limited current for hydrogen oxidation in acidic electrolyte on tungsten carbide. This represents a failure to fill in a comprehensive assessment of the electrocatalytic properties of tungsten carbide material. There is a small enhancement in the current at 0.4V vs RHE when in the presence of hydrogen in the aqueous acidic electrolyte, a result expected from the noticeable hydrogen oxidation current in the electrochemical half-cell referred to in section 5.2. There is no diffusion limited current seen under these circumstances. It is possible that under the conditions which the tungsten carbide was tested, a transport limited current will not be seen because the current at 0.4V vs RHE will never be high enough to be dominated by the transport of reactants to the catalyst. The loading of catalyst on a glassy carbon rotating disk electrode was kept to a minimum in order to prevent disruption to the well-defined diffusion layer at the face of the rotating disk electrode; there is also a problem with the adhesion of the catalyst layer to the disk surface. The catalyst loading on the carbon paper working electrode in the half cell was much higher, at 25 mg cm^{-2}. In the half cell, the reactants were supplied in gaseous form to the non-immersed side of the working electrode, and a pressure gradient forms when hydrogen is consumed at the electrode, refreshing the supply of hydrogen. In the RDE experiments, the concentration of reactant hydrogen is limited by its solubility in aqueous acidic electrolyte. It may be that the anions present are non-specifically adsorbing in a manner that inhibits catalytic activity.

However, the kinetics of the hydrogen oxidation reaction on tungsten carbide are clearly not fast enough under these conditions to bring about a diffusion limited current. The curves of the anodic currents shown in figure 5.1 suggest a fairly significant overpotential for hydrogen oxidation on the tungsten carbide, particularly when compared with the very rapid electron transfer kinetics seen for this particular

reaction on platinum. Although the overpotential effect is not sufficient to prevent the oxidation at the potentials seen in the RDE experiment, the kinetics of electron transfer on these catalysts under these conditions do not seem to be sufficiently rapid to produce a steady state current.

The catalytic activity for this reaction on these catalysts is too sluggish therefore to make an assessment by either the Levich or Koutechy-Levich analysis. There have been very few attempts to observe the transport limited property of the wide range of tungsten carbide based catalysts. Earlier studies on the catalytic activities of tungsten carbide materials focussed on the gas-phase heterogeneous catalytic activity for various reactions [31, 80]. The majority of previous studies on these catalysts have concentrated on the performance of the catalysts in half cell environments, such as in aqueous electrolytes with a fuel gas access chamber [40, 81, 82]. There have also been early full fuel cell tests with tungsten carbide materials [83]. However, it seems that the chemical literature of tungsten carbide electrocatalysis does not contain a thorough attempt to observe transport limited current on these catalysts.

A cyclic voltammogram of a 25 mg cm^{-3} electrode of catalyst A in room temperature (20±5°C) 0.5 mol dm^{-3} H_2SO_4, fed with gaseous hydrogen, was recorded. The reference electrode was a mercury/mercurous sulfate electrode, though the voltammogram is shown corrected to the reversible hydrogen electrode scale. The CV is shown in figure 5.3.

Figure 5.3: Cyclic voltammogram of Tungsten Carbide Catalyst A in half-cell fed by H_2, electrolyte- room temperature 0.5 mol dm^{-3} H_2SO_4. Scan rate 5 mV s^{-1}, vs MMSE, corrected to reversible hydrogen scale, (20±5)°C.

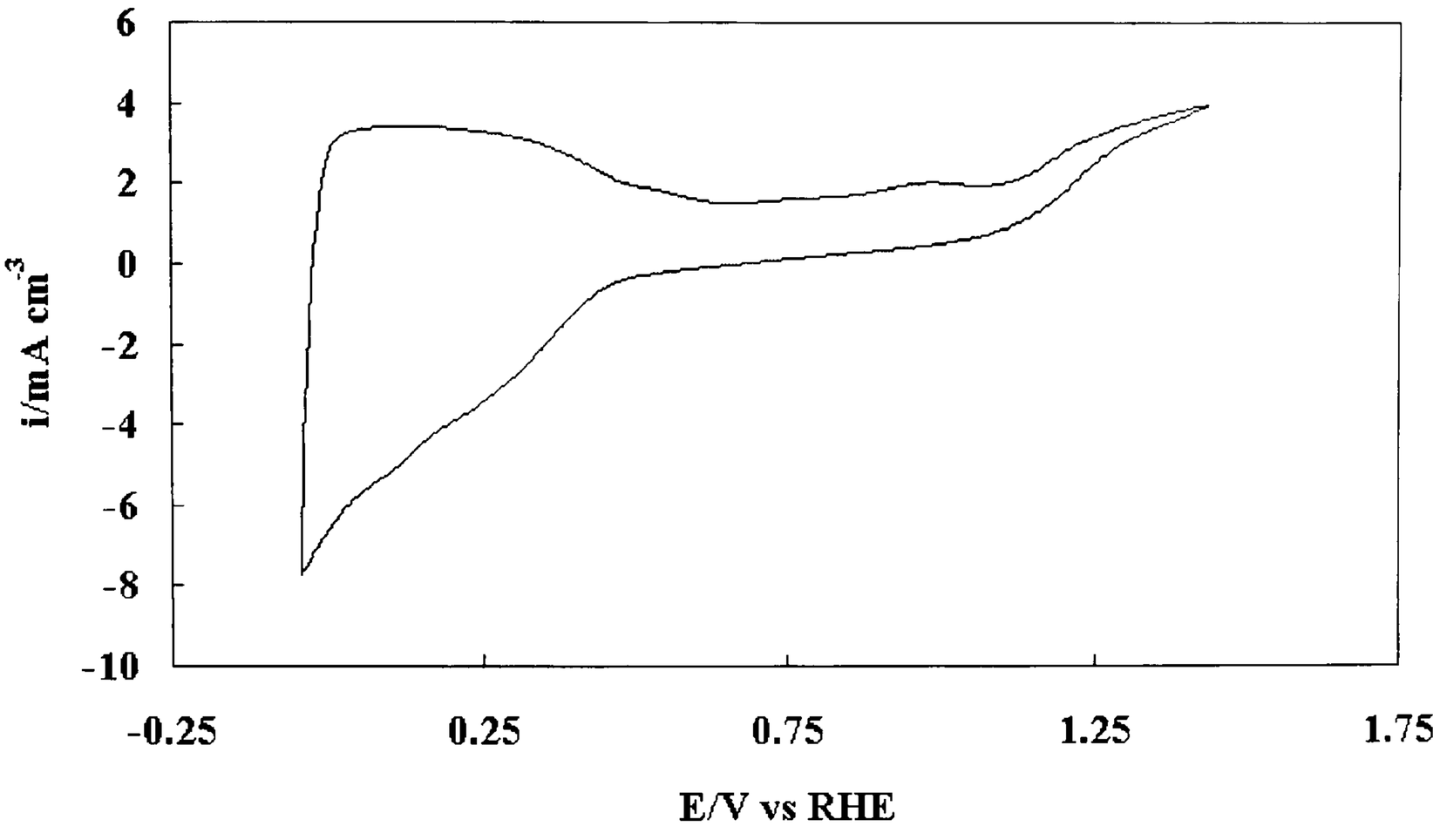

The voltammogram confirms the suitability of tungsten carbide as a hydrogen electrocatalyst. The onset potential of hydrogen anodic oxidation confirms there is no prohibitive overpotential on this catalyst. There appears to be a broad region of oxidation, suggesting a range of potentials over which hydrogen is adsorbed and oxidatively desorbed, probably due to a number of different adsorption sites.

The performance of the catalyst in a half cell was assessed by testing a 25 mg cm^{-2} tungsten carbide working electrode in room temperature (20±5°C) 0.5 mol dm^{-3} H_2SO_4 at various potentials and recording the current density as it approached steady state after 600 s. In order to assess the contribution to the current of anodic corrosion, inert argon was admitted to the gaseous reactant chamber and the current measured over a range of potentials from 0-0.6V. The argon was replaced with hydrogen and the experiment was repeated. Electrocatalytic activity may be impeded by the presence of a co-ordinating counter ion in the electrolyte. The bisulfate anion is known to non-specifically adsorb to some catalyst surfaces, whereas the perchlorate

anion- the counter ion in perchloric acid- is non-adsorbing. In order to assess this effect on tungsten carbide surfaces, the experiment was repeated with room temperature (20±5°C) 0.5 mol dm^{-3} $HClO_4$. Typical PEM fuel cells operate at 70-90°C, so the steady state currents at various potentials were also taken with the same electrolyte held at 75(±2)°C. The resulting half-cell polarisation curves are shown in figure 5.4.

Figure 5.4: Anodic hydrogen oxidation current density on various tungsten carbide catalyst fed with gaseous reactants under the conditions shown. Currents are steady-state, taken after 600s to give stationary current at potentials shown, without iR correction. The working electrode was a circular with 1 cm diameter. The reference electrode was held in the solution at the temperature shown.

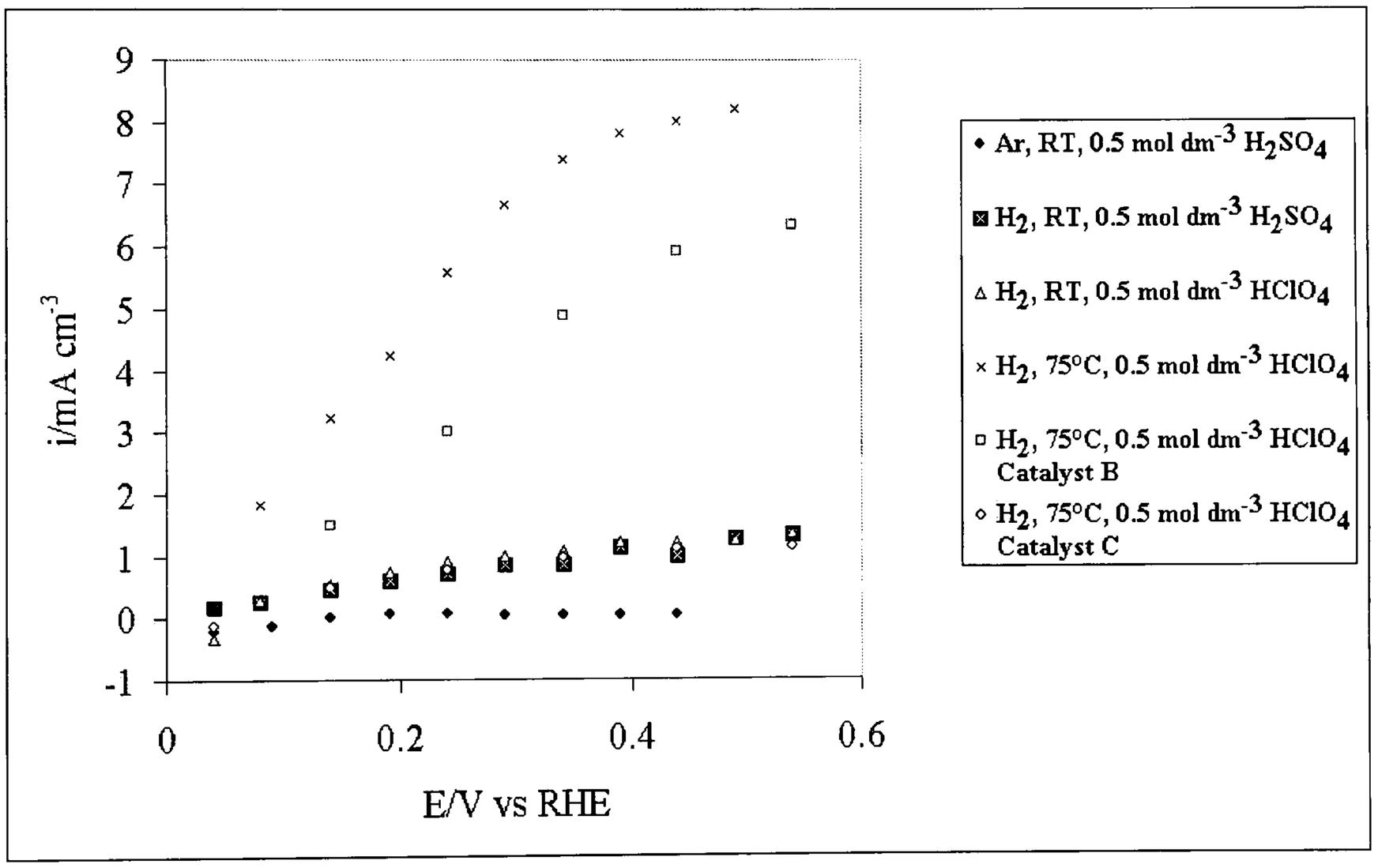

The curves show activity for the hydrogen reduction reaction over and above the background current, attributed to catalyst corrosion, seen when the half cell is supplied with argon. Significantly, the currents seen begin to plateau with increasing overpotential above 0.4 V, which may be due to the currents approaching transport limited conditions in the half cell.

Clearly there is a modest electrocatalytic performance for the anodic oxidation of hydrogen on tungsten carbide. There is a small current density associated with the corrosion processes or other electrode processes on the catalyst seen when argon gas is supplied to the electrode. However there is a noticeable anodic current several orders of magnitude higher when hydrogen gas is supplied. There is also a small but noticeable effect associated with changing the electrolyte from sulfuric acid to perchloric acid. There may be a limited inhibition of the catalytic activity of tungsten carbide by non-specific adsorption of the bisulfate anion. On raising the temperature of the electrolyte, there is a significant increase in the current density. There is clearly a strong temperature effect of the hydrogen oxidation reaction; the current density increases by an order of magnitude with an electrolyte temperature rise of 50-60°C.

Figure 5.5 shows a comparison between the half-cell polarisation curves obtained for catalyst WC_A and WC_B, both at 25 mg cm^{-2} loading.

Figure 5.5: Anodic hydrogen oxidation current on tungsten carbide catalysts. Currents are steady-state, taken after 600s to give stationary current at potentials shown, without iR correction. The working electrode was a circular with 1 cm diameter. The reference electrode was held in the solution at the temperature shown, 75°C 0.5 mol dm^{-3} perchloric acid.

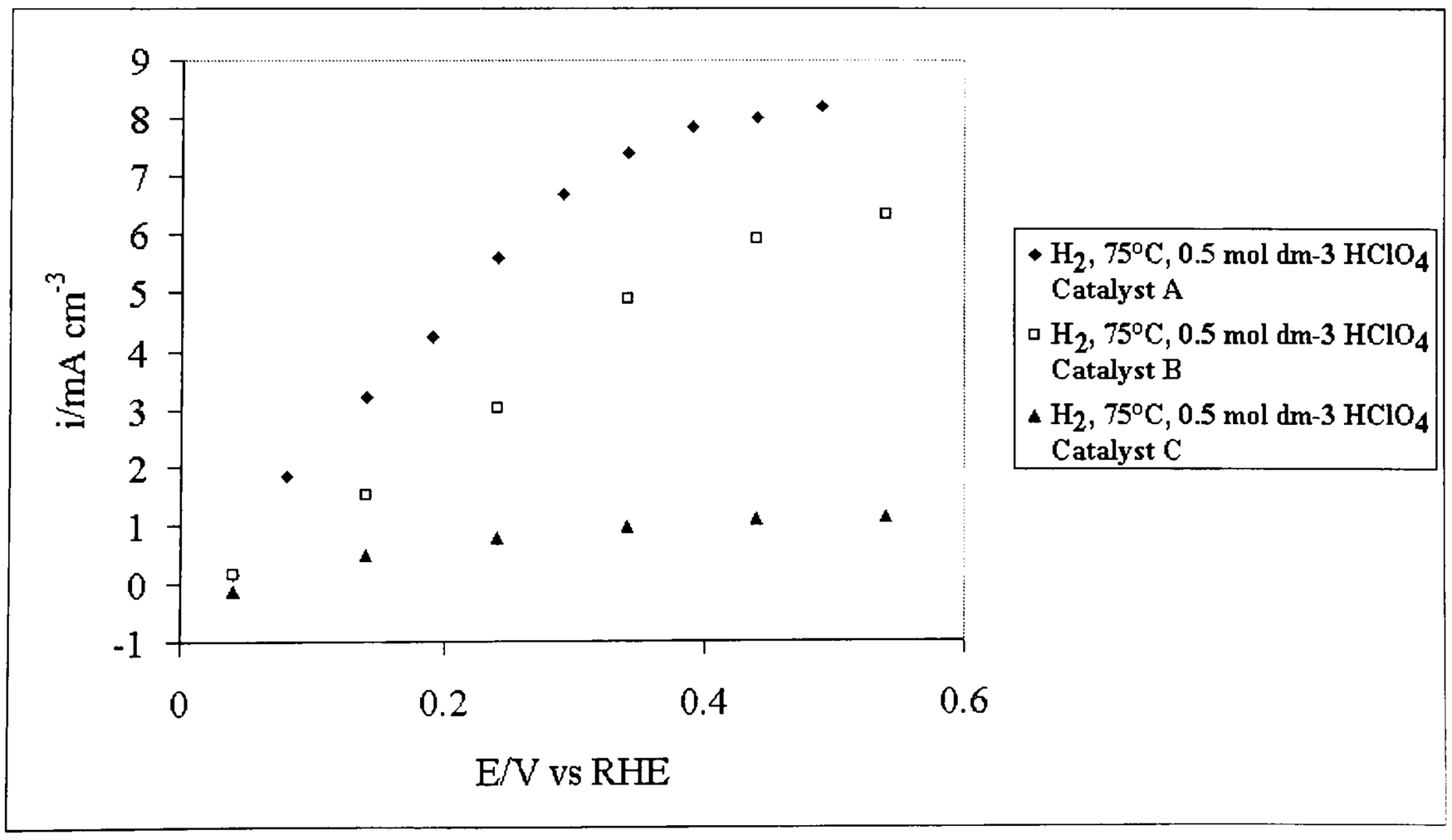

Again, the currents approach a plateau around 0.4 V which may due to transport limitation of reactants. It is not straightforward to assess the theoretical transport limited current as the catalyst is being supplied by gaseous reactants and transport conditions are not well defined. The form of the curves does suggest that, as the overpotential increases to the extent that the electron transfer kinetics are at the fastest rate available, the current begins to be limited by the supply of reactants.

Clearly there is a significant enhancement in the current density observed for catalyst A compared with B. This is ascribed to differing surface compositions of the catalyst brought about by the methods used to passivate the catalyst particles. The increased oxygen content of the passivating gas mixture used in the case of catalyst B appears to have brought about reduced catalytic activity, possibly through limited re-oxidation of the catalyst surface, either to tungsten oxide or tungsten metal. The carbide content at the surface of the catalyst particles may have been depleted by the passivation process. Catalyst A was annealed in the extremely low oxygen content of the impurity oxygen in research-grade nitrogen, and yields noticeably higher current density.

The third batch of catalyst was manufactured by the Pechini (polymer precursor) method. A gas diffusion electrode was manufactured in an identical manner to those catalysed by tungsten carbide synthesised from tungsten oxide nanopowder. This electrode was then mounted in the same PTFE/glass half-cell, which was immersed in 0.5 mol dm^{-3} perchloric acid. The current density was again recorded at various potentials between 0V and 0.6V. The resulting half-cell polarisation plot is shown in figure 5.4 (above).

The polymer precursor method has been shown to produce a tungsten oxide starting material suited to producing an electrochemically active tungsten carbide catalyst. However, the performance of the Pechini-method derived tungsten carbide is modest, and somewhat lower than the tungsten carbide manufactured from commercially available tungsten oxide nanopowder. The surface areas of catalyst A and catalyst C (produced by the polymer precursor method) were measured by the BET analysis. The surface areas were $5.91 \times 10^4\ cm^2\ g^{-1}$ for carbides derived from tungsten nanopowder and $2.52 \times 10^4\ cm^2\ g^{-1}$ for the catalyst prepared from Pechini method tungsten oxide. The surface areas found for the catalyst synthesised from tungsten oxide nanopowder was somewhat lower than the surface area given for the starting material. The BET surface areas recorded for catalyst C, made by the polymer precursor method, are slightly less than half those obtained for catalyst A. The surface area of the resulting catalyst particles is known to be dependent on the method of synthesis [39]. The reduction in catalyst surface area may be ascribed to sintering of metallic phases during the reduction step of the reaction. The surface areas reported are in the lower range reported by the work of McIntyre et al [40] and compare favourably with the commercially available tungsten carbide samples investigated by Bodoardo et al [84].

Figure 5.6 below shows the X-ray powder diffraction spectrum for a tungsten carbide catalyst produced by carburising tungsten oxide nanopowder.

Figure 5.6: X-ray powder diffraction pattern for tungsten carbide produced by carburising nanopowder.

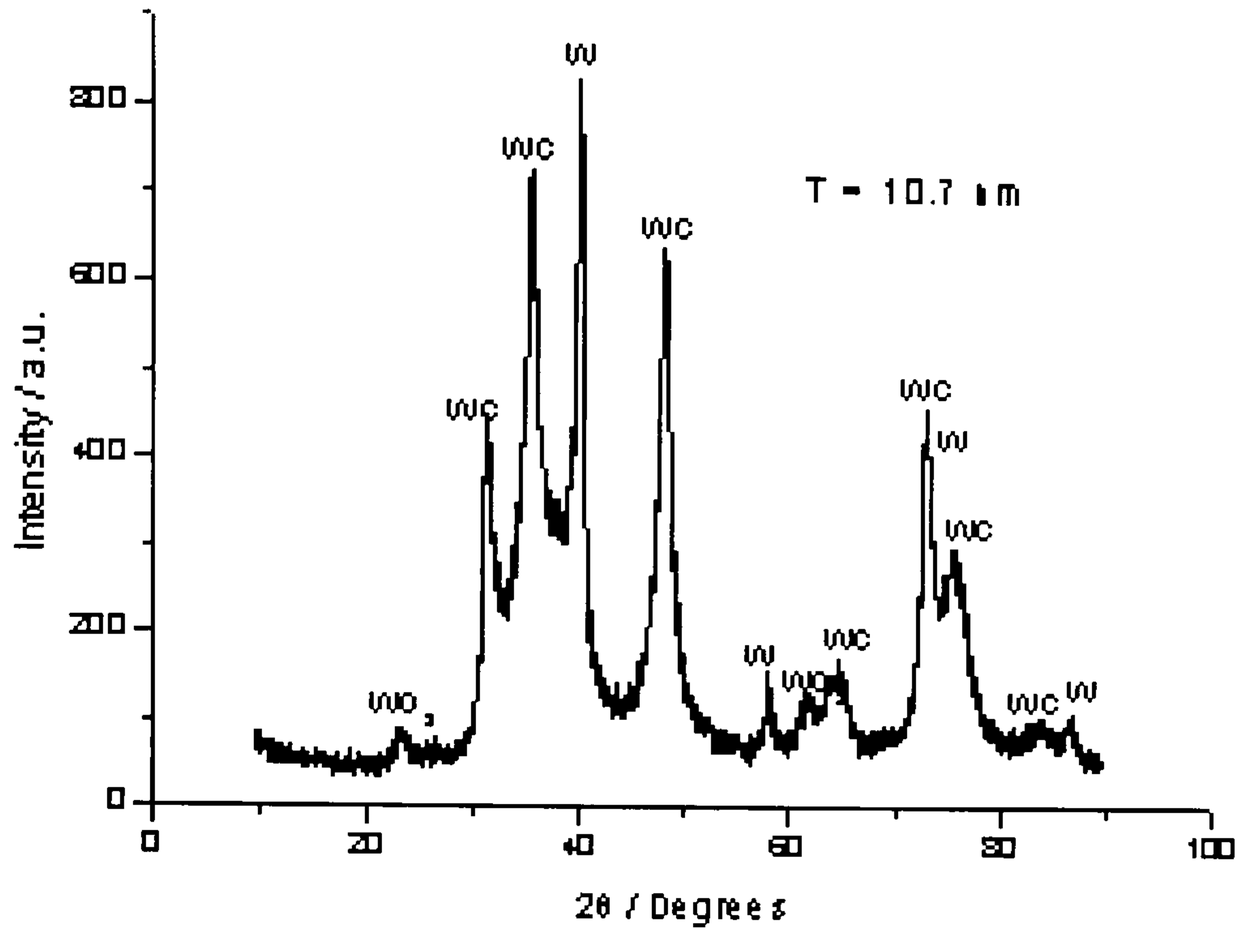

Peak assignments are based on JPCDS library data. The particulate size was assessed using the Debye-Scherrer equation.

$$T = \frac{C\lambda}{B\cos\theta}$$

Where T is the crystallite diameter, λ is the X-ray wavelength and C is a correction factor depending on crystallite shape. B is the full width at half maximum of the peak. Based on JCPDS data the value of C was fixed at 0.9. The value of T=10.7 nm is based on the peak at 2θ=48°. The XRD pattern shows a sizeable peak attributed to metallic tungsten, and some small peaks confirming the presence of unreacted tungsten oxide. The material is substantially WC tungsten carbide with a small crystallite size.

Figure 5.7 below shows the X-ray powder diffraction spectrum for a tungsten carbide catalyst produced by the polymer precursor method.

Figure 5.7: X-ray powder diffraction pattern for tungsten carbide catalyst produced by polymer precursor method.

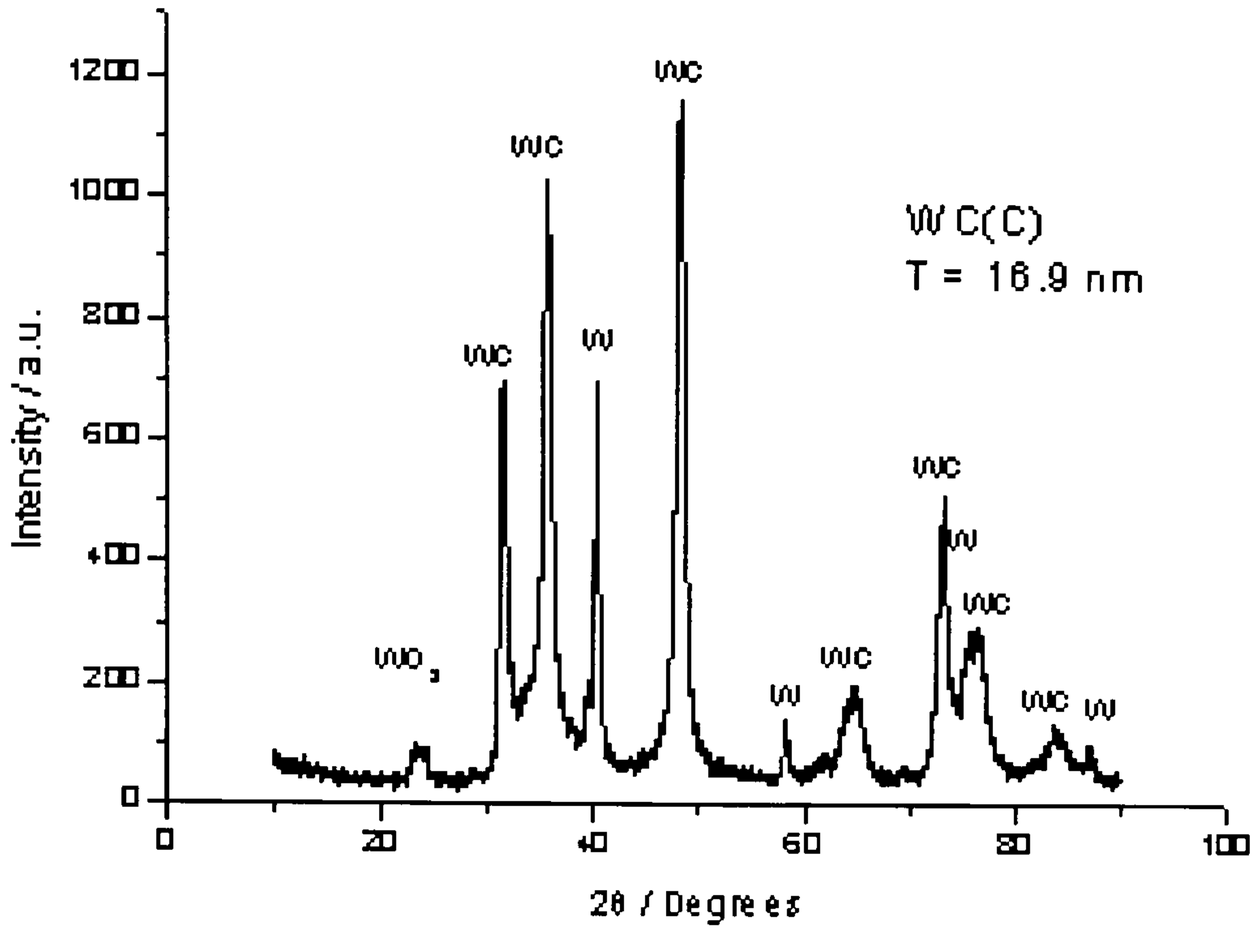

Again, there is a minor phase of metallic tungsten and a small trace of tungsten oxide.

The particle size calculated from the Debye-Scherrer equation is slightly larger than for the nanopowder-derived catalyst, as expected from the BET surface areas. There is a smaller tungsten metal presence in this catalyst than seen in figure 5.6. It is unclear why the different precursors should give different intensities of the tungsten metal peaks, though it may be due to different metal oxide phases of the precursors undergoing reduction differently.

The mass activities and current densities per real surface area are shown in figure 5.8 (below)

Figure 5.8: Anodic hydrogen oxidation current on tungsten carbide catalysts corrected to unit mass (left) and real surface area (right). Tungsten carbide catalysts prepared by carburising tungsten oxide nanopowder (open) and polymer precursor (filled). Currents are steady-state, taken after 600s chronoamperometry. Currents measured in half cell in 75°C perchloric acid vs MMSE, corrected to reversible hydrogen electrode scale.

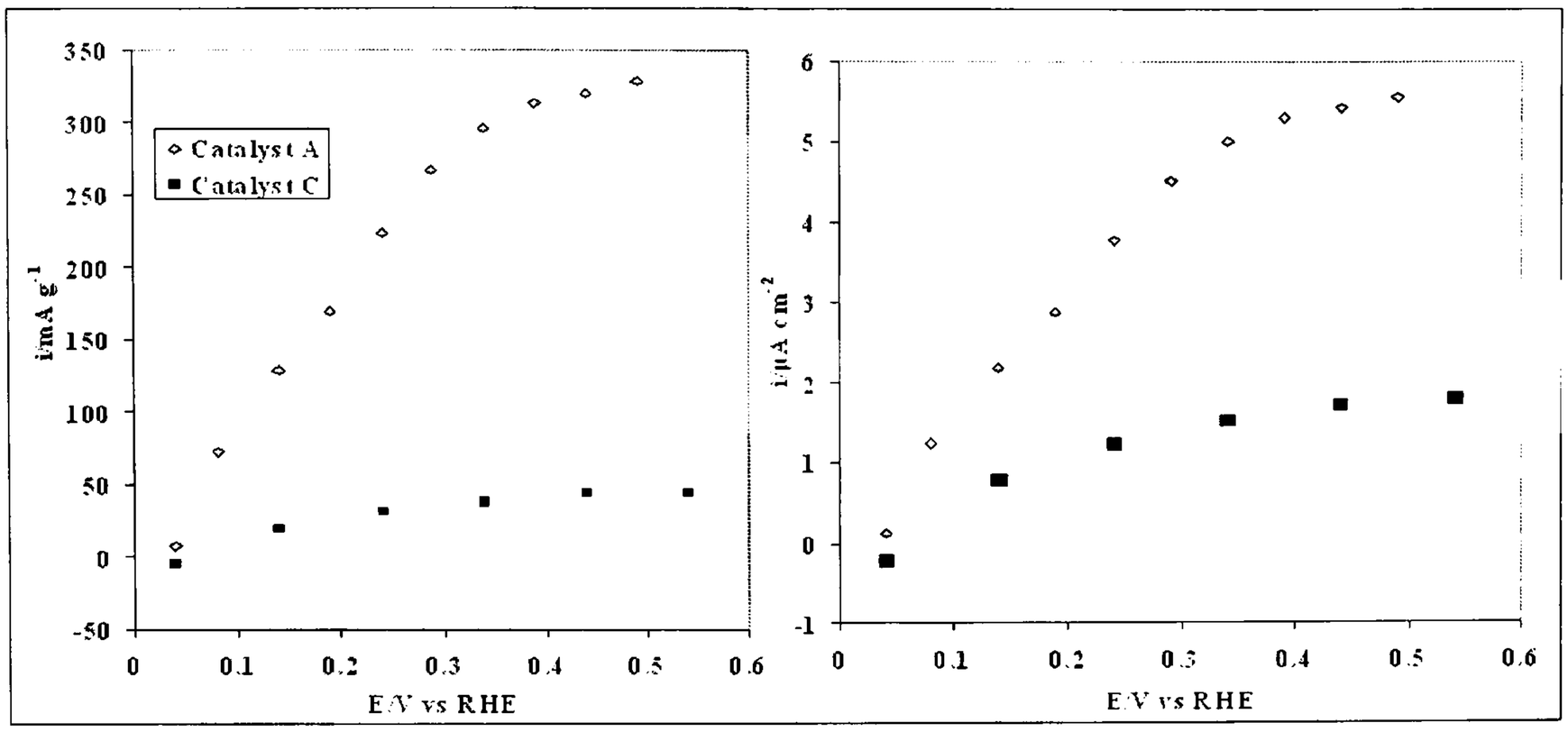

The mass activities for tungsten carbide catalysts are several orders of magnitude below the mass activities observed for state of the art platinum catalysts. However, there is major cost constraint associated with the use of platinum in a practical fuel cell. There are two reasons for this. The high cost of the platinum metal itself has been noted. Furthermore, platinum catalysts at PEM fuel cell temperatures require a carbon monoxide content lower than 10 ppm [4]. This means that the hydrogen fuel must undergo energetically and spatially costly refinement, particularly if the fuel is produced from a reformer. A fuel cell anode with a tungsten carbide catalyst would tolerate a much larger carbon monoxide content, enabling the fuel cell to operate from CO-rich reformate output, significantly reducing the fuel processing costs. In this respect, the tungsten carbide synthesised and tested in this work shows some promise for fuel cells for certain applications. The much-reduced current density for tungsten carbide would perhaps prevent their use in mobile and personal electronics applications, but for larger scale and automotive uses, these catalysts justify ongoing research interest. The polymer precursor method has been shown to produce a

precursor that gives a catalyst of comparable surface area to that obtained from tungsten oxide nanopowder. The catalytic activity of this catalyst was somewhat lower than that seen for catalyst A; it may be that different reaction conditions for the reduction and carburisation of polymer precursor tungsten oxide are required for optimum activity. The polymer precursor method has been shown to produce a tungsten carbide catalyst at moderately high dispersion and modest catalytic activity. This method offers a convenient route to small particle tungsten carbides; it is energetically efficient and essentially a "one-pot" chemistry method that could be easily scaled up to give large volume production.

The slight enhancement in current when testing catalyst A in perchloric acid compared with sulfuric acid suggests that the performance of these catalysts is dependent on their electrolyte environment, and an assessment of their performance in solid polymer electrolyte is required to predict their behaviour in fuel cells.

There is a considerable effect of increasing the temperature of the electrolyte. It may well be that tungsten carbide catalysts are better suited to higher temperature fuel cells such as phosphoric acid fuel cells, given the elevated temperatures at which the catalysts are passivated.

5.4 Conclusions.

This work confirms that tungsten carbide is a promising non-noble metal replacement for platinum in PEM fuel cells. The mass activities of these catalysts are significantly lower than that seen with state of the art platinum catalysts, and a high loading (WC at 25 mg cm^{-2} compared to Pt at around 0.5 mg cm^{-2}) for the performances seen for these catalysts. Nevertheless, the currents seen for catalyst A at 75°C represents promising performance, particularly in the context of the low cost of tungsten carbide

and the resistance of the catalyst to poisoning by carbon monoxide. Furthermore, this work details a novel application of the polymer precursor method, for producing well-dispersed tungsten oxide particles, to the production of tungsten carbide catalysts. Pechini-method tungsten carbide was produced with an area comparable to that seen for tungsten carbide produced from 25.3 $\times 10^4$ cm^2 g^{-1} tungsten oxide nanopowder.

In this work, the electrocatalytic activity of tungsten carbide on a glassy carbon rotating disk electrode in 0.5 mol dm^{-3} sulfuric acid sparged with hydrogen was found to be insufficient to produce a current limited by transport of reactants. This was found to be the case even at potentials where a noticeable anodic current was observed in a half-cell arrangement. It may be that the catalytic activity, and therefore the currents passed for the oxidation of hydrogen are simply too low to be resolved into a transport limited current. An alternative route to finding the transport limited current on these catalysts when employed as a fuel cell anode must be sought.

The current density for hydrogen oxidation on the resulting catalysts was lower for the polymer precursor method catalyst. This reduction has been ascribed to possible differences in surface composition in superficially similar catalysts. The passivation process has been shown to affect the activity of the tungsten carbide catalysts greatly, as have the composition and temperature of the reducing-carburising gas mixture. Therefore the reduction-carburisation-passivation process undergone by the catalysts may not give optimum surface activity for different tungsten oxide structures, produced in different ways.

Chapter 6: Fuel Cells With Tungsten Carbide Catalysed Anodes.

6.1 Introduction.

In order to fully investigate the effectiveness of tungsten carbide catalysts for fuel cells, anodes catalysed with tungsten carbide materials were included in a full fuel cell along with a high surface area platinum on carbon electrode developed using Johnson Matthey catalysts. Tungsten carbide materials have been shown in chapter 4 to have electrocatalytic activity towards the oxidation of hydrogen in acidic electrolyte. Inclusion in a full fuel cell under typical PEMFC operating conditions is a logical next step in the assessment of whether these materials hold promise to replace or reduce the platinum and other noble metals which contribute to the capital costs of the units. As has been noted in chapter 5, these materials have been examined in the literature as promising replacements for platinum, but very little work has been done to establish their performance in a polymer electrolyte membrane environment, and a full fuel cell with an anode with tungsten carbide has yet to be extensively investigated. A phosphoric acid fuel cell anode with tungsten carbide catalysts was reported with a performance of around 35 mA cm^{-2} at a 200mV overpotential [83].

In this section, a fuel cell anode made from tungsten carbide as synthesised in chapter 5 was manufactured and tested for background corrosion current, hydrogen oxidation activity and carbon monoxide tolerance. Tungsten carbides manufactured by carburising tungsten oxide nanopowder and by a Pechini-type method were investigated.

6.2 Experimental

The fuel cell testing apparatus was as described in the general experimental chapter. Electrodes were 1.5 cm × 1.5 cm squares. The anode was constructed by evaporating an ink consisting of 10 wt% Nafion 1100 solution in water (Aldrich, UK), and water (Millipore) and the tungsten carbide material of choice, as synthesised in chapter 4; Nafion content was calculated to give a 25 wt% Nafion binder. Anode catalyst loading was 25 mg cm^{-2}. The substrate was carbon paper (Toray) with PTFE wetproofing (6 wt%) and the ink was added dropwise and evaporated at room temperature. Evaporation at elevated temperatures was avoided to prevent dehydration and shrinkage of the Nafion binder, which can dislodge the catalyst layer. The cathode catalyst was a proprietary Johnson Matthey high surface area platinum on carbon electrode. The polymer electrolyte membrane was a Nafion 117 membrane cut larger than the electrodes. The membrane was prepared by boiling in 3 wt% H_2O_2 for 30 mins, then 0.5M H_2SO_4 for 30 mins, then two changes of Millipore water (18 MΩ cm, Millipore, Watford, UK). The membrane was then dried under reduced pressure at 80°C. The membrane-electrode assemblies were manufactured by hot pressing electrodes and membrane at 155°C and 75 kg cm^{-2} (7.36 MPa). The MEA was mounted in a fuel cell unit between machined graphite blocks containing a serpentine gas flow channel. Reactant gases were supplied to the electrodes via mass flow controllers (Bronkhorst, Netherlands). The hydrogen gas was humidified by feeding it through a Nafion gas drying tube (PermaPure, Toms, NJ) supplied with heated water. The cell itself was heated with cartridge heaters and its temperature was regulated by PID controllers (Omron, Schaumburg, IL). The fuel cell was tested using a potentiostatic current load made in-house. The fuel cell curves were tested following 0.5 s polarisation at each point. Fuel cell curves were recorded

by a NI Labview program created in-house. Hydrogen (High Purity grade), compressed air and a 100ppm CO in hydrogen mix were supplied by BOC. Nitrogen (BIP grade) was supplied by Air Products.

6.3 Results and Discussions.

6.3.1 Polarisation of a WC Fuel Cell Anode in the Absence of Hydrogen.

It is important to isolate any currents not due to the anodic oxidation of hydrogen. It is anticipated based on the results in section 5.2 that there will be a small background current attributable to the corrosion of the catalyst, as there is a small current seen when tungsten carbide based electrodes in the half cell were supplied by inert gases.

The tungsten carbide anodes were tested for background currents by supplying the anode side of the fuel cell with nitrogen gas, and the platinum cathode was fed with humidified hydrogen, in order that it would act as a counter and reference electrode. The cell was polarised by scanning the potential from 0V to 0.6V, and the resulting voltammogram was recorded.

Figure 6.1: Background currents for fuel cell with tungsten carbide (A) anode and JM Pt cathode. Humidified hydrogen gas fed to Pt electrode. Nitrogen (25 cm^3 min^{-1}) fed to tungsten carbide electrode. Hydrogen gas humidified at 70°C. Fuel cell heated to 65°C. Scan rate 1 mVs^{-1}.

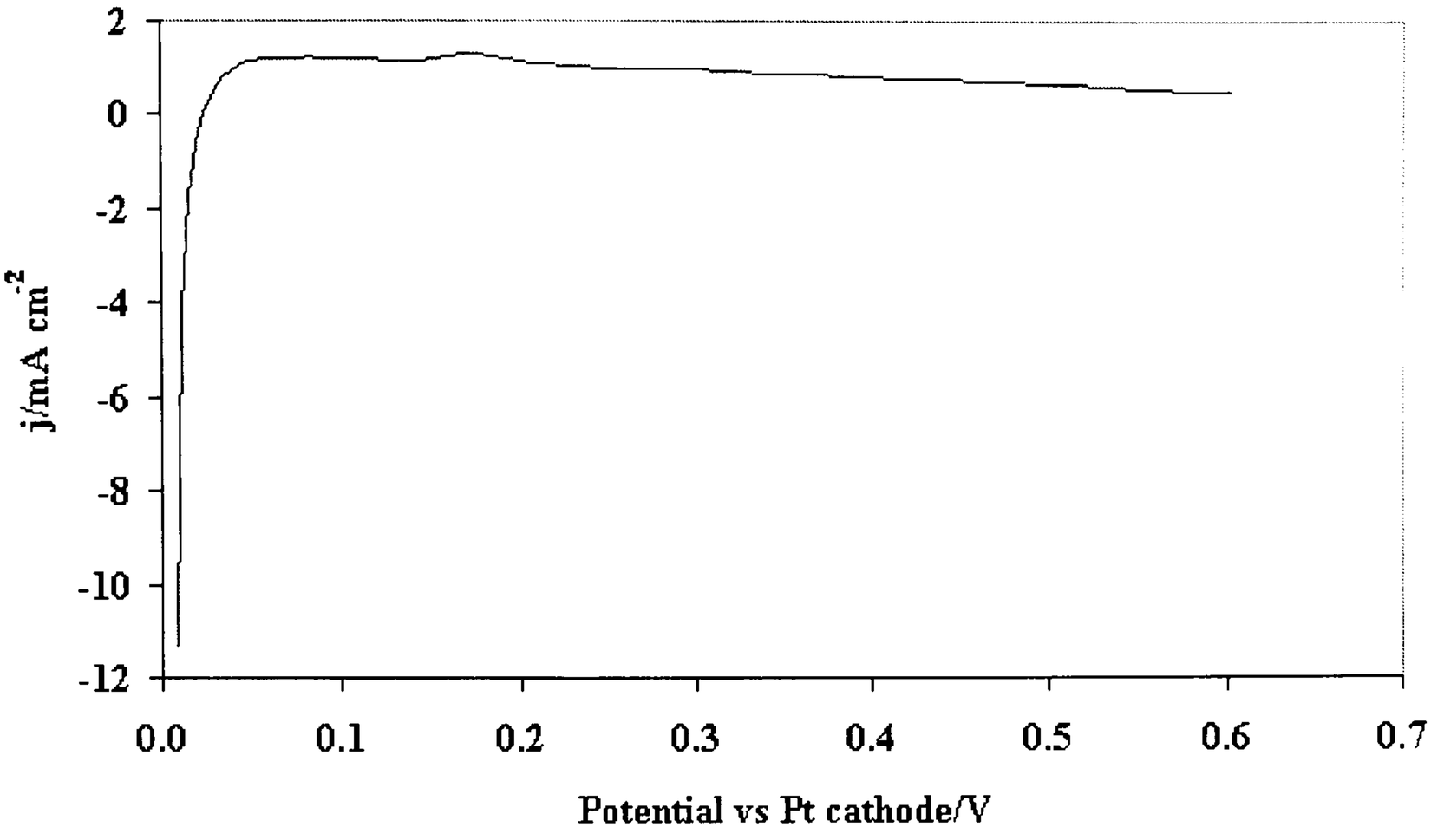

This voltammogram indicates that there is a modest but significant background current, which is observed when the fuel cell anode is fed with an inert gas. The currents above equate to a corrosion current in a fuel cell of 41.2 $\mu A\ mg^{-1}$ catalyst. This compares with a far lower value of 0.244 $\mu A\ mg^{-1}$ catalyst for the half-cell results when fed with inert argon. Tungsten carbides are regarded as resistant to corrosion in acidic environments [38]. Fuel cell anode catalysts are required to be resistant or largely resistant to corrosion in acidic electrolyte environments, and it is significant that the catalyst shows a higher corrosion current in the solid polymer fuel cell environment. The superacidic environment of the Nafion membrane may be contributing to the accelerated corrosion of the catalyst. It is also possible that there was greater electrolyte access to the surface of the carbides in the Nafion-bound anodes in a fuel cell than in the extensively wet-proofed PTFE bound working electrodes of the gas fed half-cell. The corrosion current in the fuel cell environment may have implications for the implementation of these catalysts for fuel cells where long term use is desired. It should be noted that there may be an effect of hydrogen

crossover, as the tungsten carbide electrode under test is in close proximity to the hydrogen-fed platinum cathode.

6.3.2 Operation of WC Fuel Cell Anodes on Pure Hydrogen.

Polarisation curves were obtained for fuel cells equipped with anodes constructed from catalyst A, prepared by carburisation of tungsten carbide nanopowder, and from catalyst C, prepared by a Pechini-type method. The resulting polarisation and power curves are shown in figure 6.2.

Figure 6.2: Fuel cell currents and power density for tungsten carbide (catalysts A and C) anode and JM Pt cathode. Humidified hydrogen gas fed to anode at 15 cm^3 min^{-1}. Air (25 cm^3 min^{-1}) fed to Pt cathode (fuel cell test). Hydrogen gas humidified at 70°C. Fuel cell heated to 65°C. Data points recorded after 0.5 s at each point.

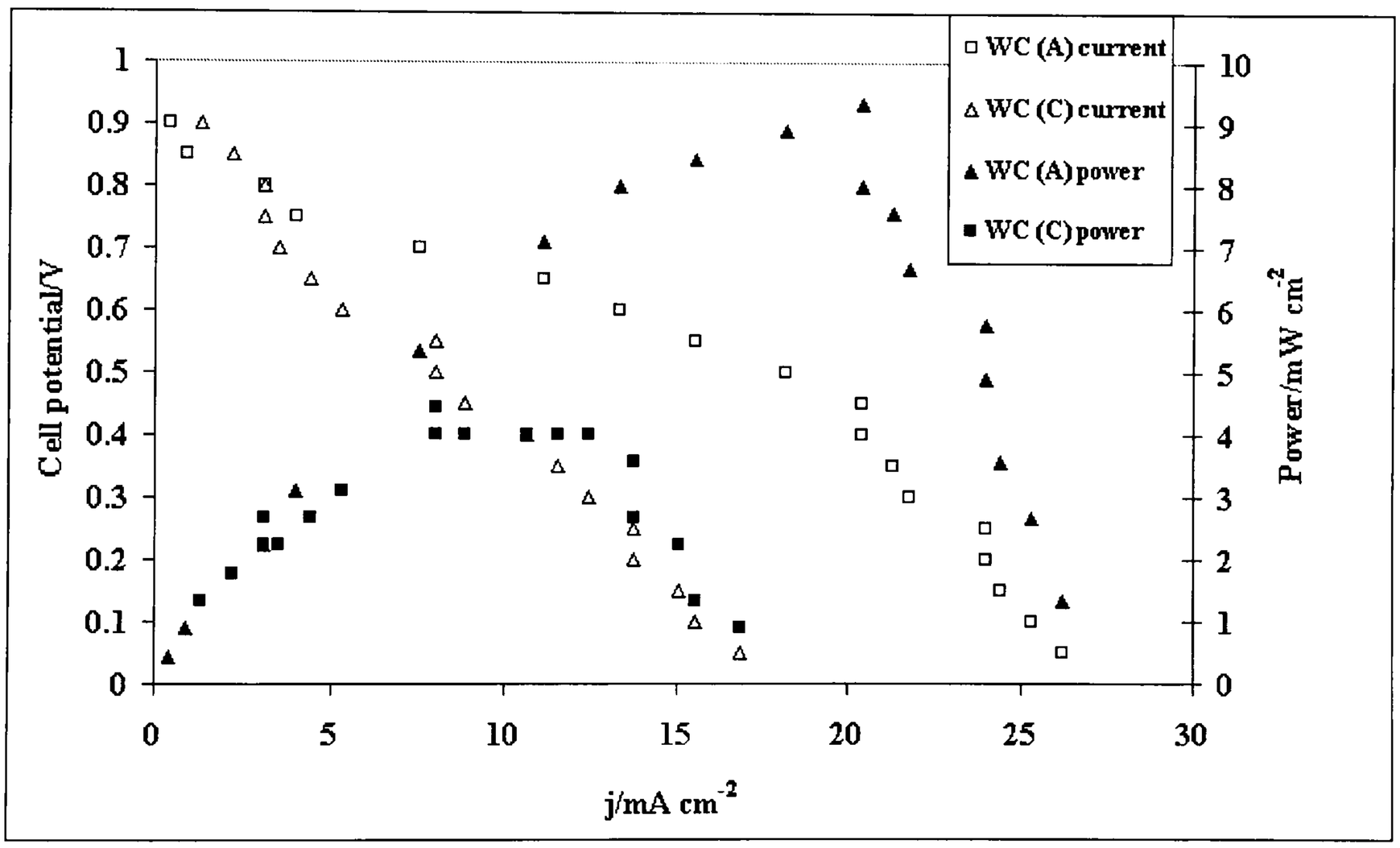

The results shown in figure 6.2 illustrate the potential for a fuel cell with a tungsten carbide based anode, albeit confirming the modest performance seen in chapter 4. The currents seen are in line with those expected from the assessment of the catalysts' performance in aqueous acidic electrolyte. The reasons for the limited performance of the fuel cells relate largely to the modest catalytic activity of the tungsten carbide catalysts on the anode. It can be seen from the conditions that the fuel cell is

operating at substantial excess stoichiometry. Fuel cell stoichiometry is the ratio of reactant supply to the minimum supply of reactants required for a given current, according to Faraday's law. Supplying the fuel cell with hydrogen at 25 cm^3 min^{-1}, with a current of 15 mA cm^{-2} means a hydrogen stoichiometry of 107, and an air stoichiometry of 42. The cell is not therefore expected to be starved of reactants. The form of the curve suggests that the cell does not approach diffusion limitation, as there is no rapid collapse of the current values as the cell potential approaches zero. The expected form of a polarisation curve for a hydrogen-air fuel cell is shown and discussed in chapter 1 (introduction). That the polarisation curves shown here do not approach a limited current suggests that the catalytic action of tungsten carbide fuel cell anodes is compromised by overpotential losses for hydrogen oxidation on the tungsten carbide. The difficulties in calculating a kinetic current density for hydrogen oxidation on tungsten carbides in chapter 5 mean it is difficult to isolate the exact regions of kinetic and transport limited current, and the background currents seen around the thermodynamic potential for hydrogen oxidation in figure 5.1 complicate any effort to construct a Tafel plot for this reaction.

However, the fuel cell currents for these catalysts are considerably higher than those seen for the half-cell reactions with the same catalysts studied in chapter 5. This could be due to the improved access to more of the catalyst when removed from the aqueous electrolyte environment. The diffusion current of hydrogen in Nafion is 4.5×10^{-6} cm^2 s^{-1} [85] is higher than the value in 0.5 mol dm^{-3} aqueous H_2SO_4, at 3.8×10^{-5} cm^2 s^{-1} [79] at 298K. The diffusion of hydrogen in fuel cell GDEs is a complicated problem of diffusion in gaseous and liquid phases, and in the gaseous phase the self diffusion coefficient at 273.15 K is much higher, at 1.28 cm^2 sec^{-1} [86]. Certainly the gaseous reactant access to some proportion of the catalyst is expected to

be more favourable in the case where the catalyst is bound on a 6wt% PTFE carbon paper electrode with Nafion and without liquid electrolyte than in the half cell case, where the need to prevent flooding required a higher PTFE content and a PTFE catalyst binder.

The fuel cell currents for both catalysts, prepared by different methods as described in chapter 5, are similar as expected. The activity exhibited by catalyst A, prepared by carburising tungsten oxide nanopowder as detailed in chapter 5, is slightly higher than that seen for catalyst C, prepared by a Pechini-type method. These results are expected in light of the half-cell results seen in chapter 5. The slightly higher performance of catalyst A is expected given its higher surface area as found by BET measurements reported earlier. Figure 6.3 (below) shows the fuel cell currents normalised by the real surface area of the catalysts, as found by BET analysis.

Figure 6.3: Fuel cell data from figure 6.2 (above) corrected for BET surface area of catalysts. Humidified hydrogen gas fed to anode at 15 ml/min. Air (25 ml/min) fed to Pt cathode (fuel cell test). Hydrogen gas humidified at 70°C. Fuel cell heated to 65°C. Data recorded after 0.5s at each point.

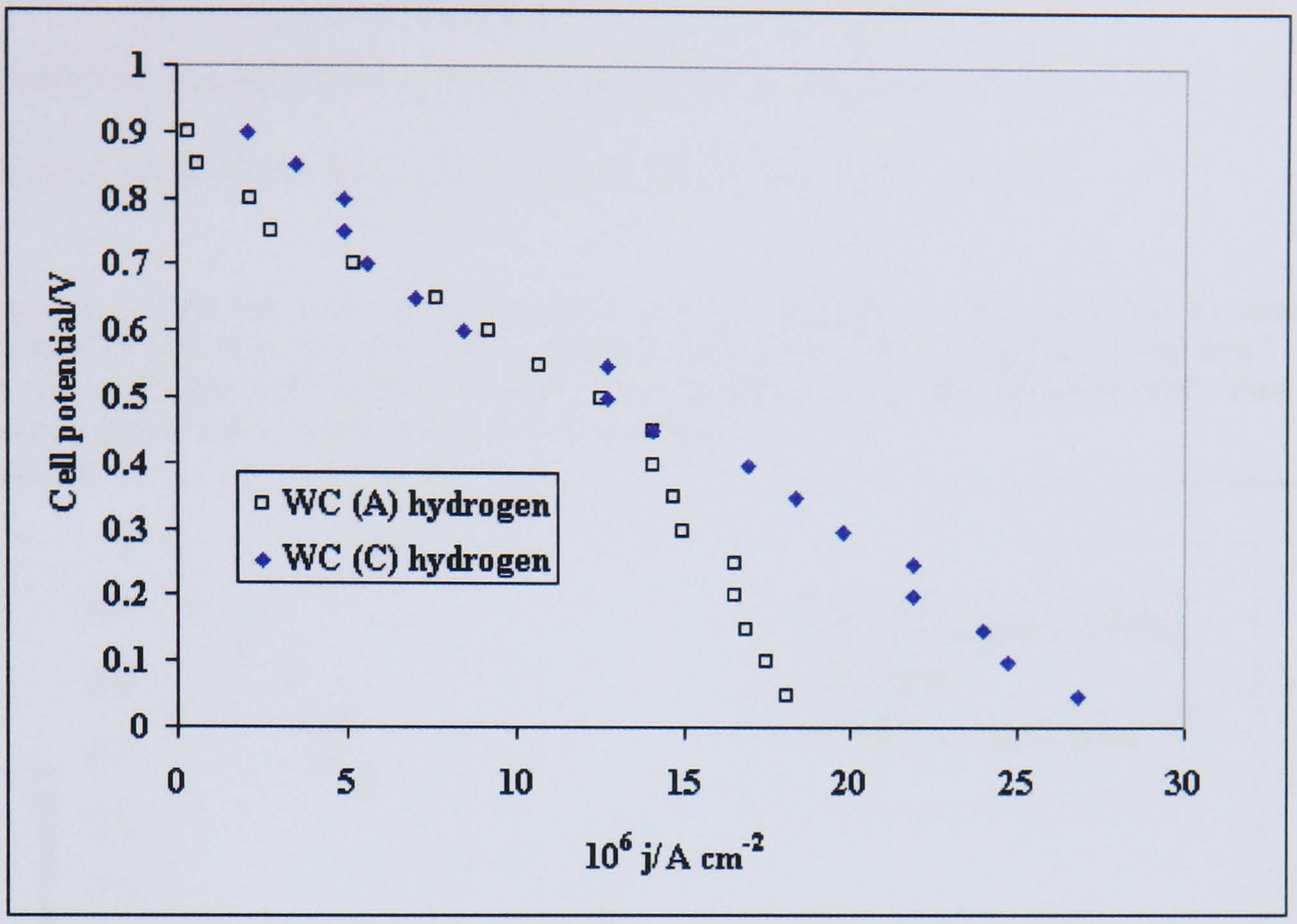

As the catalytic activity may be substantially affected by small changes in the preparation method, it may be expected that the different synthetic methods will yield catalysts with different surface phases. However the performance of the catalysts in the full PEM fuel cell environment appears to reflect their activities in the half cell with aqueous acid electrolyte; the relatively lower currents obtained for polymer precursor method catalyst C are expected due to its slightly lower BET surface area; the catalytic activity per unit BET surface area is actually slightly higher for catalyst C in the full fuel cell environment. Typically fuel cell catalysts would be assessed by electrochemically active surface area; this is hampered by the fact that there is no electrochemical method to measure the surface area of tungsten carbide electrochemically.

6.3.3: Operation of WC anodes in the presence of CO.

The fuel cell with anode catalyst C was assessed for CO tolerance of its anode. The humidified hydrogen was replaced with hydrogen containing 100ppm CO for 1hr and a further polarisation curve was obtained, shown in figure 6.4, below.

Figure 6.4: Fuel cell currents for tungsten carbide (catalysts C) anode and JM Pt cathode. Humidified hydrogen gas, pure and containing 100ppm CO fed to anode at 15 cm^3 min^{-1}. Air (25 cm^3 min^{-1}) fed to Pt cathode (fuel cell test). Hydrogen gases humidified at 70°C. Fuel cell heated to 65°C. Data recorded after 0.5s at each point.

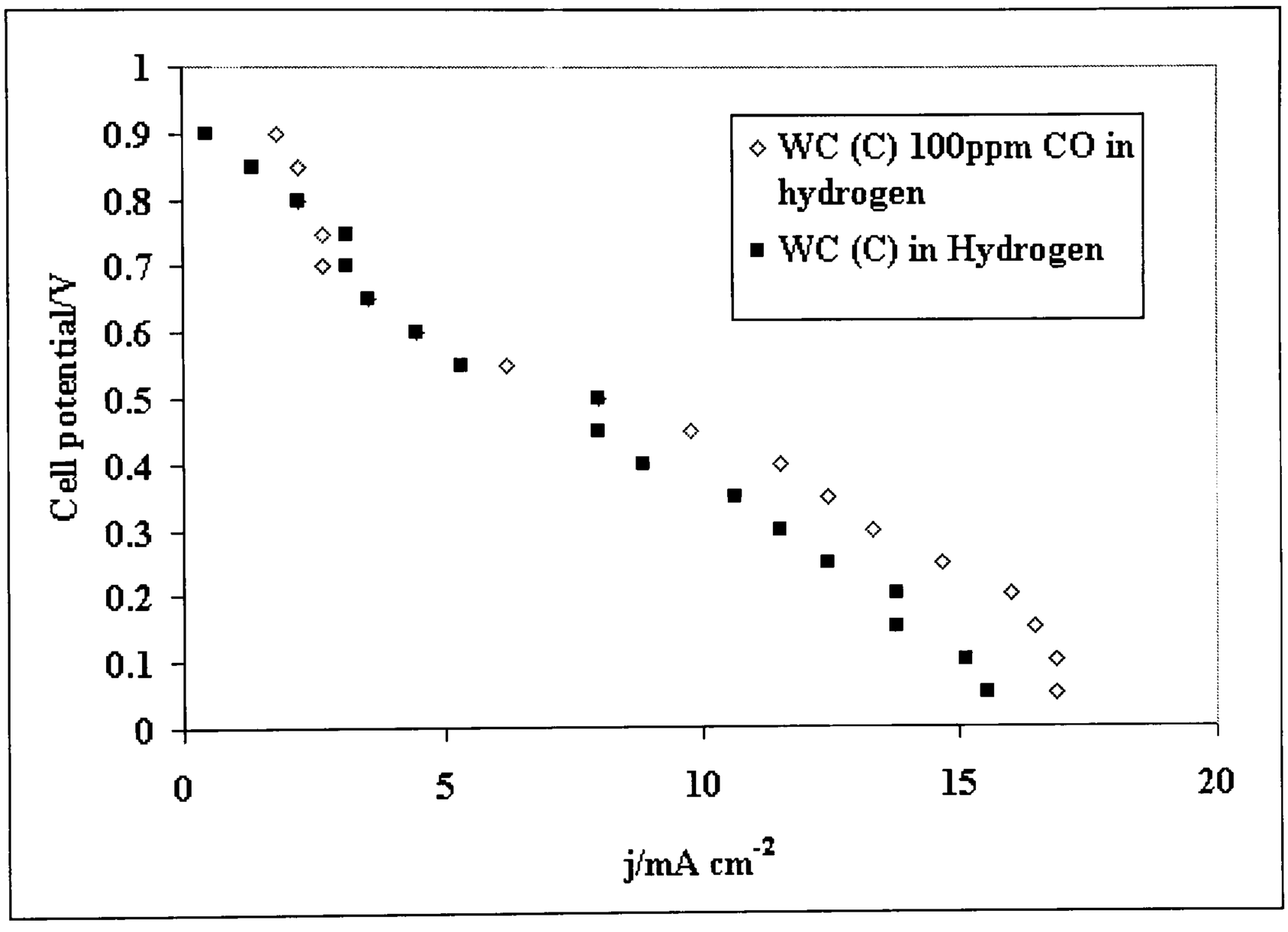

The carbon monoxide tolerance of these anode catalysts was demonstrated by the performance of the fuel cell with tungsten carbide catalyst C under conditions that would poison a conventional platinum based fuel cell anode. 100ppm CO in hydrogen was supplied to the anode for 1hr, and the polarisation curve was recorded. It can be seen that the addition of carbon monoxide to the fuel stream does not poison the catalysts. Indeed, the performance of this fuel cell anode with 100ppm CO slightly exceeds that seen in pure hydrogen, though this may be within experimental error variations. The absence of a CO poisoning effect represents a major advantage of

tungsten carbides and other base metal catalysts over platinum and noble metal catalysts. There is a substantial incentive to develop CO tolerant anodes for fuel cells, as the CO poisoning of platinum catalysts prevents the use of impure hydrogen based fuels, such as methanol reformate and natural gas reformates. The requirement for a gas processing step to remove CO from hydrogen adds substantially to the additional engineering costs and system bulk, which is particularly detrimental to mobile applications.

6.4 Conclusions.

There is clearly a capacity to develop fuel cell anodes based on non-precious metal catalysts for fuel cells. The performance of the tungsten carbide catalysts studied in this chapter is undoubtedly modest, but the benefits of fuel cell systems developed using these catalysts lie in the much reduced cost of tungsten-derived catalysts compared to platinum and other precious metals, even at the higher catalyst loadings employed. In addition, the CO tolerance of these anodes may make fuel cell anode catalysts based on tungsten carbides and other base metals the preferred choice for certain fuel cell types where the fuel supplied is high in carbon monoxide, such as reformates.

Chapter 7: Fuel Cell Testing of Sputter Deposited Catalysts.

7.1 Introduction.

Having demonstrated that sputter deposited platinum yields a high electrochemically active surface area at low loading and minimal thickness, catalysts layers based on this deposition method would appear to be ideal for use in a PEM fuel cell. The results of chapter 2 show that there is a catalyst deposition technique that can provide a highly active platinum layer for both the fuel cell anode and cathode. The high roughness factors observed- 130 to 150 depending on the substrate- at low loadings are a major advantage of this catalyst deposition technique. However, it is the thinness of the catalyst layers on these membranes that represents their real advantage. The specific roughness factor, **a**, is $(1.1 \pm 0.3) \times 10^9$ m^2 m^{-3} (see chapter 2); this should be compared to the value calculated for a proprietary fuel cell electrode from E-TEK inc. $\mathbf{a} = 1.59 \times 10^6$ m^2 m^{-3} based on the data of Hirano et al [17]. The high roughness factor per catalyst layer volume is significant because of the narrow region over which fuel cell reactions take place, especially at high overpotentials. Therefore this catalyst structure is thought to make highly efficient use of the platinum available [87].

There have been several previous studies of full fuel cell performance tests in the literature [19, 88]. In this section, polarisation curves for fuel cells with reactively sputtered anodes and cathodes are presented. In addition, a model for the electrode structures is presented that attempts to demonstrate the extent of utilisation of the catalyst in this electrode structure. Porous electrodes have been extensively studied, and their modelling falls into several main classes. Homogenous models treat the

boundary between electrode and electrolyte as a single homogenous region, simplifying the requirement for detailed understanding of the structure of the electrode itself [89]. This model requires an assessment of the surface area of the internal surface of the electrode pores. Quasihomogenous models are based on modelling the three-phase region and applying this model to what is known about the pore structure. Statistical models use simplified representations of the porous electrode structure, such as modelling the pores as a linear cylinder throughout the thickness of the catalyst layer. Other approaches to understanding porous electrodes include the flooded agglomerate model and the thin film model [90, 91]. The model employed below for studying thin catalyst layers is based on the simple pore model [92]. The model was originated by Srinivasan *et al* [93]. This model is considered appropriate for analysis of the performance of these electrodes because of the highly porous nature of the sputter deposited layers, and the minimal thickness of the layers. Sputter deposited catalyst layers consist of a single metallic phase with extensive catalytic reaction sites within the layer. In contrast, catalyst layers with supported platinum particles on carbon need to take account of the dispersion of the catalytic sites within the layer. Such structures are often modelled using a macro homogenous model [90]. The simple pore method has been used for regular mesoporous catalyst structures [94]. In this work the simple pore method is the preferred approach for the analysis of the performance of sputter deposited electrodes because of its simplicity and suitability.

It is the aim of this work to demonstrate that reactively sputtered catalyst membranes hold promise for a new approach to fuel cell catalyst layer structures. In this section full fuel cell tests were carried out to establish the performance of fuel cells equipped with reactively sputtered electrodes.

7.2 Experimental.

Catalyst layers were prepared by sputtering platinum from an oxygen atmosphere onto Nafion membranes or carbon gas diffusion electrodes. Platinum was sputtered at 75 mA for 960 s with a plasma gas pressure of around 7×10^{-3} mbar (0.7Pa) oxygen. Substrates were Nafion 117 membranes or carbon gas diffusion electrodes made from 4 mg cm^{-2} XC72R carbon (Vulcan) bound with 20 wt% PTFE. Nafion membranes and gas diffusion electrodes were prepared as reported in chapter 2 (experimental section). The deposited metals were reduced electrochemically; as detailed in chapter 2. Membrane electrode assemblies were formed by hot-pressing two carbon gas diffusion electrodes at 75 kg cm^{-3} (7.36 MPa), 154°C. MEAs were mounted in a fuel cell between graphite current collectors with a 1.5 cm × 1.5 cm serpentine gas flow field. Connections to the graphite current collectors were made via brass end plates. Reactant gases were supplied to the electrodes via mass flow controllers (Bronkhorst, Netherlands). Hydrogen gas (BOC, Premier grade) was supplied to the anode via humidification in a Nafion tube (PermaPure, Toms River, NJ) fed with heated water, thermostatically controlled. Air was supplied to the cathode (BOC). The fuel cell itself was heated with cartridge heaters (RS Ltd, Corby), under PID control (Omron, Schaumburg, Il., with K-type thermocouple sensing, RS Ltd).

Fuel cell tests were performed using a current load under potentiostatic control manufactured in house. Current data was recorded at each potential after 0.5 s.

7.3 Results and Discussions.

Figure 7.1 below shows a polarisation curve for a fuel cell with reactively sputtered catalyst on the Nafion membrane (filled circles) and with reactively sputtered catalyst on the carbon gas diffusion electrodes (open circles). The catalyst loading for these

sputtering conditions was found to be 0.15 mg cm^{-2}; identical amounts were sputtered on anode and cathode. The cell was supplied with hydrogen at 20 cm^3 min^{-1} humidified at 70°C, and air at 25 cm^3 min^{-1}. The cell was heated to 65°C. For comparison, a polarisation curve of an MEA with conventional platinum on carbon fuel cell electrodes (Johnson Matthey, UK), otherwise prepared identically, is shown (crosses). Figure 7.2 below shows the power curves for the same fuel cells.

Figure 7.1: Polarisation curves for fuel cell with reactively sputtered platinum on membrane (filled circles) and on gas diffusion electrodes (open circles). Cell heated to 65°C; hydrogen (20 cm^3 min^{-1}) humidified at 70°C, cathode supplied with air (25 cm^3 min^{-1}). Pt on carbon electrodes (data from chapter 4) same conditions: crosses. Data recorded after 0.5s at each point.

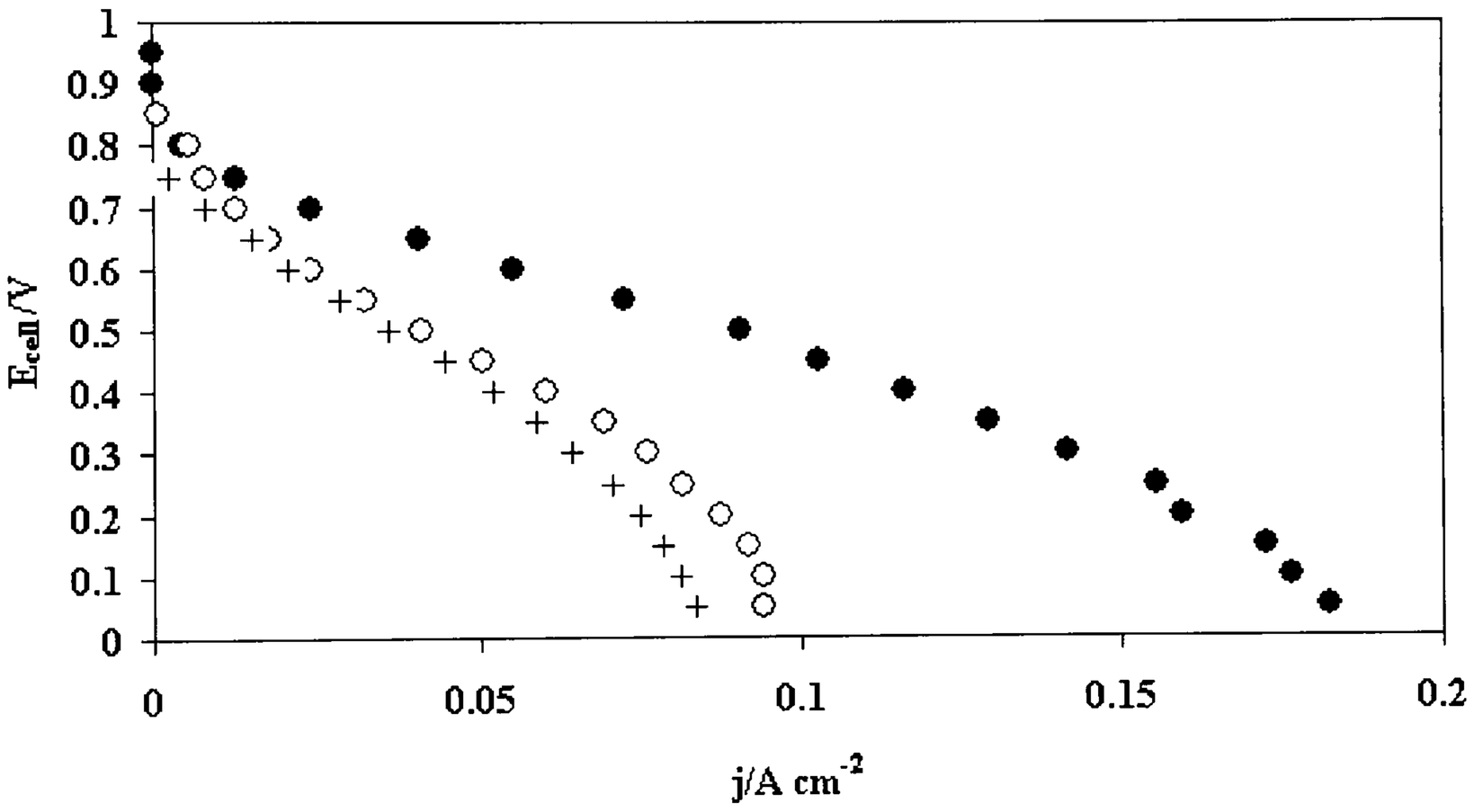

Figure 7.2: Power curves for same fuel cells. Cell heated to 65°C; hydrogen (20 cm^3 min^{-1}) humidified at 70°C, cathode supplied with air (25 cm^3 min^{-1}). Pt on carbon electrodes (data from chapter 4) same conditions: crosses. Data recorded after 0.5 s at each point.

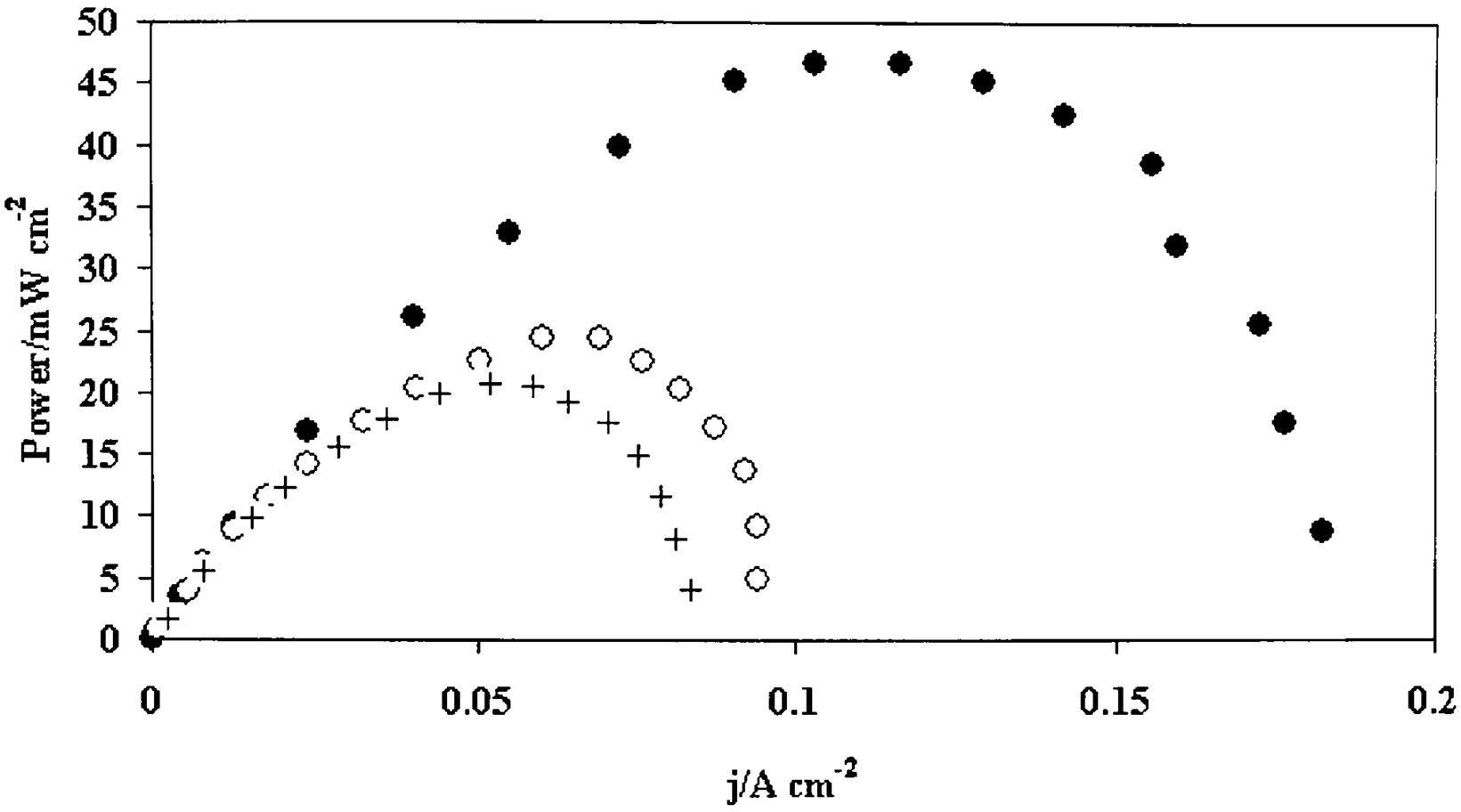

In both cases, sputter deposition of platinum has been shown to give fuel cell electrodes of reasonable activity. The high performances seen by O'Hayre *et al* [19] have not been replicated, but there is sufficient activity to suggest that this method of catalyst deposition is a promising technique for the manufacture of fuel cell electrodes.

As discussed in chapter 1- introduction, there are many factors that limit the performance of the fuel cell. The slow oxygen kinetics of the oxygen reduction reaction (ORR) on a platinum cathode is blamed for much of the loss in fuel cell performance at acceptable current densities. The increased surface area of the fuel cell electrodes at minimal loading penalty is suggested as a means by which a sputter deposited fuel cell electrode can circumvent this problem. A related problem of oxygen transport to the cathode limits activity at high overpotentials. Under these conditions the minimal thickness of the sputter deposited catalyst layers is suggested as an advantage, giving oxygen molecules short diffusion lengths to reach the three-phase area of the catalyst, electrolyte and gaseous phases. At the anode, the kinetics

of the hydrogen oxidation reaction are relatively more rapid and facile; however a high surface area remains an asset on the anode to maximise hydrogen oxidation rate. In addition the thin catalyst layer is expected to give rapid reactant transport to all available platinum, though transport of reactants is more facile at the anode due to the rapid diffusion of hydrogen and the enhanced transport due to the pressure gradient caused by the gaseous reactant being consumed.

The goal of sputter deposition in this work is to localise a thin film of platinum catalyst on the face of the Nafion electrolyte, in intimate contact with the electrolyte and at high surface area. Sputter depositing the platinum directly onto the membrane satisfies the requirement to bring a large amount of the high surface area platinum into contact with the electrolyte. Depositing the catalyst on the carbon gas diffusion electrodes ensures the catalyst is in intimate contact with the electronically conductive phase and readily supplied with gaseous reactants through the porous carbon. However, this structure relies on the hot pressing process to bring the catalyst into contact with the electrolyte and may not yield the largest three-phase contact area possible under these circumstances. Conversely the deposition directly onto the Nafion means that the electronic conductive phase makes contact with the catalyst through the pressing process. The XC72R powdered carbon that forms the surface of the carbon gas diffusion electrode is anticipated to shift slightly under pressing conditions and distribute across the surface of the Nafion electrolyte. In addition the sputtered phase is expected to show an appreciable lateral conductivity, assisting electron transport from active catalytic sites. However, direct sputter deposition on the membrane may have a limited impact on the proton conductivity of the Nafion (see figure 3.4).

The current densities observed with direct sputtering of platinum onto the Nafion membrane are significantly higher, suggesting that the most efficient use of the catalyst is made by localising the catalyst on the Nafion membrane. Open circuit potentials are significantly lower than the thermodynamic cell potential of 1.23V. This result is expected in PEM fuel cells with platinum cathode catalysts because of the small but significant overpotential for oxygen reduction on platinum. The fuel cell polarisation curve then shows a region of ohmic resistance limited current. With sputter deposited electrodes, the polarisation curve (filled circles, figure 7.1) rapidly collapses with increasing potential, a feature consistent with reactant transport limitation of the fuel cell performance. In the case of the fuel cell with catalyst directly sputtered onto the electrolyte (open circles, figure 7.2), the polarisation curve does not show the transport limited feature to the same extent, and it appears that the current is limited by ohmic resistance at lower potentials down to short circuit. It is possible that the reduced membrane conductivity suggested by the results in chapter 3 is slightly impeding the fuel cell performance at lower cell potentials and higher current densities. The enhanced performance of the cell is ascribed to the success of the direct reactive sputter deposition technique in providing a thin, highly roughened catalyst layer in intimate contact with the electrolyte.

7.3 Modelling of Catalyst Utilisation.

The simple pore model of the catalyst layer is suggested as a mathematical model to understand the nature of the reactions taking place on the electrode. Among the claimed advantages for sputter deposited catalysts is the efficient utilisation of platinum based on the ability to localise the catalyst in a narrow zone at the surface of the electrolyte. The simple pore model is employed to demonstrate extent of the utilisation of catalyst at various overpotentials. The extent of utilisation is denoted ψ:

$$\psi = \frac{\lambda}{l} Tanh \frac{l}{\lambda}$$

Where l is the length of the pores. The parameter λ gives the penetration depth of the current:

$$\lambda = \left(\frac{nF\gamma Dc^0}{2 j_0} \right) \exp\left(\frac{-\beta F \eta}{RT} \right)$$

Where n is the number of electrons involved in the reaction, F the Faraday constant, γ the pore radius, D is the diffusion coefficient; c^0 the bulk concentration of the reactant and j_0 is the exchange current density. β is the symmetry factor, η the overpotential R the gas constant and T the temperature. In the model used here, the pore length was set to the calculated thickness of the film, 140nm. The pore radius was calculated, based on the porosity of the film and the specific surface area, to be 0.913 nm. This figure represents a very narrow pore channel size, and would give an extremely high density of pores on the surface of the catalyst layer, at 1.91×10^{13} cm^{-1}. The pores are spaced at 2.13 nm pitch based on a hexagonal close packed model of the pores. Modelling the pores in this way give perhaps an unrealistically narrow pore wall structure and high pitch, but the simple pore model captures the highly porous metal structure of the catalyst layer and is appropriate for a thin structure deposited directly on an electrolyte.

Figure 7.3 below gives the utilisation, ψ, for a sputtered fuel cell anode modelled using the simple pore model. The pores are assumed to be filled with Nafion due to the deposition of the catalyst on the membrane and hot pressing process; the diffusion coefficient D and c_0 of hydrogen in Nafion is taken from data in Ota et al [85]. The value of β is taken to be 0.5; j_0 is assumed to be 10^{-2} A cm^{-2} [92, 95]. The extent of catalyst utilisation is shown; values of ψ are given for overpotentials between 0V and

0.6V for the sputtered catalyst layer at 30°C and 65°C. For comparison, the extent of catalyst utilisation has also been calculated for a theoretical catalyst layer with the same structure but double the thickness.

Figure 7.3: Extent of catalyst utilisation for sputtered catalyst for hydrogen oxidation, simple-pore model. Solid line: 140nm catalyst (as used in this work), 338 K. Dotted line: 280nm catalyst layer, 338 K. Dashed line: 140nm catalyst (as used in this work), 303 K. Dotted-dashed line: 280nm catalyst layer, 303 K.

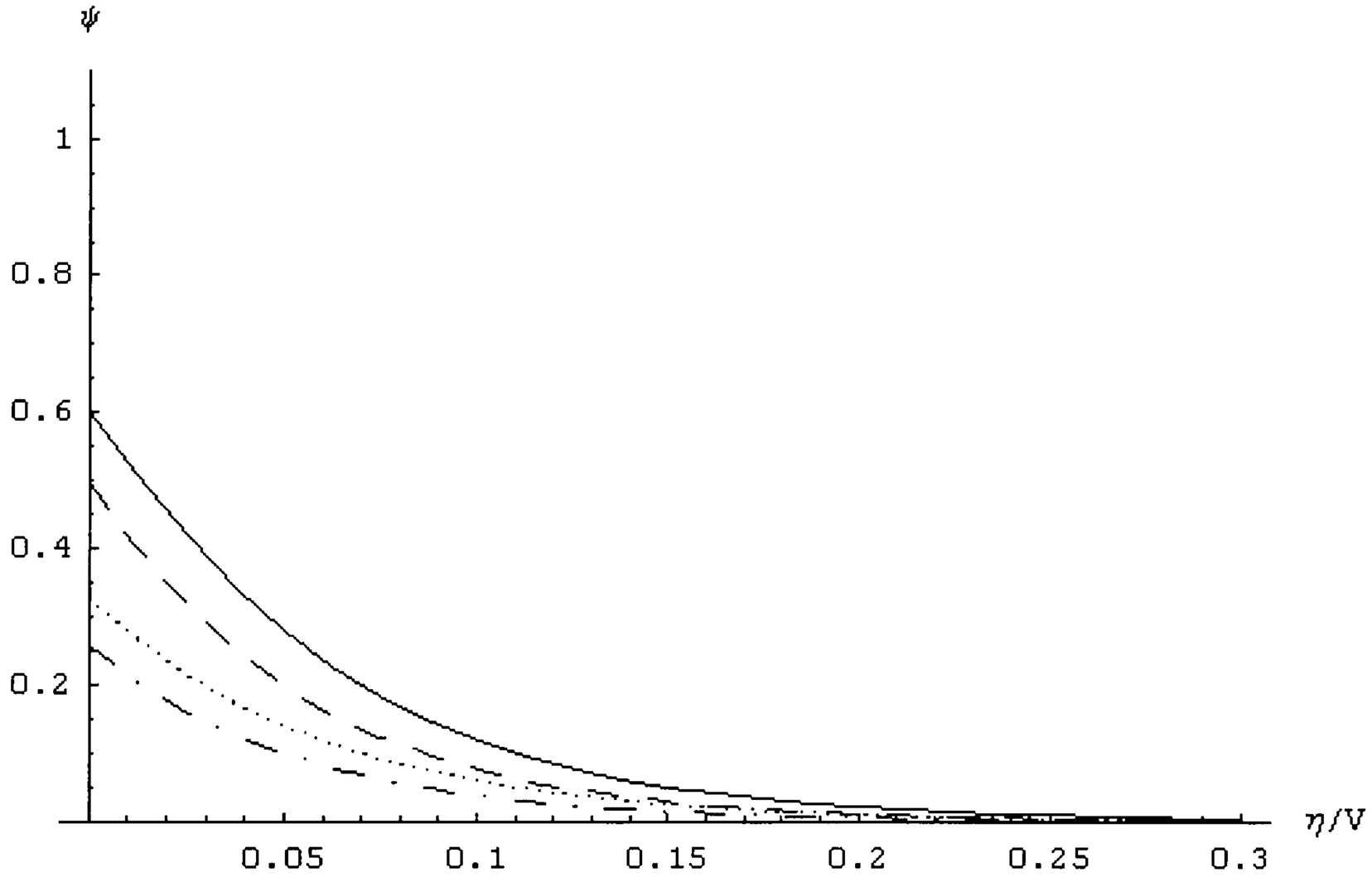

It is clear that, according to this model, the catalyst is not entirely utilised even at very low overpotentials on the fuel cell anode. It is not expected that a platinum fuel cell anode would operates at an overpotential greater than η=100 mV. The catalyst utilisation factor, ψ, rapidly decreases as the overpotential increases. The reduced catalyst utilisation at increased thickness confirms the importance of a thin porous layer in the efficient use of catalyst material.

Figure 7.4 below shows the same model applied to the sputtered fuel cell cathode, for the oxygen reduction reaction, and for an identical electrode of double thickness for comparison.

Figure 7.4: Extent of catalyst utilisation for sputtered catalyst for oxygen reduction, simple-pore model. Solid line: 140nm catalyst (as used in this work), 338K. Dotted line: 280nm catalyst layer, 338K. Dashed line: 140nm catalyst (as used in this work), 303K. Dotted-dashed line: 280nm catalyst layer, 303K.

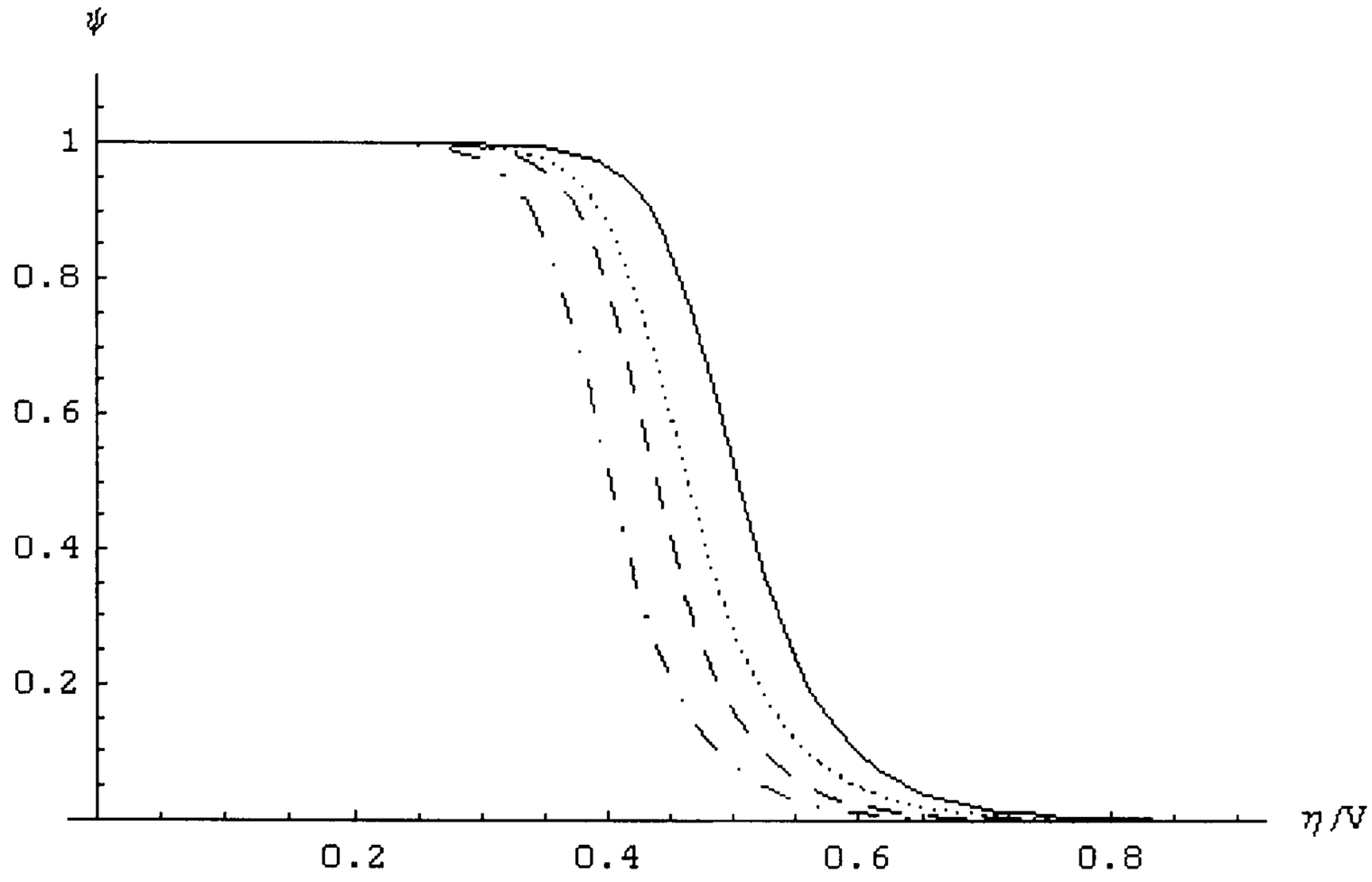

For the cathode, the difference in the extent of catalyst utilised is attributed to the lower exchange current density of the oxygen reduction reaction. At overpotentials below 0.45V at 303K, 0.5V at 338K, the catalyst is again almost entirely utilised, but as the overpotential increases the extent of catalyst utilisation rapidly decreases.

Again, the catalyst layer thickness is shown to have an effect on the extent of utilisation, reinforcing the conclusion that a thin, highly porous electrode makes the most efficient use of the catalyst material available.

This model confirms the need for a platinum catalyst layer to be as thin as possible for efficient use of the catalyst. However, at moderate overpotentials on both electrodes, the sputter deposited platinum layer is indeed largely utilised, particularly as the temperature is increased. As the overpotentials increase, we see a reduction in the extent of catalyst utilisation. It is anticipated that the electrode would exhibit an internal polarisation effect under these conditions of partial utilisation; the catalyst

layer would not behave as a homogenous reaction zone with all areas of platinum operating under optimum conditions.

7.4 Conclusions.

The results for full fuel cell testing of sputter deposited catalysts show promising results for the polarisation and power curves, particularly when compared like for like with the polarisation and power curves seen for the high surface area platinum electrodes also reported. The analysis of these electrodes by the simple pore method suggests that these electrodes show optimum platinum utilisation when manufactured as thin as possible, but even at the narrow thicknesses seen for this technique, the values of ψ decrease rapidly at higher overpotentials.

Chapter 8: Conclusions.

The stated aim of the work in this thesis was to carry out research that would advance the commercialisation of fuel cells by reducing the capital cost of fuel cell units, in particular by reducing the amount of expensive platinum catalyst required. Two approaches were taken; sputter deposited platinum catalysts and tungsten carbide anode catalysts.

By considering a thorough survey of the literature of fuel cell catalysts, the efficient use of platinum emerged as a major motivation for this work. In chapter 2, the formation of catalyst layers by sputter deposition and reactive sputter deposition was explored. Sputtering and reactive sputtering produced catalyst layers with roughness factors up to 154 ± 5 and specific catalyst roughness of up to $\mathbf{a} = (1.1 \pm 5) \times 10^9\ m^2\ m^{-3}$. This value of catalyst layer specific roughness is several orders of magnitude higher than that seen for conventional fuel cell catalyst layers. By producing a catalyst layer with this high value of specific roughness, fuel cell electrodes can be produced that make extremely efficient use of the platinum, localising the majority of metal in the narrow region where fuel cell reactions take place. However, sputter deposition is shown to have a slight detrimental effect on polymer electrolyte membrane conductivity. An alternative route to depositing a catalyst layer directly on the surface of Nafion has been described, though it shows only limited promise due to the incomplete transfer and poor adhesion of the platinum layer and extensive cracking of the platinum, leaving some platinum isolated from electronic contact.

Tungsten carbide catalysts were investigated for fuel cell anode reactions. In chapter 4, several synthetic routes towards high surface area tungsten carbides have been

described, and the catalysts were characterised by BET surface area analysis and XRD analysis. The catalysts were tested in a half cell and showed promising activity for the oxidation of hydrogen. They were also investigated in a full fuel cell with a high surface area platinum cathode. In a fuel cell environment the catalysts showed very promising polarisation performance, particularly when compared to a platinum catalysed anode in the same fuel cell under identical conditions. The performance of a fuel cell with tungsten carbide anodes was tested with 100ppm CO in the hydrogen fuel. Significantly, the presence of CO in the fuel, which would poison a conventional fuel cell electrode, does not have a detrimental effect on the activity of the anode.

Although the catalytic activity of tungsten carbide is significantly lower than that of platinum, the cost saving associated with the use of tungsten carbide represent a major advantage. In addition the resistance to CO poisoning allows the use of less pure fuels and reformer output, simplifying the overall fuel cell infrastructure and potentially reducing fuel costs.

A fuel cell with sputter deposited catalysts was tested. Again, the performance showed promising performance when compared to a conventional high surface area platinum MEA.

A simple-pore model of the electrodes was implemented to demonstrate the extent of utilisation of the platinum catalyst. The results from this model further emphasised the need for ultrathin catalyst layers, and showed the remarkable extent to which catalyst utilisation falls with increasing overpotential even for the thin sputter deposited catalyst layers.

This thesis presents the results of two different approaches to the problem of high capital cost of fuel cells. By thoroughly exploring a technique to make extremely efficient use of the platinum catalyst, and by examining the potential for the replacement of platinum catalysts on the anode by tungsten carbide, progress towards the commercialisation of fuel cells through advances in catalysis has been made.

8.2: Further Work.

Many ongoing research areas arise from the conclusions in this work. In particular, the application of reactive sputter deposition to other types of fuel cell and fuel cell catalyst, such as bi- tri- and tetrametallic methanol oxidation catalysts for DMFCs. Better controls of the sputtering conditions could give a future experimenter the ability to tune and refine the physical properties of the catalyst layers. Similarly, an extremely broad range of base metallic carbides and nitrides could be explored for the oxidation of methanol in DMFCs. Given the platinum-like behaviour of such materials and their resistance to CO poisoning, which prevents the use of Pt alone for DMFC catalysis, it is suggested that there may be potential a non-noble metal in this area also. However, an immediate priority to continue the work is the isolation of the kinetic current for hydrogen oxidation in a rotating disk electrode experiment.

8.3: Dissemination.

The work contained in this thesis has been presented in poster form at the Electrochem 2002 conference (Preston, UK), SET for Europe 2003 (ESRF, Grenoble, France) and Electrochem 2005 (Newcastle, UK). Work from this thesis was also presented orally at Electrochem 2004 (Leicester, UK). A paper on the results of chapters 4 and 5 is being prepared.

Appendix A: Analytical Techniques.

A.1: BET surface area analysis.

The surface areas of the tungsten carbide catalysts synthesised in this work were assessed by BET surface analysis by the analytical service of the Department of Chemical Engineering, Imperial College London, on a Micrometrics ASAP 2010 BET analyser. The technique is based on the adsorption isotherm developed by Stephen Brunauer, Paul Emmet and Edward Teller.

$$V/V_{monolayer} = cz/(1-z)\{1-(1-c)z\}$$

where $c = \exp[\Delta H_{desorption}^{\varnothing} - \Delta H_{vaporisation}^{\varnothing}]/RT$ and $z = p/p^*$, the ratio of gas pressure to the vapour pressure of the adsorbate, $V_{monolayer}$ is the monolayer volume. The isotherm relates ratio of the volume of a gas to the volume of an adsorbed monolayer to the ratio of gas pressure to the vapour pressure of the adsorbate. The measurement is performed at the boiling temperature of liquid nitrogen at various pressures. The quantity $z/(1-z)V$ is plotted against z, where $z = p/p^*$, the ratio of gas pressure to the vapour pressure above the adsorbate. From this the volume of the monolayer and the constant c can be calculated. The BET isotherm measurement has limitations. The substrate must adsorb layers of the gas without absorbing the gas, and the isotherm underestimates adsorption at low pressures and overestimates at high pressures.

A2: Platinum Loading by ICP-AES.

The platinum loading of the samples was assessed by dissolving the catalysts in aqua regia. The platinum content of the aqua regia samples was measured by inductively coupled plasma atomic emission spectroscopy (ICP-AES) by Dr V. Din at the Natural History Museum's analytical laboratory, Exhibition Road, London SW7. To measure

the atomic emission spectrum, the samples were atomised (converted into gaseous atoms) by an inductively coupled plasma source. The sample is partially ionised by a spark, then heated by injecting into a radio-frequency induction coil, causing the ions to move within the circular magnetic field. The sample can reach temperatures of 6000 to 8000 K. The heating promotes electrons in outer orbitals of the sample atoms, which relax, emitting photons with energy characteristic of the element studies. Following calibration, the intensity of key parts of the emission spectrum can be used to assess the concentration of the element under study in the sample.

A3: X-Ray Powder Diffraction.

The tungsten carbide samples in chapter 5 were measured by X-ray powder diffraction. X-ray diffraction was originally used by Max von Laue to measure the spacing of atomic layers in single crystal structures using a range of X-ray wavelengths in an effort to isolate at least one instance of constructive interference. From this, the crystal plane spacing can be calculated using Bragg's Law. Debye and Scherrer later modified the method, using monochromatic radiation and an area of randomly-orientated small crystals in a powder. The reflection of the X-ray radiation from the sample takes the form of cones at an angle of 2θ from the incident beam. The resulting diffraction pattern can be compared to a library of existing patterns. The particulate size is assessed by measuring the broadening of a characteristic peak and calculating the size with the Debye-Scherrer equation, named for the technique's originators:

$$T = \frac{C\lambda}{B\cos\theta}$$

Where T is the crystallite diameter, λ is the X-ray wavelength and C is a correction factor depending on crystallite shape. B is the full width at half maximum of the peak.

The assessment of crystallite sizes of the tungsten carbide samples is detailed in chapter 6; Dr Yangdong Qian of the Department of Chemistry, Imperial College assisted with the interpretation of the peaks using peak-assign software.

9: References.

1. A.J. Appleby and F.R. Foulkes, *Fuel cell handbook.* 1st ed. 1989, New York: Van Nostrand Reinhold.

2. P.H. Rieger, *Electrochemistry*. 2nd ed. 1994, London: Chapman and Hall. 483.

3. S. Trasatti, *Work function, electronegativity, and electrochemical behaviour of metals : III. Electrolytic hydrogen evolution in acid solutions.* Journal of Electroanalytical Chemistry, 1972. **39**(1): p. 163-184.

4. A. Dicks and J. Larminie, *Fuel Cell Systems Explained*. 2nd ed. 2003, Chichester: Wiley.

5. L. Carrette, K.A. Friedrich, and U. Stimming, *Fuel Cells- Fundamentals and Applications.* Fuel Cells, 2001. **1**: p. 5-39.

6. W. Grot, *Use of Nafion Perfluorosulfonic Acid Products as Separators in Electrolytic Cells.* Chemie Ingienieur Technik, 1978. **50**(4): p. 299-301.

7. K.A. Mauritz and R.B. Moore, *State of Understanding of Nafion.* Chemical Reviews, 2004. **104**(4): p. 4535-4585.

8. C.H. Hamann, A. Hamnett, and W. Vielstich, *Electrochemistry*. 1998, Chichester: Wiley-VCH.

9. H.-G. Haubold, T. Vad, H. Jungbluth, and P. Hiller, Electrochimica Acta, 2001. **46**: p. 1599.

10. L. Rutabat, A.L. Rollet, G. Gebel, and O. Diat, Macromolecules, 2002. **35**: p. 4050.

11. M.S. Wilson, J.S. Valerio, and S. Gottesfeld, *Low platinum loading electrodes for polymer electrolyte fuel cells fabricated using thermoplastic ionomers.* Electrochimica Acta, 1995. **40**: p. 355-363.

12. S. Gottesfeld and T.A. Zawodzinski, *Polymer Electrolyte Fuel Cells*, in *Advances in Electrochemical Sciences and Engineering*, R.C. Alkire, et al., Editors. 1997, Wiley-VCH: Weinheim. p. 195-301.

13. D.J. Thompsett, *Catalysts for the proton exchange membrane fuel cell*, in *Fuel Cell Technology Handbook*, G. Hoogers, Editor. 2003, CRC Press: Boca Raton, FL.

14. J. Thomas, *Sputtering: Present and Future. Introduction.* Philosophical Transactions, 2004. **362**(1814): p. 3-4.

15. M.F. Weber, S. Mamche-Afra, M.J. Dignam, L. Patakt, and R.D. Venter, *Sputterer Fuel Cell Electrodes.* Journal of the Electrochemical Society, 1987. **134**(6): p. 1416-1418.

16. S. Mukerjee, S. Srinivasan, and A.J. Appleby, *Effect of sputtered film of platinum on low platinum loading electrodes on electrode. Kinetics of oxygen reduction in proton exchange membrane fuel cells.* Electrochimica Acta, 1993. **38**(12): p. 1661-9.

17. S. Hirano and F. Fujikawa, *High performance PEFCs with sputter-deposited Pt layer on low- Pt-loading electrode.* Denki Kagaku, 1996. **64**(6): p. 737-742.

18. S.Y. Cha and W.M. Lee., *Performance of Proton Exchange Membrane Fuel Cell Electrodes Prepared by Direct Deposition of Ultrathin Platinum on the Membrane Surface.* Journal of the Electrochemical Society, 1999. **146**(11): p. 4055-4060.

19. R. O'Hayre, S.-J. Lee, S.-W. Cha, and F.B. Prinz, *A sharp peak in the performance of sputtered platinum fuel cells at ultra-low platinum loading.* Journal of Power Sources, 2002. **109**(2): p. 483-493.

20. Y.-F. Su, T.-C. Chou, T.-R. Ling, and C.-C. Sun, *Photocurrent performance and nanostructure analysis of TiO_2/ITO electrodes prepared using reactive sputtering.* Journal of the Electrochemical Society, 2004. **151**(9): p. A1375-A1382.

21. M.-C. Jung, H.-D. Kim, M. Han, W. Jo, and D.C. Kim, *X-ray photoelectron spectroscopy study of Pt-oxide thin films deposited by reactive sputtering using O_2/Ar gas mixtures.* Japanese Journal of Applied Physics, Part 1: Regular Papers, Short Notes & Review Papers, 1999. **38**(8): p. 4872-4875.

22. Y. Abe, M. Kawamura, and K. Sasaki, *Preparation of PtO and a-PtO_2 thin films by reactive sputtering and their electrical properties.* Japanese Journal of Applied Physics, Part 1: Regular Papers, Short Notes & Review Papers, 1999. **38**(4A): p. 2092-2096.

23. L. Maya, L. Riester, T. Thundat, and C.S. Yust., *Characterization of sputtered amorphous platinum dioxide films.* Journal of Applied Physics, 1998. **84**(11): p. 6382-6386.

24. L. Maya, E.W. Hagaman, R.K. Williams, X.-D. Wang, G.D.D. Cul, and J.N. Fiedor, *Carbon in α-Platinum Dioxide.* Journal of Physical Chemistry B., 1998. **102**: p. 1951-1955.

25. J.R. McBride, G.W. Graham, C.R. Peters, and W.H. Weber, *Growth and Characterization of Reactively Sputtered Thin-Film Platinum Oxides.* Journal of Applied Physics, 1991. **69**(3): p. 1596-1604.

26. V. Voorhees and R. Adams, Journal of the American Chemical Society, 1922. **44**: p. 1397-1405.

27. L. Maya, G.M. Brown, and T. Thundat., *Porous platinum electrodes derived from the reduction of sputtered platinum dioxide films.* Journal of Applied Electrochemistry, 1999. **29**: p. 883-888.

28. E. Song, C. Shi, and F.C. Anson., *Comparison of the Behavior of Several Cobalt Porphyrins as Electrocatalysts for the Reduction of O_2 at Graphite Electrodes.* Langmuir, 1998. **14**: p. 4315-4321.

29. H. Wang, R. Côté, G. Faubert, D. Guay, and J.P. Dodelet, *Effect of the pre-treatment of carbon black supports on the activity of Fe-based electrocatalysts for the reduction of oxygen.* Journal of Physical Chemistry B, 1999. **103**(12): p. 2042-2049.

30. H. Bohm, *Adsorption und anodische oxydation von wasserstoff an wolframcarbid.* Electrochimica Acta, 1970. **12**: p. 1273-1280.

31. R.B. Levy and M. Boudart, *Platinum-like behaviour of Tungsten Carbide in Surface Catalysis.* Science, 1973. **181**: p. 547-548.

32. L. Leclercq, M. Provost, H. Pastor, and G. Leclercq, *Catalytic properties of transition metal carbides. II. Activity of bulk mixed carbides of molybdenum and tungsten in hydrocarbon conversion.* Journal of Catalysis, 1989. **117**(2): p. 384-95.

33. L. Leclercq, M. Prigent, F. Daubrege, L. Gengembre, and G. Leclercq, *Tungsten carbide and tungsten-molybdenum carbides as automobile exhaust catalysts.* Studies in Surface Science and Catalysis, 1987. **30**(Catal. Automot. Pollut. Control): p. 417-26.

34. K.E. Curry and L.T. Thompson, *Carbon-Hydrogen Bond Activation over Tungsten Carbide Catalysts.* Catalysis Today, 1994. **21**(1): p. 171-184.

35. V.S. Palanker, D.V. Sokolsky, E.A. Mazulevsky, and E.N. Baybatyrov, *Catalytic activity and capacitance of tungsten carbide as a function of its dispersity and surface state.* Electrochimica Acta, 1977. **22**(6): p. 661-7.

36. P.N. Ross, Jr. and P. Stonehart, *The relation of surface structure to the electrocatalytic activity of tungsten carbide.* Journal of Catalysis, 1977. **48**(1-3): p. 42-59.

37. I. Nikolov, V. Nikolova, T. Vitanov, and M. Svatá, *The effect of method of preparation on the catalytic activity of tungsten carbide.* Journal of Power Sources, 1979. **4**(1): p. 65-75.

38. C.J. Barnett, G.T. Burstein, A.R.J. Kucernak, and K.R. Williams, *Electrocatalytic activity of some carburised nickel, tungsten and molybdenum compounds.* Electrochimica Acta, 1997. **42**(15): p. 2381-2388.

39. J.M. Giraudon, P. Devassine, J.F. Lamonier, L. Delannoy, L. Leclercq, and G. Leclercq, *Synthesis of tungsten carbides by temperature-programmed*

reaction with CH_4-H_2 mixtures. Influence of the CH4 and hydrogen content in the carburizing mixture. Journal of Solid State Chemistry, 2000. **154**(2): p. 412-426.

40. D.R. McIntyre, G.T. Burstein, and A. Vossen, *Effect of carbon monoxide on the electrooxidation of hydrogen by tungsten carbide.* Journal of Power Sources, 2002. **107**(1): p. 67-73.

41. K. Reichelt and X. Jiang, *The preparation of thin films by physical vapour deposition methods.* Thin Solid Films, 1990. **191**: p. 91-126.

42. F. Klabunde, M. Lõhmann, J. Bläsing, and T.P. Drüsdea., *The influence of argon pressure on the structure of sputtered molybdenum: From porous amorphous to a new type of highly textured film.* Journal of Applied Physics, 1996. **80**(11): p. 6266-6273.

43. T.P. Drüsdea, M. Lõhmann, F. Klabunde, and T.-M. John, *Investigations on energy fluxes in magnetron sputter-deposition: implications for texturing and nanoporosity of metals.* Sputtering and Coatings Technology, 2000. **133-134**: p. 126-130.

44. H. Neff, S. Henkel, E. Hartmannsgruber, E. Steinbeiss, W. Michalke, K. Steenbeck, and H.G. Schmidt, *Structural, optical, and electronic properties of magnetron- sputtered platinum oxide films.* Journal of Applied Physics, 1996. **79**(10): p. 7672-7675.

45. W.D. Westwood and C.D. Bennewitz, *Formation of platinum oxide films by reactive sputtering.* Journal of Applied Physics, 1974. **45**(5): p. 2313-15.

46. Y. Abe, H. Yanagisawa, and K. Sasaki, *Preparation of Pt and Pt oxide thin films by reactive sputtering and their electrical properties.* Japanese Journal of Applied Physics, Part 1: Regular Papers, Short Notes & Review Papers, 1999. **38**(4): p. 2092-2096.

47. K. Yamamoto, D.M. Kolb, R. Kötz, and G. Lehmpfuhl, *Hydrogen adsorption and oxide formation on platinum single crystal electrodes.* Journal of Electroanalytical Chemistry, 1979. **96**(2): p. 233-239.

48. S. Gilman, *A study of the adsorption of carbon monoxide and oxygen on platinum. significance of the "polarization curve"*. Journal of Physical Chemistry, 1962. **66**(12): p. 2657-2664.

49. S. Gilman, *Electrochemical surface oxidation of platinum.* Electrochimica Acta, 1964. **9**(7): p. 1025-1046.

50. M.J. Weaver, S.C. Chang, L.W.H. Leung, and X. Jiang, *Evaluation of absolute saturation coverages of carbon monoxide on ordered low-index platinum and rhodium electrodes.* Journal of Electroanalytical Chemistry, 1992. **327**(2): p. 247-260.

51. J.M. Feliu, J.M. Orts, A. Femandez-Vega, A. Aldaz, and J. Clavilier, *Electrochemical studies in sulphuric acid solutions of adsorbed CO on Pt (111) electrodes.* Journal of Electroanalytical Chemistry, 1990. **296**(1): p. 191-201.

52. S. Hirano, J. Kim, and S. Srinivasan, *High performance proton exchange membrane fuel cells with sputter-deposited Pt layer electrodes.* Electrochimica Acta, 1997. **42**(10): p. 1587-1593.

53. DuPont, *Techincal Information: Safe Use and Handling of Perfluorosulfonic Acid Products*. February 2004: Fayetteville, NC.

54. S.R. Yoon, G.H. Hwang, W.I. Cho, L.-H. Oh, S.-A. Hong, and H.Y. Ha, *Modifications of polymer films for DMFCs using Pd films formed by sputtering.* Journal of Power Sources, 2002. **106**(1-2): p. 215-223.

55. R. Greef, R. Peat, L.M. Peter, D. Pletcher, and J. Robinson, *Instrumental Methods in Electrochemistry*. 1990, Chichester: Ellis Harwood Ltd.

56. J. Muller, G. Frank, K. Colborn, and D. Wilkinson, *Handbook of Fuel Cells: Fundamentals, Technology, Applications*, H. Gasteiger, Editor. 2003, John Wiley and Sons: New York. p. 848.

57. J.R. Selman and Y.P. Lin, *Application of ac impedance in fuel cell research and development.* Electrochimica Acta, 1993. **38**(14): p. 2063-73.

58. B. Andreaus and G.G. Scherer, *Proton-conducting polymer membranes in fuel cells - humidification aspects.* Solid State Ionics, 2004. **168**(3-4): p. 311-320.

59. DuPont, *Nafion PFSA Membranes*. 2004.

60. T.A. Zawodzinski, M. Neeman, L. Sillerud, and S. Gottesfeld, *Determination of Water Dlffusion Coefficients in Perfluorosulfonate Ionomeric Membranes.* Journal of Physical Chemistry, 1991. **95**(15): p. 6040-6040.

61. J. Halim, F.N. Büchi, O. Haas, M. Stamm, and G.G. Scherer, *Characterization of perfluorosulfonic acid membranes by conductivity measurements and small-angle x-ray scattering.* Electrochimica Acta, 1994. **39**(8-9): p. 1303-1307.

62. B.D. Cahan and J.S. Wainright, *AC impedance investigations of proton conduction in nafion.* Journal of the Electrochemical Society, 1993. **140**(12): p. L185-L186.

63. Y. Sone, P. Ekdunge, and D. Simonsson, *Proton conductivity of Nafion 117 as measured by a four-electrode ac impedance method.* Journal of the Electrochemical Society, 1996. **143**(4): p. 1254-9.

64. R.F. Silva, M. De Francesco, and A. Pozio, *Solution-cast Nafion ionomer membranes: preparation and characterization.* Electrochimica Acta, 2004. **49**(19): p. 3211-3219.

65. S.-A. Sheppard, S.A. Campbell, J.B. Smith, G.W. Lloyd, T.W. Ralph, and F.C. Walsh., *Electrochemical and microscopic characterisation of platinum-coated perfluorosulfonic acid (Nafion 117) materials.* Analyst, 1998. **123**: p. 1923-1929.

66. A. Lofberg, A. Frennet, G. Leclercq, L. Leclercq, and J.M. Giraudon, *Mechanism of WO_3 reduction and carburization in CH_4/H_2 mixtures leading to bulk tungsten carbide powder catalysts.* Journal of Catalysis, 2000. **189**(1): p. 170-183.

67. T.J. Schmidt, H.A. Gasteiger, and R.J. Behm, *Rotating Disk Electrode Measurements on the CO Tolerance of a High Surface Area Pt/Vulcan Carbon Fuel Cell Catalyst.* Journal of the Electrochemical Society, 1999. **146**(4): p. 1296-1304.

68. M.U. Pechini. 1967: USA Patent 3330697.

69. C.A. Kodaira, H.F. Brito, O.L. Malta, and O.A. Serra, *Luminescence and energy transfer of the europium (III) tungstate obtained via the Pechini method.* Journal of Luminescence, 2003. **101**(1-2): p. 11-21.

70. A.F. Fuentes, O. Hernandez-Ibarra, G. Mendoza-Suarez, J.I. Escalante-Garcia, K. Boulahya, and U. Amador, *Structural analysis of several W(VI) and Mo(VI) complex perovskites prepared by the polymeric precursors method.* Journal of Solid State Chemistry, 2003. **173**(2): p. 319-327.

71. M. Stojanovic, R.G. Haverkamp, C.A. Mims, H. Moudallal, and A.J. Jacobson, *Synthesis and characterization of* $LaCr_{1-x}Ni_xO_3$ *perovskite oxide catalysts.* Journal of Catalysis, 1997. **166**(2): p. 315-323.

72. C. Laberty-Robert, F. Ansart, C. Deloget, M. Gaudon, and A. Rousset, *Powder synthesis of nanocrystalline ZrO2–8%*Y_2O_3 *via a polymerization route.* Materials Research Bulletin, 2001. **36**(12): p. 2083-2101.

73. A. Wijayasinghe, B. Bergman, and C. Lagergren, $LiFeO_2$-$LiCoO_2$-NiO *cathodes for molten carbonate fuel cells.* Journal of the Electrochemical Society, 2003. **150**(5): p. A558-A564.

74. USC, *Private Communication from United Steel Companies to JCPDS*: Sheffield, UK.

75. G. McCarthy, *ICDD Grant-in-aid report*. 1973, Penn. State University.

76. O. Yamaguchi, D. Tomihisa, H. Kawabata, and K. Shimizu, *Formation and transformation of tungsten trioxide prepared from alkoxide.* Journal of the American Ceramic Society, 1987. **70**(5): p. C/94-C/96.

77. H.E. Swanson and E. Tatge, *Standard x-ray diffraction powder patterns.* National Bureau of Standards Circular (U. S.), 1953. **539**(Vol. I): p. 95 pp.

78. G. Leclercq, M. Kamal, J.M. Giraudon, P. Devassine, L. Feigenbaum, L. Leclercq, A. Frennet, J.M. Bastin, A. Lofberg, S. Decker, and M. Dufour, *Study of the preparation of bulk powder tungsten carbides by temperature programmed reaction with CH_4+H_2 mixtures.* Journal of Catalysis, 1996. **158**(1): p. 142-169.

79. R.M.Q. Mello and E.A. Ticianelli, *Kinetic Study of the Hydrogen Oxidation Reaction on Platinum and Nafion Covered Platinum Electrodes.* Electrochimica Acta, 1997. **42**(6): p. 1031.

80. L. Leclercq, M. Provost, H. Pastor, J. Grimblot, A.M. Hardy, L. Gengembre, and G. Leclercq, *Catalytic properties of transition metal carbides. I. Preparation and physical characterization of bulk mixed carbides of molybdenum and tungsten.* Journal of Catalysis, 1989. **117**(2): p. 371-83.

81. G.T. Burstein, D.R. McIntyre, and A. Vossen, *Relative activity of a base catalyst toward electro-oxidation of hydrogen and methanol.* Electrochemical and Solid State Letters, 2002. **5**(4): p. A80-A83.

82. P.N. Ross, Jr., J. MacDonald, and P. Stonehart, *Surface composition of catalytically active tungsten carbide.* Journal of Electroanalytical Chemistry and Interfacial Electrochemistry, 1975. **63**(3): p. 450-5.

83. H. Binder, A. Koehling, W. Kuhn, W. Lindner, and G. Sandstede, *Tungsten carbide electrodes for fuel cells with acid electrolyte.* Nature (London, United Kingdom), 1969. **224**(5226): p. 1299-300.

84. S. Bodoardo, M. Maja, N. Penazzi, and F.E.G. Henn, *Oxidation of hydrogen on WC at low temperature.* Electrochimica Acta, 1997. **42**(17): p. 2603-2609.

85. K. Ota, Y. Inoue, N. Motonira, and N. Kamiya, Journal of New Material for Electrochemical Systems, 2000. **3**(3): p. 193-197.

86. CRC, *CRC Handbook of Chemistry and Physics*. 75th ed, ed. D.R. Lide. 1995, Boca Raton, Fl.: CRC Press.

87. E.A. Ticianelli, C.R. Derouin, and S. Srinivasau, *Localization of plating in low catalyst loading electrodes to attain high power densities in SPE fuel cells.* Journal of Electroanalytical Chemistry, 1988. **251**: p. 275-295.

88. A.T. Haug, R.E. White, J.W. Weidner, W. Huang, S. Shi, T. Stoner, and N. Rana, *Increasing proton exchange membrane fuel cell catalyst effectiveness through sputter deposition.* Journal of the Electrochemical Society, 2002. **149**(3): p. A280-A287.

89. M. Eikerling and A.A. Kornyshev, *Modelling the Performance of the Cathode Catalyst Layer of Polymer Electrolyte Fuel Cells.* Journal of Electroanalytical Chemistry, 1997. **453**(1): p. 89-106.

90. F. Gloaguen, P. Convert, S. Gamburzev, O.A. Velev, and S. Srinivasan, *An Evaluation of the Macro-homogenous and Agglomerate Model for Oxygen Reduction in PEMFCs.* Electrochimica Acta, 1998. **43**(24): p. 3767-3772.

91. K.L. Saenger, C.C. Jr., C. Lavoie, and S.M. Rossnagel., *Thermal stability and oxygen-loss characteristics of PtO films prepared by reactive sputtering.* Journal of Applied Physics, 1999. **86**(11): p. 6084-6087.

92. B.V. Tilak, R.S. Yeo, and S. Srinivasan, *Electrochemical Energy Conversion-Principles*, in *Comprehensive Treatise on Electrochemistry*, J.O.M. Bockris, Editor. 1981, Plenum: New York. p. 39-122.

93. S. Srinivasan, H.D. Hurwitz, and J.O.M. Bockris, *Fundamental Equations of Electrochemical Kinetics at Porous Gas-Diffusion Electrodes.* Journal of Chemical Physics, 1967. **46**(8): p. 3108-3122.

94. J. Jiang and A.R. Kucernak, *Investigations of fuel cell reactions at the composite microelectrode/solid polymer electrolyte interface. I. Hydrogen oxidation at the nanostructured Pt/Nafion membrane interface.* Journal of Electroanalytical Chemistry, 2004. **567**: p. 123-137.

95. S. Chen and A.R. Kucernak, *Electrocatalysis under conditions of high mass-transport: Investigation of hydrogen oxidation on single submicron Pt particles supported on carbon.* Journal of Physical Chemistry B, 2004. **108**(37): p. 13984-13994.